1-1-2012

Shear Deformation in Polymer Gels and Dense Colloidal Suspensions

Anindita Basu
University of Pennsylvania, abasu000@gmail.com

Recommended Citation

Basu, Anindita, "Shear Deformation in Polymer Gels and Dense Colloidal Suspensions" (2012). *Publicly Accessible Penn Dissertations*. 611.
http://repository.upenn.edu/edissertations/611

Shear Deformation in Polymer Gels and Dense Colloidal Suspensions

Abstract

This thesis investigates two soft-matter systems, viz., bio-polymer gels and colloidal dispersions under mechanical deformation, to study non-affinity and jamming. Most materials are assumed to deform affinely, i.e., macroscopic applied deformations are assumed to translate uniformly to the microscopic level. This thesis explores the validity of the affine assumption in model polymer networks under shear. Displacements of micron-sized fluorescent polystyrene tracer beads embedded in polyacrylamide (PA) gels are quantified when the sample is sheared. The experiments confirm that the macroscopic elasticity of PA gels behaves in accordance with traditional flexible polymer network elasticity theory. Microscopically, non-affine deformation is detected, and the observations are in qualitative agreement with many aspects of current theories of polymer network non-affinity. The measured non-affinity in PA gels suggests the presence of structural inhomogeneities resulting from the reaction kinetics, which likely predominates over the effects of thermal fluctuations.

Compared to flexible polymer gels, filamentous biopolymer networks generally have higher shear moduli, exhibit a striking increase in elastic modulus with increasing strain, and show pronounced negative normal stress when deformed under shear. Affine deformation is an essential assumption in the theories of these materials. The validity of this assumption is experimentally tested in fibrin and collagen gels. Measurements demonstrate that non-affine deformation is small for networks of thinner, relatively flexible filaments and decreases even further as strain increases into the non-linear regime. Many observations are consistent with the entropic nonlinear elasticity model for semiflexible polymer networks. However, when filament stiffness and mesh-size increase, then deformations become more non-affine and the observations appear to be consistent with enthalpic bending and stretching models.

A qualitatively different set of studies explores the rheology of monodisperse and bidisperse colloidal suspensions near the jamming transition as a function of packing fraction, steady-state strain rate, and oscillatory shear frequency. The experiments employ soft, temperature-sensitive polymer micro-spheres for easy tuning of sample packing fraction and a rheometer in order to explore scaling behaviors of shear stress versus strain rate, and storage/loss shear moduli versus frequency. Under steady shear, rheometer measurements exhibit predicted scaling behavior for volume fractions above and below the jamming transition that agree with scaling observed in monodisperse particle suspensions by microfluidic rheology; importantly, similar scaling behavior is observed for the first time in bidisperse particle suspensions. At finite frequency, new measurements were performed across the jamming transition for both monodisperse and bidisperse suspensions. The storage and loss moduli of the jammed systems, measured as a function of frequency and volume fraction, could be scaled onto two distinct master curves in agreement with simulation predictions [142]. For unjammed systems, stress-relaxation timescale is found to scale with volume fraction.

Degree Type

Dissertation

Degree Name

Doctor of Philosophy (PhD)

Graduate Group
Physics & Astronomy

First Advisor
Arjun G. Yodh

Second Advisor
Paul A. Janmey

Keywords
colloid, jamming, non-affine, polymer, rheology, shear

Subject Categories
Condensed Matter Physics | Physics

SHEAR DEFORMATION IN POLYMER GELS AND DENSE COLLOIDAL SUSPENSIONS

Anindita Basu

A DISSERTATION

in

Physics and Astronomy

Presented to the Faculties of the University of Pennsylvania

in

Partial Fulfillment of the Requirements for the

Degree of Doctor of Philosophy

2012

Arjun G. Yodh, James M. Skinner Professor of Science, Professor of Physics

Supervisor of Dissertation

Alan T. Charlie Johnson, Jr., Professor of Physics

Graduate Group Chairperson

Dissertation Committee

Paul A. Janmey, Professor of Physiology
Tom Lubensky, Professor of Physics
Douglas Durian, Professor of Physics
Gary Bernstein, Professor of Physics

Dedication

To my mother.

Acknowledgements

I am deeply indebted to the following individuals for my education and the work presented in this thesis.

I am infinitely grateful to my advisor, Dr. Arjun Yodh for his unfailing guidance and support, not to mention his patience in my endeavours. I acknowledge his constant efforts in teaching me to think critically and interact effectively. I also thank my thesis committee members- Drs. Gary Bernstein, Douglas Durian, Paul Janmey, and Tom Lubensky.

I thank my dear husband and best friend, Soumyadip Ghosh, for his unwavering support- he took upon himself a 130-mile commute, shine or snow during my PhD. I thank my mother and father, who provided me with every opportunity.

I am also grateful to my colleagues and group mates, past and present- Ahmed Alsayed, Kevin Aptowicz, David Busch, Dan Chen, Ke Chen, Piotr Habdas, Yilong Han, Larry Hough, Matt Gratale, Matt Lohr, Xiaoming Mao, Saurav Pathak, Matt Pelc, Tim Still, Qi Wen, Ye Xu, Peter Yunker, and Zexin Zhang. Not only were they instrumental in much that I have learned during my PhD, but they made every moment enjoyable.

I thank my collaborators for their deep insight and patience- Paulo Arratia, Douglas Durian, Jerry Gollub, Paul Janmey, Xiaoming Mao, Kerstin Nordstrom, Qi Wen. It was enlightening as well a pleasure working with them.

I also thank my mentors, Dr. Reeta Vyas, Dr. Supratik Guha and Dr. William Oliver, for their encouragement and guidance.

ABSTRACT

SHEAR DEFORMATION IN POLYMER GELS AND DENSE COLLOIDAL SUSPENSIONS

Anindita Basu

Arjun G. Yodh

This thesis investigates two soft-matter systems, *viz.*, bio-polymer gels and colloidal dispersions under mechanical deformation, to study *non-affinity* and *jamming*. Most materials are assumed to deform affinely, i.e., macroscopic applied deformations are assumed to translate uniformly to the microscopic level. This thesis explores the validity of the affine assumption in model polymer networks under shear. Displacements of micron-sized fluorescent polystyrene tracer beads embedded in polyacrylamide (PA) gels are quantified when the sample is sheared. The experiments confirm that the macroscopic elasticity of PA gels behaves in accordance with traditional flexible polymer network elasticity theory. Microscopically, non-affine deformation is detected, and the observations are in qualitative agreement with many aspects of current theories of polymer network non-affinity. The measured non-affinity in PA gels suggests the presence of structural inhomogeneities resulting from the reaction kinetics, which likely predominates over the effects of thermal fluctuations.

Compared to flexible polymer gels, filamentous biopolymer networks generally have higher shear moduli, exhibit a striking increase in elastic modulus with increasing strain, and show pronounced negative normal stress when deformed under shear. Affine deformation is an essential assumption in the theories of these materials. The validity of this assumption is experimentally tested in fibrin and collagen gels. Measurements demonstrate that non-affine deformation is small for networks of thinner, relatively flexible filaments and decreases even further as strain increases into the non-linear regime. Many observations are consistent with the entropic non-linear elasticity model for semiflexible polymer networks. However, when filament stiffness and mesh-size increase, then deformations become more non-affine and the observations appear to be consistent with enthalpic bending and stretching models.

A qualitatively different set of studies explores the rheology of monodisperse and bidisperse colloidal suspensions near the jamming transition as a function of packing fraction, steady-state strain rate, and oscillatory shear frequency. The experiments employ soft, temperature-sensitive polymer micro-spheres for easy tuning of sample packing fraction and a rheometer in order to explore scaling behaviors of shear stress versus strain rate, and storage/loss shear moduli versus frequency. Under steady shear, rheometer measurements exhibit predicted scaling behavior for volume fractions above and below the jamming transition [113, 141] that agree with scaling observed in monodisperse particle suspensions by *microfluidic* rheology [107]; importantly, similar scaling behavior is observed for the first time in *bidisperse* particle suspensions. At finite frequency, new measurements were performed across the jamming transition for both monodisperse and bidisperse suspensions. The storage and loss moduli of the jammed systems, measured as a function of frequency and volume fraction, could be scaled onto two distinct master curves in agreement with simulation predictions [142]. For unjammed systems, stress-relaxation timescale is found to scale with volume fraction.

Contents

List of Tables

List of Figures

Chapter 1

Introduction

Gels are an important subclass of soft matter composed of three dimensional polymer networks swollen in solvents. Jelly is a gel of polysaccharides [144]; contact lenses are hydrogels of silicone [106]; and cells in the human body are connected by collagen gels [91]. These gels have mechanical properties common to both fluids and solids, i.e., they are viscoelastic. The gel solvents make them macroscopically incompressible and enable gels to "flow" like fluids; the polymer network structures provide mechanical support for the gels. Not surprisingly, microscopic properties of polymers and the structure of polymer networks affect the elastic properties of gels. Increased polymer concentration and crosslinker concentration, for example, can lead to enhancements in gel elasticity. The solubility of polymers in the solvents can also be tuned to regulate gel elasticity by changing pH [24] or temperature [158]. As a result of this tunable elasticity, gels are widely applied in the food industry, environment control, medical instrumentation, and medicine. Polymer gels are one of the unifying theme of this thesis work; in the first part, we will study microscopic behavior of different polymer gels under macroscopic deformation in the first part of this thesis, using the second unifying concept of this work, *viz.*, shear rheology. In the second part, we will use hydrogel microparticles and shear rheology to explore mechanical behavior of soft glasses across the jamming transition. Easy tunability of hydrogel properties as a function of temperature to induce jamming.

1.1 Non-affine Deformation in Flexible Polymer Gels

The elastic behavior of many synthetic polymer gels such as polyethylene glycol (PEG) and polyacrylamide (PA) is similar to that of rubber-like materials. Their elasticity can be understood on the basis of the classic theory of rubber elasticity [2]. Affine deformation is an essential assumption in the classical theory of elasticity. In this case, deformation is assumed to be distributed homogeneously in the material so that strain is spatially constant at all length scales.

Affine deformation implies a mechanical response with uniformly distributed strain, γ, i.e., the *local microscopic* strain is identical to the *global macroscopic* strain applied to the material. This idea is depicted by the schematic in Fig. 1.1, which shows a cross-section of polymer gel under shear. The grey circles along the vertical dashed line indicate the position of tracer beads entrapped in a gel with no external loading. When a shear force is applied on the top surface of the gel, the circles move as the gel deforms. If the gel were to deform affinely, then the tracer beads would displace to new positions given by green circles all of which lie along the oblique dashed line. However, if the gel deforms non-affinely, as real gels are wont to do, then the tracer bead displacement would deviate from the affine position to a random new position denoted by the red circles.

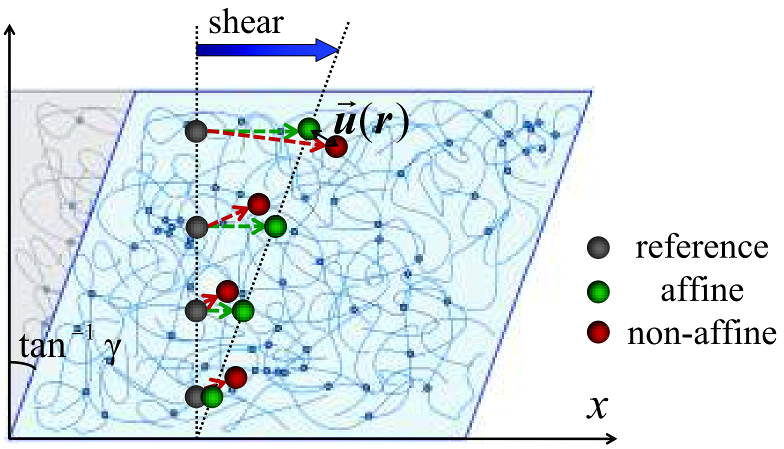

Figure 1.1: Illustration of affine and non-affine shear deformation of polymer gels with entrapped tracer beads.

The affine assumption permits elastic properties of cross-linked polymer networks to be readily derived from theories of rubber elasticity based on the entropy of a single polymer chain in the network. In practice, however, such affine deformations only occur in perfect crystals under very small deformation. In polymer networks, especially networks composed of semi-flexible or rigid filaments, the microscopic network deformations should be non-affine below certain length scale.

Non-affinity can arise from different sources. In near-ideal flexible polymer melts, deformations might be expected to be affine on length scales much larger than the average mesh size and non-affine at lengths scales of the order of the mesh size or smaller [125]. Random thermal fluctuations of the cross-link junctions, along with thermal undulations of the polymer chains may also lead to non-affine behavior in polymer gels. Inhomogeneities introduced into the network micro-structure during sample preparation can also introduce non-affine responses; such inhomogeneities might be expected to be a function of reaction kinetics and other sample preparation parameters [23].

Over the years, the connection between shear deformation and non-affinity has been explored theoretically in a wide range of materials including rubber-like spatially homogeneous elastic media [23], entangled or cross-linked polymer networks [126, 38, 29, 139, 136], semi-flexible polymer networks with rigid [45] and flexible cross-links [47], stiff rod networks [157], biopolymers [93], amorphous systems [140] and foams [78]. Indeed, it has been proposed that non-linear elasticity in polymer networks has its origin in non-affine responses [125]. In spite of continued interest in this problem and its fundamental importance, relatively little experimental quantification of the non-affine phenomenon has been carried out in semi-flexible biopolymer gels [155, 90], and we are not aware of any non-affinity studies for the simple case of flexible polymers. Experiments along these lines provide benchmarks for future understanding of the subject.

Chapter 4 describes an investigation of non-affine shear deformations in a model flexible polymer gel: polyacrylamide gels with bisacrylamide cross-links. Polyacrylamide is well suited for the investigation because it is comparatively well-controlled, and its stiffness is tunable by the number of bisacrylamide cross-links. As part of this study, macroscopic rheological measurements are carried out to confirm the simple rubber-like elastic character of these networks. Then deformation fields in the gels under external shear stress are characterized by measuring the displacements of fluorescent beads entrapped in the gels. Bulk rheology and confocal microscopy are used in concert for the latter study. To this end, a home built apparatus that will be described in **Chapter 2** is constructed; the apparatus permits simultaneous shearing and visualization of the entrapped tracer beads in polyacrylamide gels. A non-affine parameter, $\mathcal{A}$, is defined to quantify the degree of non-affinity in the displacement field. $\mathcal{A}$ is measured as a function of bead size, polymer chain density, and cross-link density in the gels. Such measurements enable us to test simple predictions of a recently developed theory of non-affinity in random elastic media [23], and thereby obtain estimates for the fluctuations in elastic modulus of the gels from $\mathcal{A}$. The findings from this study have been published [8].

1.2 Non-affine Deformation in Bio-polymer Gels

Semi-flexible bio-polymer networks are ubiquitous in nature and are of physiological importance. Gels composed of collagen are the major constituents of extra-cellular matrices (ECM); actin is main ingredient of all cyto-skeletal structures, and fibrin is a critical component in blood clots. Beside being an indispensible part of all biological systems, these gels display unique macroscopic elastic behavior which are not observed in rubber-like materials, *viz.*, higher shear modulus at low polymer concentrations compared to synthetic gels [68], non-linear elasticity [60, 33, 138, 34] at low strains, and significant negative normal force under shear [62, 66, 20]. These unique mechanical properties may have biological significance, and a mechanistic understanding of them is beyond the scope of classic rubber elasticity theory [93, 138].

Several theoretical and simulation studies model these unique elastic behaviors in bio-polymer gels [47, 50, 93, 125, 115, 13]. Broadly speaking, two types of theoretical models account for the elasticity of biological polymer gels. Both approaches are successful in predicting strain-stiffening and negative normal stress, both characteristic mechanical properties of biological gels. The first model is an affine model. As in the case of the classical theory for rubber elasticity, it treats the biological filaments as entropic springs and assumes affine deformation, i.e., it assumes that strain is uniformly distributed in the polymer networks. According to this model, strain-stiffening of polymer networks originates from the nonlinear force extension curve of individual biopolymers [138, 93]. In spite of the success of the affine deformation model in accounting for both non-linear elasticity and negative normal stress in semi-flexible polymer gels, this picture is overly simplistic. In affine models, for example, each polymer deforms independently without affecting their neighbors, and any interactions between polymers are ignored. Such a deformation can only occur under ideal conditions [23]. In reality, all material deformations are expected to be non-affine on some length-scale. Indeed, non-affine deformation has been observed in many materials, including foams, synthetic polymer gels, and biological materials [23, 45, 155, 8, 116, 56, 13].

The other theoretical approach is the so-called non-affine model in which enthalpic deformation of stiff filaments is the dominant contribution to elasticity. It predicts non-affine deformation due to bending and reorganization of the polymer filaments. Filament bending causes "floppy modes" (low-frequency vibrational modes arising from low-energy excitations) in the network [50], which give rise to the non-affine network deformation [50, 57]. Rather than the nonlinear stretching of individual filaments, geometric effects such as the transition from filament bending/buckling dominated non-affine network deformation to a stretching dominated affine deformation may also give rise to the strain-stiffening [115, 85, 12]. Strain-stiffening in the non-affine model originates from network reorganization that leads to a transition from filament bending to filament stretching [115, 85].

Experimental verification of these two models is currently lacking. Depending on whether the bio-polymer gel elasticity model is entropic or not, different non-affinity predictions can be made as functions of polymer stiffness, crosslink density, etc., and such effects can be tested experimentally by measuring microscopic non-affine deformation in bio-polymer gels under different synthesis and probing conditions. Experimentally, it is advantageous to derive raw non-affinity measures in different gels that enable comparison between different polymer gel classes. Non-affinity measures can also help us to understand the underlying polymer network deformation mechanisms.

One possible way to check the validity of these two types of theoretical models is to measure the non-affine deformation in semi-flexible bio-polymer gels with a wide range of persistence lengths and mesh-sizes. This can be accomplished by embedding micron-sized fluorescent tracer particles in the gels and tracking the motion of these tracer particles under shear. **Chapter 5** compares non-affinity values in a wide variety of polymer gels, composed of polymers ranging from flexible to stiff. A fluorescent microscope with a piezo-driven objective is coupled with a rheometer for the non-affinity measurements. Non-affinity measurements made in salmon fibrin gels in particular, using this experimental setup, have been reported in [155].

Chapter 6 concentrates on two types of gels studied in the previous chapter, *viz.*, fibrin and collagen gels. These gels are synthesized under different conditions that allow us to study a wide range of gel morphologies. A set of non-affinity measurements are performed using a home-built setup described in **Chapter 2** that permits measurements with higher spatial resolution. In particular, non-affinity is studied in fibrin and collagen gels as functions of polymer concentration, filament diameter and applied shear strain. Rheology experiments are also performed to characterize macroscopic shear deformation in these gels. The non-affinity measures help to connect the microscopic picture to the macroscopic response. The effect of probe size is also investigated by using fluorescent polystyrene beads of different diameters as tracer particles.

1.3 Shear Rheology and Jamming

Jamming theory [89] offers a unified approach for understanding the onset of dynamic arrest under a variety of conditions across a wide range of material types including polymeric glasses [80], colloidal suspensions [163, 17], granular systems [72], emulsions [64] and foams [71]. The onset of mechanical rigidity in disordered systems, for example, can be induced by tighter packing, by decreasing temperature, or by reducing applied shear, as shown in Fig. 1.2. Recently, a growing number of works have explored the behavior of driven disordered systems along the shear axis of the jamming phase diagram. Many of these theoretical and simulation studies [113, 42, 141, 142] find that the mechanical properties of disordered systems exhibit scaling in the vicinity of the jamming transition, reminiscent of critical point scaling. Only a few experiments, however, have critically examined these predictions under shear [107, 132].

In **Chapter 7**, we employ macrorheology to study the shear response of soft-particle colloidal glasses in the vicinity of the jamming transition. In particular, the jamming phenomenon is investigated as functions of shear stress and packing fraction at a fixed non-zero temperature, as indicated by the plane in Fig. 1.2. Our experiments significantly extend previous work exploring scaling [113, 114, 42, 43, 141, 107, 142]. First, by using conventional rheometry, we readily carry out *frequency-dependent* shear experiments that test scaling predictions of *frequency-dependent* storage and loss moduli as a function of oscillatory frequency near the onset of jamming [110, 142]. Second, our work examines scaling predictions in both monodisperse and *bidisperse* colloidal suspensions. A model-independent scaling procedure that exploits

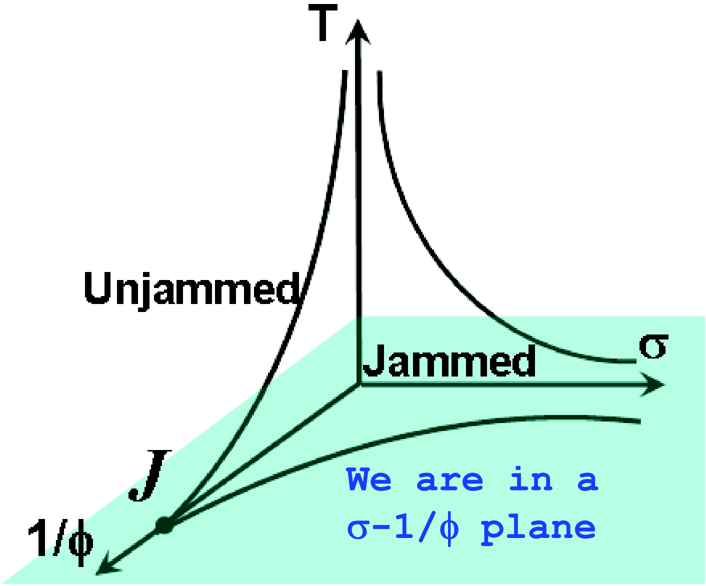

Figure 1.2: A jamming phase diagram for short-range, repulsive particles.

data from both above *and* below the jamming transition is employed for analysis, instead of the commonly used Herschel-Bulkley model [107, 114]. Furthermore, macroscopic rheometry permits comparison of zero-frequency stress versus strain-rate scaling with the findings based on microfluidics [107] in similar (monodisperse only) sample-types. Finally, in the process of carrying out these macroscopic measurements we clarify the strengths and weaknesses of the bulk rheometry approach for testing scaling phenomena in this system-class.

The experiments employ aqueous suspensions of poly(N-isopropyl acrylamide) (NIPA) microgel particles [130, 131, 120, 1]. NIPA particles are soft, micron-size colloidal spheres with repulsive interparticle potentials [40]. Their particle diameter is sensitive to temperature, which in turn permits experimenters to continuously tune colloidal packing fraction. By using soft particles we are able to investigate packing fractions both above and below the jamming transition. Recent experiments on a similar system which I coauthored, were performed using microfluidics and video microscopy [107]. In the present work, we employ a commercially available "macroscopic" rheometer that permits rapid, reproducible experimentation at macroscopic length scales. One limitation of the bulk rheometer for this class of scaling study is that its macroscopic dimensions can lead to relatively high Reynolds numbers and flow instabilities. Thus, special care is taken in our experiments to limit flow to low Reynolds numbers (i.e., $Re \lesssim 0.5$) [9]. Experiments are performed using two kinds of colloidal samples: monodisperse and bidisperse NIPA microgel particle suspensions. The bidisperse sample offers an experimental test of the scaling properties in a qualitatively different disordered medium wherein shear-induced crystallization and shear-banding effects are minimized (i.e., a system qualitatively different from the monodisperse suspension).

Zero-frequency shear-stress versus strain-rate measurements corroborate proposed scaling behavior [141, 42, 43] across the two sample types, including scaling exponent predictions. These data also demonstrate reasonable agreement with results of microfluidic rheology experiments [107, 69]. Rheology at finite frequency, i.e., the frequency-dependent shear moduli, is also found to be consistent with theoretical scaling predictions [110, 142]. The observed scaling of shear moduli with frequency and packing fraction in jammed systems is indicative of the presence of a diverging time-scale associated with the jamming transition [159]. On the unjammed side of the transition, the cross-over frequency, i.e., the frequency at which sample storage and loss moduli cross, is shown to scale with system packing fraction. Taken together, this set of experimental results adds to the emerging picture of jamming along the shear axis.

1.4 Organization

This thesis is organized as follows. **Chapters 2** and **3** briefly discuss the theory and instrumentation issues related to the non-affinity experiments on polymer gels. This is followed by **Chapter 4** that investigates non-affinity measurements in flexible PA gels. **Chapter 5** compares gel elasticity and non-affinity in different types of polymer gels, ranging from flexible PA gels, to gels of rigid carbon nanotubes. **Chapter 6** concentrates on fibrin and collagen gels, in particular, to probe such effects as polymer chain concentration, filament diameter, applied strain and tracer bead size on shear elasticity and non-affinity.

We switch gears in the following chapter. **Chapter 7** uses macroscopic shear rheology to probe flow behavior in soft repulsive microgel suspensions in the vicinity of the jamming transition. Critical scaling behavior in both steady-state and frequency-dependent regimes are studied. The following **Chapter 8** summarizes the experimental findings presented in this thesis and provides a brief outlook for possible follow-up experiments.

Chapter 2

Gel Elasticity Theory, Rheology and Non-affinity

2.1 Macro-rheology and Elasticity in Polymer Gels

Shear elasticity of polymeric gels can be characterized by rheological measurements using commercially available rheometers. Before the polymerization reaction is initiated, the ingredients are in the form of a viscous fluid, present either in a molten state or in solution. As a gel polymerizes, (in the zero-frequency limit) both elastic (storage) modulus, G' and viscous (loss) modulus, G'' increase with time, with G' increasing faster than G''. The point at which G' and G'' cross over and the mechanical response changes from liquid-like to solid-like is called the *sol-gel transition* [79], as shown in Fig. 2.1(a). This transition may be brought forth either by chemical reactions (e.g., formation of long polymer chains which get entangled, or cross-linking of polymeric chain that lead to the formation of networks), or physical processes (e.g., hydrogen bonding, van der Waals or electrostatic attractions) [164].

During a typical oscillatory measurement using a strain-controlled rheometer, the rheometer imposes an sinusoidal oscillatory shear strain on the sample of the form $\gamma = \gamma_0 sin(\omega t)$, and the shear stress, σ, required to generate such a deformation is measured. For a linear viscoelastic material, the resulting stress is also a sinusoidal function with a phase shift, ϕ, i.e., $\sigma = \sigma_0 sin(\omega t + \phi)$. The shear elastic modulus, G', is calculated from the part of stress that is in phase with strain, i.e., $G' = \frac{\sigma_0}{\gamma_0} cos\phi$. The out-of-phase stress is used to calculate the viscous response, i.e., the shear loss modulus, G'': $G'' = \frac{\sigma_0}{\gamma_0} sin\phi$. For crosslinked polymer networks, G' is often much larger than G'', i.e., the elastic response of the gel dominates.

Before the polymerization reaction is initiated, the ingredients are in the form of a viscous fluid, present either in a molten state or in solution, where $G'' > G'$. As a gel polymerizes, both elastic (storage) modulus, G' and viscous (loss) modulus, G'' increase with time, with G' increasing faster than G''. The point at which G' and G'' cross over marks the *sol-gel transition* [79]. Beyond this point, $G'' < G'$, i.e., the elastic component dominates. At the completion of the polymerization reaction, both G' and G'' plateau to steady-state values. Fig. 2.1(a) shows how G' and G'' evolves with time during a polymerization reaction. Data is shown for a polyacrylamide (PA) gel with 15% acrylamide (polymer) and 0.005% bisacrylamide (crosslink). Note that the formation of polyacrylamide chains and bisacrylamide crosslinks are occurring simultaneously as polymerization progresses in the aforementioned reaction.

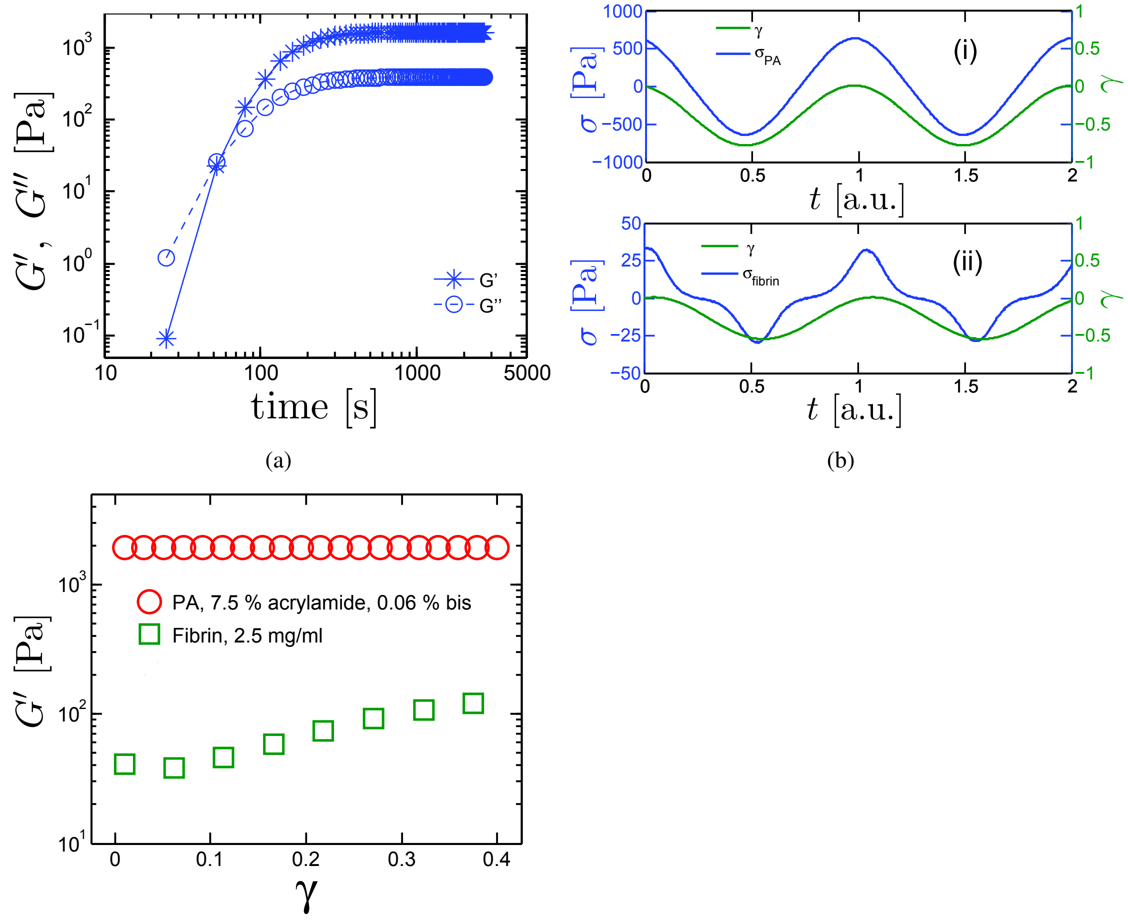

(a)

(b)

(c)

Figure 2.1: (a) Polymerization reaction of a sample PA gel. Mechanical properties of flexible (PA) and semi-flexible (fibrin) polymer gels. (b) Stress vs. strain of (i) PA and (ii) fibrin gels. (c) Elastic modulus vs. strain of PA gels, fibrin gels.

2.1.1 Linear Elasticity

Most synthetic polymer networks, such as polyacrylamide, polyethylene glycol, and polyvinyl alcohol are composed of flexible polymer chains, similar to the polymers in rubber. The elasticity of such synthetic polymer gels also share some characteristics of rubber elasticity. For example, its mechanical response is mostly linear, i.e., a sinusoidal shear stress is required to generate a sinosoidal strain, as shown for a sample polyacrylamide (PA) gel with bisacrylamide as crosslinker in Fig. 2.1(b)-(i). The fact that the phase shift, ϕ between the strain and stress response is small indicates that most of the stress response is in-phase or elastic, and the out-of-phase or viscous response is minimal, i.e., $G'' \approx 0$. In this case, the G' of the synthetic polymer gel is constant over a large range of strain. In Fig. 2.1(c), G' of a sample PA gel is measured as a function of shear strain. G' remains constant with increasing shear strain (data shown for $\gamma = 0.01$ – 0.4); indeed, in this experiment, G' remains constant as strain increased from $\gamma = 0.01$ up to 1.2; the test failed beyond this point due to detachment of gel from the rheometer plates [8]. At larger strains, beyond this linear elastic regime and beyond our experimental limit, nonlinear elasticity is expected in synthetic polymer gels similar to that observed in rubber-like materials at large deformations.

G' of synthetic polymer gels is also predicted to depend on crosslinker concentration, c, and temperature, T, i.e., $G' = ck_BT$ [145]. k_B is the Boltzmann constant. Measured dependences along these lines in PA gels are shown in the next chapter (Figures 4.3(b),(c)). The frequency response of crosslinked flexible and semi-flexible polymer gels are similar in that G' remains constant with frequency, ω, while G'' increases as ω increases. Such data for a sample PA gel is shown in the next chapter in Fig. 4.3(d).

2.1.2 Non-linear Elasticity

The G' for biopolymer hydrogels differs significantly from that of flexible PA gels. As illustrated in Fig. 2.1(b)-(ii), the stress required to generate a relatively large amplitude sinusoidal strain in fibrin gel is no longer a sine function. Higher-order harmonics are seen in the stress response signal, indicating the nonlinear relationship between shear stress and shear strain. Instead of being a constant, the G' of biological polymer gels often increases with increasing strain

(Fig. 2.1(c)). For example, the elastic modulus of a fibrin gel can increase about 20 times from 45 Pa to 800 Pa, when the strain increases from $\gamma = 0.01 – 0.8$ [155]. Such an increase in elastic modulus with increasing strain is referred to as strain-stiffening. Strain-stiffening is a ubiquitous behavior in crosslinked gels of semi-flexible biological polymers. Besides fibrin, gels made of F-actin, vimentin and collagen also exhibit strong strain-stiffening [138]. The strain-stiffening of biopolymer gels has biological significance; for example, it protects tissues from the detrimental effects of extremely large deformations [133]. This nonlinear elasticity in biopolymer networks can be characterized using Large Amplitude Oscillatory Shear (LAOS) techniques.

2.1.2.1 Fourier Transform Method

Shear stress data obtained from an imposed oscillatory shear strain may be decomposed into elastic and viscous components. Each component can be further decomposed into harmonic representations using either (a) Fourier transforms [156], or (b) Chebyshev polynomials of the first kind [30, 66]. Only odd harmonics are included in the decomposition, since stress response is assumed to be a series consisting of only odd powers of strain. Nonlinear shear modulus are evaluated by comparing the relative amplitudes of the higher harmonics to the first harmonic (linear) response.

Rheology data in Chapters 5 and 6 are analyzed by fitting the averaged raw stresses up to the *third* harmonic in Fourier space. Shear moduli obtained in this manner from moderately strain-stiffening materials are similar to those calculated using MITlaos software (Version 2.1 Beta for MATLAB) [30, 31] and Lissajous analyses [161, 18]. Higher harmonic analysis (e.g., fifth harmonic) may be required for even stronger strain-stiffening.

2.1.2.2 Lissajous Analysis

Mathematically, any curve in 2D that can be expressed by the following set of parametric equations

$$x(t) = A_x sin(\omega_x t + \delta_x), \text{ and } y(t) = A_y sin(\omega_y t + \delta_y), \tag{2.1}$$

is called a Bowditch curve or Lissajous curve [154]. Note that a sinusoidal stress-strain ($\sigma - \gamma$) relation in the linear elastic regime, i.e., $\sigma = \sigma_0 sin(\omega t + \phi)$ vs. $\gamma = \gamma_0 sin(\omega t)$ can be naturally expressed in the Lissajous form. In the linear elastic case, the Lissajous curve has an elliptical form, as indicated by the red dots in Fig. 2.2(a). The data shown here is from a sample fibrin gel (2.5 mg/ml fibrinogen in T7 buffer), at $\omega = 0.1$ Hz and $\gamma = 0.03$.

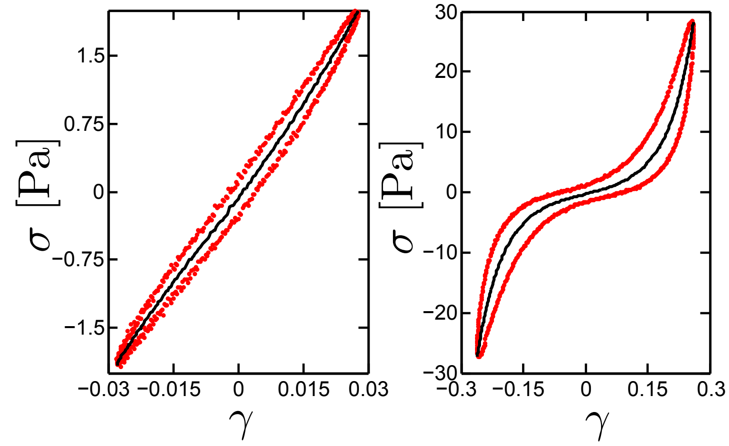

(a) (b)

Figure 2.2: Lissajous curves for a 2.5 mg/ml fibrin gel at (a) $\gamma = 0.03$, and (b) $\gamma = 0.3$.

Even when there is significant non-linear response, the response to the same simple sinosiodal strain signal is a stress that can be decomposed into a sum of odd harmonics of sine function of the form $\sum \sigma_i sin((2n+1)\omega t + \delta_i)$ [18], which is also in the Lissajous form. In the non-linear elasticity scenario, the shape of the Lissajous curve is significantly different from an ellipse though, as is shown in Fig. 2.2(b). Data shown in this figure is from the same fibrin gel at $\omega = 0.1$ Hz, but at higher γ (i.e., γ=0.3) that is well into the non-linear elastic regime.

In either case, one can plot the σ vs. γ relation in the Lissajous form over an entire deformation cycle (see Fig. 2.2(a),(b)). The elastic stress, σ' at a given γ is the average of the two σ at that γ in the Lissajous plot, as indicated by the black curve in Fig. 2.2(a),(b); the viscous stress, σ'' is the absolute difference between the applied σ and σ' [161]. The area enclosed by the Lissajous curve is representative of the magnitude of the viscous/loss response, i.e., the greater the area enclosed by the curve, the higher the loss modulus, and vice versa.

2.1.2.3 Differential Strain Measurements

Another method to measure non-linear elasticity is to impose a constant level of stress (or strain) and then superimpose a low-amplitude oscillatory deformation to obtain the so-called differential modulus, $K(\gamma, \omega)$, of the material in its strained state [33, 34]. For non-linear materials, K is strongly dependent on the pre-stress (or pre-strain) values.

2.1.2.4 Stress Response from Oscillatory Waveforms

Non-linear stresses needed to calculate the shear modulus at any given strain may be given by the peak values of the stress waveforms generated from sinosoidal strain waves like the one shown in Fig. 2.1(b)-(ii) [147]. For an in-depth comparison of different experimental techniques used for calculating non-linear elasticity in viscoelastic materials, see Yao, *et al.* [161].

2.1.3 Negative Normal Stress

Besides strain-stiffening, negative normal stresses are also observed in biopolymer gels [62, 66]. When subjected to shear deformation, biopolymer gels tend to pull the shearing surfaces toward each other. This inward pulling force is referred to as the negative normal stress [62]. In contrast, a polyacrylamide gel has negligible normal stress at small deformation. The negative normal stress is predicted to arise from the non-linear force-extension behavior of bio-polymer filaments. For an isotropic network of bio-polymers under shear, an equal number of network filaments may be expected to be bending and stretching, but because of the nature of the force-extension curve, the tensile force generated by the filaments under extension exceeds the compressive force generated by the bent filaments, leading to a net negative force that pulls the shearing surfaces inward. In contrast, polyacrylamide gels, the filaments of which are modeled as Hookean springs, would have the tensile and compressive forces cancel each other out, resulting in zero normal stresses. At large strain, PA gel generates positive normal stress, which tends to push the shearing surfaces away from each other [62], arising from hoop stresses [66]. The magnitude of positive normal stress in PA gels is much smaller than the shear stress [62]. However, the magnitude of negative normal stress in biopolymer gels is comparable to the shear stress and increases nonlinearly with the increasing strain [62, 66].

Under certain conditions, the magnitude of negative normal stress may even be larger than the magnitude of the applied shear stress [20, 66].

2.2 Affine Model of Elasticity

Using the affine assumption, both the linear elasticity and nonlinear strain-stiffening in hydrogels can be understood on the single molecule level as a direct consequence of the mechanical response of worm-like-chains (WLC) [145, 45, 93, 138]. Within this approach, the end-to-end distance of the WLC, i.e., R, in the cross-linked network is set to be the average distance between cross-linkers, L_c; L is the average contour length of polymer segments between two neighboring cross-linkers [45, 93]. Within this model, thermal agitations lead to transverse undulations, which cause the distance between the ends of a WLC to be smaller than the polymer length, i.e., $R < L$ [145, 93, 138]. Stretching a WLC, in other words, increasing R, is equivalent to pulling out the extra contour length and leads to a decrease in conformational entropy of the polymer [145, 93, 138]. The force to keep the end-to-end distance of a WLC at R may be written as [98]

$$F = \frac{k_B T}{l_p}[\frac{1}{4(1 - R/L)^2} - \frac{1}{4} + R/L], \tag{2.2}$$

where l_p is the persistence length quantifying the stiffness of a polymer. When $l_p << L$, a polymer is flexible; when $l_p >> L$, a polymer is very stiff, i.e., rod-like. Most biological polymers are semiflexible polymer with $l_p \sim L$. The relationship between l_p and L also determines mean-square end-to-end distance of a *free* WLC as:

$$\langle R^2 \rangle = 2 l_p L[1 - l_p/L(1 - e^{-L/l_p})], \tag{2.3}$$

When a network deforms affinely, each polymer is stretched by the same amount so that the end-to-end distance increases by an amount $\delta R = \gamma L_c$. The stress-strain relation in the model gel is then determined by the force-extension of a single WLC as

$$K' = \frac{d\sigma}{d\gamma} \sim \frac{dF}{dR}, \tag{2.4}$$

where K' is the differential elastic modulus.

For a flexible polymer, $\sqrt{\langle R^2 \rangle} = 2l_pL$. The end-to-end distance R, and hence L_c, are much smaller than the contour length, L, of the WLC due to the small l_p. Therefore, the stretching deformation $\delta R = \gamma L_c$ is much smaller than L for strains up to a few hundred percent, and Eq. 2.2 gives $F \propto R$, i.e., the force required to stretch a flexible WLC depends linearly on the extension for a very wide range of strain. According to Eq. 2.4, the linear part of the force-extension of single WLC gives rise to the linear elasticity of flexible polymer networks, i.e. $K' = d\sigma/d\gamma$ is a constant.

For semi-flexible polymers, R is comparable to the polymer length, because l_p and L are comparable. Thus, F is no longer a linear function of R but diverges as $1/(1 - R/L)^2$. The relationship between F and R for semiflexible polymers has been determined experimentally as $dF/dR \propto F^{3/2}$ [98]. This nonlinear force extension results in the strain-stiffening of semiflexible polymer gels [138, 93]. Following Eq. 2.4, the affine model predicts a nonlinear elasticity as $K' \propto \sigma^3/2$. This strain dependence of elastic modulus has been confirmed by experiments on actin gels [33]; similar strain-stiffening behavior has also been observed in gels of intermediate filaments, and fibrin protofibrils [138].

In addition to the entropic nonlinear elasticity of thermally undulating polymers, effects such as mechanical stretching and compression of stiff polymer segments between cross-linkers can also contribute to the elasticity of semiflexible and stiff polymer networks [45]. Such an affine mechanical stretching model can account for the elasticity of gels made of actin bundles and thick fibrin fibers [33].

2.3 Non-affine Deformation and Gel Elasticity

In spite of its successes in capturing features of both linear elasticity of flexible polymer gels and strain-stiffening of semiflexible polymer gels, the affine assumption is simplistic. In affine models, for example, interactions between polymers are ignored so that each polymer deforms independently without affecting their neighbors. Such a deformation can only occur under ideal conditions [23]. In reality, all material deformations are expected to be non-affine on some length-scale. Indeed, the effects of non-affine deformation has been observed in many materials, including foams, synthetic polymer gels, and some biological materials [23, 45, 155, 8, 116, 56, 13].

2.3.1 Origins of Non-affine Deformation

Many factors lead to non-affine deformation in hydrogels. Inhomogeneities can play a major role in the degree of non-affinity in polymer gels. Didonna and Lubensky demonstrated theoretically [23] that variations in local elasticity lead to spatially correlated non-affine deformation in random, elastic media. The magnitude of this non-affinity was predicted to be proportional to the variance in local elastic moduli [23]. Experiments [8] indicate that network inhomogeneities formed during sample preparation are a major source of non-affinity in flexible polymer gels such as PA gels. Fig. 2.3(a) is a schematic of some common network imperfections that can lead to inhomogeneities in flexible polymer gels: (a) closed loops of polymer chain, wherein a cross-linking unit is attached to the ends of the same polymer chain instead of connecting two chains together, (b) dangling polymer chain ends, (c) cross-links reacting among themselves instead of with polymer chains, and (d) polymer chain entanglements that tend to slip under external loading [22]. Inhomogeneity in cross-link and polymer concentrations may also occur during polymerization. The size of the inhomogeneities can range anywhere from tens of nanometers to a micrometer [48] which determines the non-affinity length-scale, i.e., the length-scale above which the gels deform affinely.

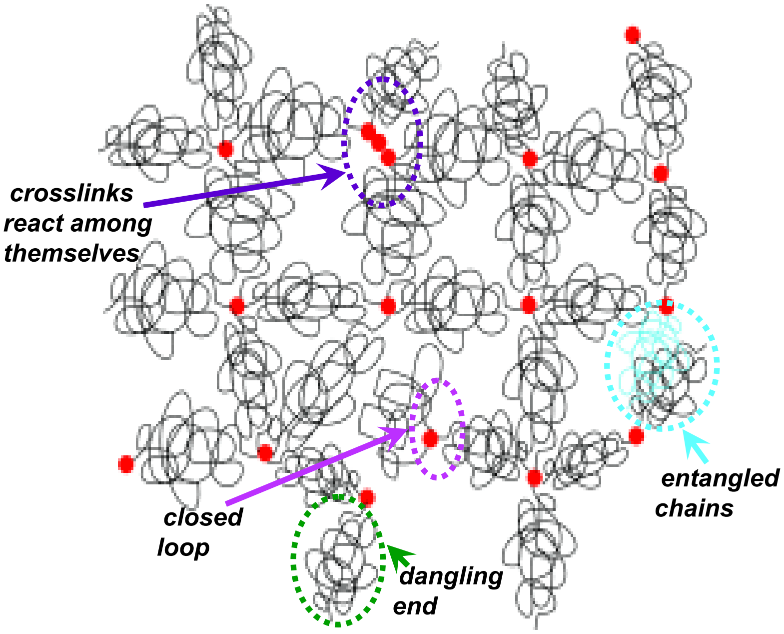

Figure 2.3: Inhomogeneities in cross-linked polymer gels.

Inhomogeneities are not restricted to flexible polymer gels only. Semiflexible polymer networks, be they *in vivo* collagen scaffolds [49], or *in vitro* fibrin gels [74], may have an additional sources of non-affinity, *viz.*, spatial inhomogeneity in the gel. Microscopic inhomogeneities in gels lead to fluctuations in the local elastic modulus and cause the gel to deform non-uniformly under shear. Such inhomogeneities may be inherent, or may depend on deformation protocols [36, 90]. Deformations larger than the average size of these inhomogeneities are seen to be essentially affine [49].

Experimentally, observed deformations in a polymer gel under external load can be affine or non-affine depending on the length-scale examined [125]. Different polymer gel classes have different "important" length-scales, *viz.*, persistence length of the constituent polymers, end-to-end length of filaments, mesh-size, etc.

For an isotropic, cross-linked polymer network [47, 45], the macroscopic elasticity parameters like the shear and the Young's moduli can be seen to depend on the bending and stretching moduli, i.e., κ and μ, respectively, of the constituent polymer filaments. For a filament of arc length, s, the total length, $\delta l(s)$, the Hamiltonian per unit length, δs in the simplified linear regime can be written as

$$\frac{\delta \mathcal{H}}{\delta s} = \frac{\mu}{2}\left(\frac{\delta l}{\delta s}\right)^2 + \frac{\kappa}{2}\left(\frac{\delta \theta}{\delta s}\right)^2, \tag{2.5}$$

where $\theta(s)$ is the angle the filament makes at s with the $\hat{x}$ axis. In the limit $\kappa \to 0$, the system becomes a network of flexible polymers where all network deformations occur through stretching of individual polymer filaments. At the other extreme, when $\kappa \to \infty$, the energetic cost of filament bending is prohibitive and network deformations are again stretching-dominated. In the intermediate regime, however, there is a transition from bending-dominated to stretching-dominated deformation as the ratio of κ/μ decreases. For such isotropic, cross-linked polymer networks, there is an intrinsic non-affine length-scale, $\lambda = l_c(l_c/l_b)^{1/3}$ [47, 45], depending on gel morphology. Here, l_c is the average length of polymer chain between cross-links, and $l_b = \sqrt{\kappa/\mu}$. The affinity of network deformation is then determined by the relationship between filament length and λ. At large l/λ, i.e., when the network is highly crosslinked, network deformation is affine. Conversely, for a loosely crosslinked network, l/λ is small and deformation is non-affine.

Biopolymer filaments can bundle together under certain conditions, e.g., pH [128] and shear [66]. Formation of bundles changes the value of l_b, and hence, the mode of deformation in the locality of the bundles. Of course, a polymer network with filament bundles randomly interspersed must be inhomogeneous on the length-scale of the filament bundles. The non-affinity measure is also affected by the applied strain: under extensional forces, non-affinity has been measured to increase with increasing strain [36], and under shear, non-affinity decreases as strain increases [155].

Simulations of 2D athermal networks of rigid rods [115] mimic gels consisting of stiff polymer filaments. Under shear, such a system exhibit filament-bending at low strains, and network rearrangements under high strains, both causing non-affine deformations. Such shear-induced network rearrangements are depicted in Fig. 2.3(c). Network rearrangements were observed in collagenous tissue, albeit under uniaxial extension [36], especially when loaded perpendicular to the natural occurring alignment of collagen fibers; here, the stiff fibers reoriented *en masse* to align with the direction of extension. Such non-affine bending and rearrangement in (non-covalently bonded) stiff collagen filaments that form the underlying substrate have been shown to have profound effects on the shape, proliferation and motility of mammalian cells [146].

There are yet other sources of non-affine deformation. The effect of network connectivity on elasticity and non-affinity has been investigated by Broedersz, *et al.* [11] using a lattice-based model of stiff rods with variable connectivity. In addition, loading history [36], pre-shear conditions [90], and gelation kinetics [8], also have influence on gel morphology and hence non-affinity measures.

2.3.2 Gel Elasticity Due to Non-affine Deformation

Over the years, there has been continued effort in determining the consequence of non-affinity in polymer gels. Rubinstein proposed a model based on microscopic non-affine deformations to account for the nonlinear elasticity of polymer networks. In an entangled network, each polymer is confined within a tube-like region due to the steric interaction with its neighbors [28]. Within the tube, the polymer deforms non-affinely by changing its conformation. The effect of steric interaction between neighboring polymers is then considered as the confining potential imposed by such a tube. Therefore, besides the conformational entropy, this confinement also alters the effective elasticity of a polymer [27, 125]. Rubinstein and Panyukov found that the size of the confining tube, and hence the confining potential, changes non-affinely with external deformation [125]. As a result of such a non-affinely varying confining potential, Rubinstein, *et al.* [125] demonstrated that the microscopic non-affine deformation leads to a nonlinear stress-strain relation similar to the empirical Mooney-Rivlin relation for flexible polymer networks at large deformations.

For semi-flexible and stiff polymer networks, in addition to the confining tubes, the finite stiffness of polymers should be considered. In these networks, such as a highly crosslinked isotropic network of actin, a single polymer of length, l, can be crosslinked multiple times, say n, such that the average length of the polymer segments between crosslinkers is $L_c = l/n$. The deformation of segments that belong to a single actin filament should be correlated due to the bending rigidity of the filament. The ratio of effective spring constant for filament-stretching to the spring constant for filament-bending, which is proportional to l_p/L_c, determines the details of network deformation [157, 45]. When $L_c >> l_p$, as in a sparsely cross-linked network, it is much easier to stretch a filament than to bend it. In contrast, if $L_c << l_p$, as in stiff filament networks or highly crosslinked semiflexible polymer networks, stretching a filament is much harder than bending one. Filament bending causes “floppy modes” in the network [157], which give rise to the non-affine network deformation [157, 57]. Rather than the nonlinear stretching of filaments, geometric effects such as the transition from filament bending/buckling dominated non-affine network deformation to a stretching dominated affine deformation may also give rise to the strain-stiffening [115, 50, 12]. For sufficiently large strains, however, filament-buckling may even lead to a *decrease* in elasticity of actin gels [14]; this decrease is reversible in that the filaments will unbuckle when the strain is released. When L_c and l_p are comparable, both affine filament-stretching and non-affine filament-bending contribute to network deformations [47, 57].

Chapter 3

Instrumentation and Data Analysis

3.1 Experimental Setup: Confocal Rheoscope

The setup used for non-affinity measurements consists of a Bohlin Gemini rheometer (Malvern Instruments, UK) coupled through home-built extensions to an Eclipse TE200 inverted optical microscope (Nikon Instruments, USA) with (or without in Chapter 5) a VTEye laser-scanning confocal unit (VisiTech International, UK), as shown in Fig. 3.1(a). The setup can be briefly described as follows: The entire setup sits on an air-floated optical table (not shown in the picture). This consists of (a) a top table (See Fig. 3.1(a)) on which sits the rheometer, and (b) a home-built xy-stage on which the microscope and the confocal unit are placed.

The rheometer is placed on a small sliding table on rails on the top table. The sliding table and therefore the rheometer can be moved *away from* and *to* the position immediately atop the microscope, for easy sample-loading and microscopy, respectively. Central sections of the top table and the sliding table are cut out such that the rheometer can reach down to sample holder.

The sample holder is an extension of the top table that sits immediately above the microscope objective (Fig.3.1(b)). It consists of a glass window, the schematic of which is shown in Fig.3.1(c). Note that the sample holder is a part of the top table and its position is essentially fixed with respect to the rheometer; the microscopy unit (microscope and confocal) that sits on the lower xy-stage is physically isolated from the rheometer and the sample holder.

The lower xy-stage can be maneuvered using a micrometer positioning stage (Del-Tron Precision, Inc., USA) such that the microscope and confocal can be moved together as a single unit, relative to the top table or the sample being imaged.

Home-built extensions include a glass window (schematic shown in Fig.3.1(c)), and an extension rod (schematic, Fig.3.1(d)). The window holder for the glass window is machined in-house using aluminum. $No.1.5$ microscope cover-slips (Corning Life Sciences, USA) are glued to the aluminum window holder using UV curing adhesives (Norland Products Inc., USA). All microscope objectives that were used in these experiments have adjustable correction collars to accomodate the cover-slips used in the glass window.

The lower plate of the rheometer is taken off to be replaced by the glass window described previously. The position of the glass window on the top table is too far for the top plate of the rheometer to reach the glass window. To compensate for this difference in distance, we use the home-built extension rod shown in Fig. 3.1(d). The extension rod is made of aluminum to keep the overall weight of the rheometer tool low ($\lesssim 40$ gm).

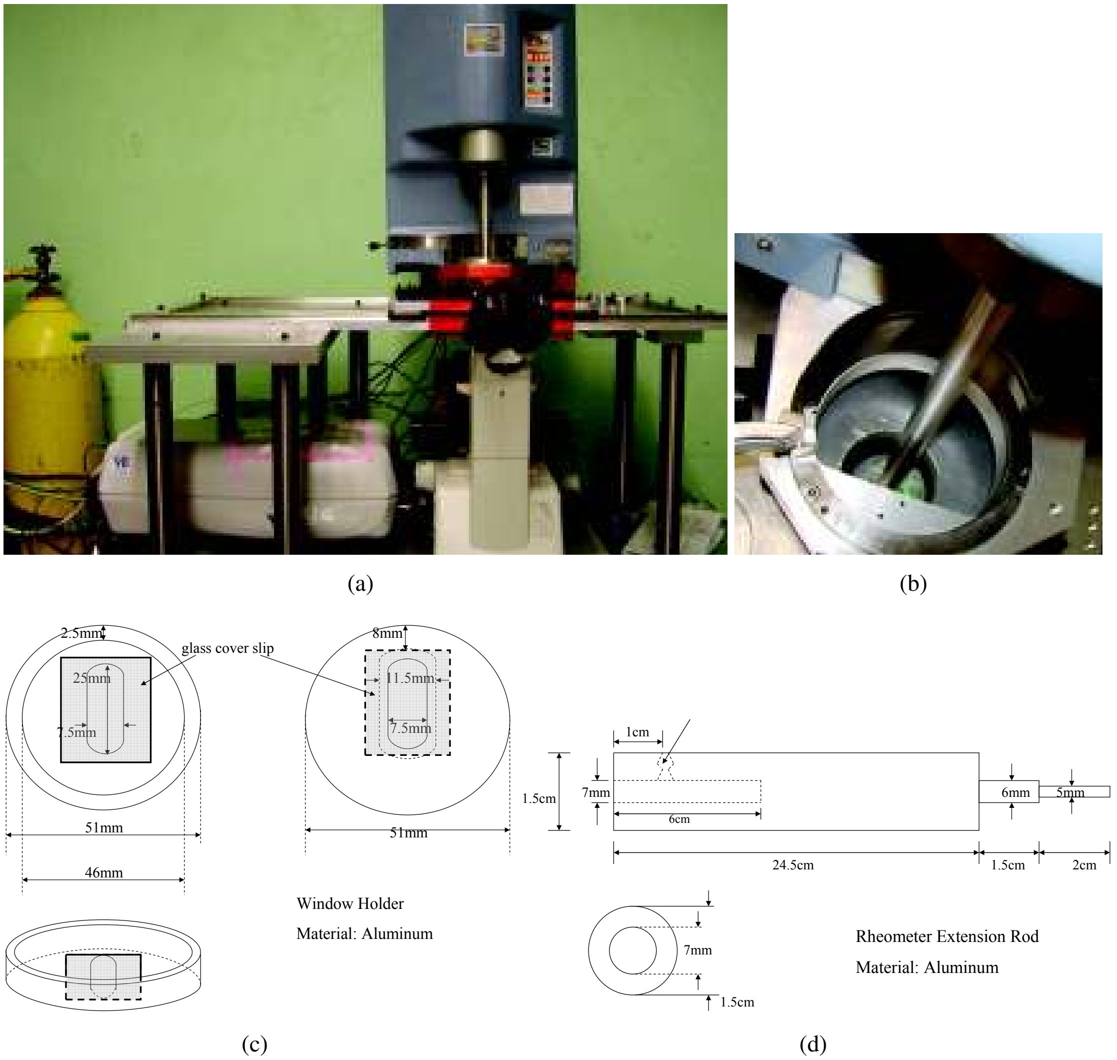

Figure 3.1: Experimental setup for confocal rheometry. Rheometer sits on the top table sits an inverted optical microscope. The confocal unit is coupled with the microscope on the right, on the main optical table. (b) Rheometer extension rod reaching down to the glass window. Schematics of the (c) glass window, and (d) extension rod.

3.1.1 Confocal Microscopy

The set-up described above is used to study microscopic deformation of the gel samples under shear by tracking the displacements of tracer bead entrapped in the gels using fluorescence confocal microscopy. Note that non-affine displacements are not restricted in the xy plane only; one needs sufficient spatial resolution in the z axis to accurate capture the entire breadth of non-affine motions. As seen from the previous chapter, the generation of normal forces in semiflexible polymers under shear also lead to significant out-of-plane motions of the tracer beads, that need to be sufficiently resolved along the z direction. While a regular microscope offers sufficient spatial resolution ($\sim$ 50 nm) in te xy-plane, there is limited resolution in the out-of-plane or z-axis. A confocal microscope improves on an ordinary fluorescent microscope by placing a pin-hole in front of the microscope objective that allows signal from only a limited focal depth to reach the objective. Fig.3.2 shows a schematic for confocal imaging proposed by Marvin Minsky in the original patent filing in 1957 [103]. Note the presence of two pin-hole apertures in the set-up–

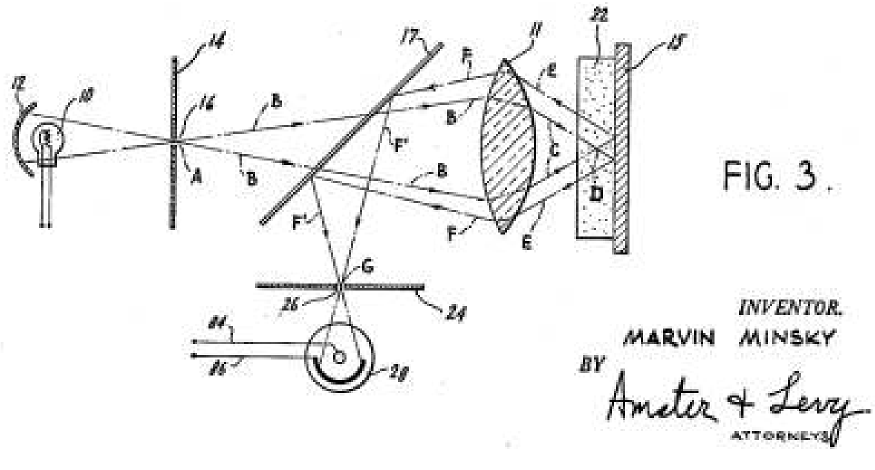

Figure 3.2: Schematic depicting the confocal microscopy principle from the original patent filed by Marvin Minsky in 1957.

the pin-hole marked as ‘16’ in the figure provide point-source illumination, while pin-hole ‘26’ limits the depth of focal plane being imaged.

These days, the point source illumination is easily provided by a well-collimated laser beam; high illumination intensities from lasers also compensates for the loss of signal intensity due to the presence of the pin-hole aperture in the confocal microscope. Because of the limited volume that is sampled through the pinhole, the incident laser beam scans the sample both in 2D and 3D. These scanned images, each limited to a narrow focal depth, are then reconstructed to generate a 3 dimensional volume of image. The particular confocal apparatus used in our set-up is a laser scanning confocal microscope, where a set of mirrors are used to raster-scan the incident laser beam in x and y axes. The focal depth (i.e., along the z axis) is changed in step-wise form by mounting the microscope objective mounted on a piezo-electric actuator (E-662 LVPZT Amplifier/Servo, Physik Instrumente, Germany).

Fluorescently labeled polystyrene (PS) micro-beads (≈ 1 μm diameter) are used for tracking non-affine displacements in different polymer gels. The lower plate of the rheometer is replaced by a home-built transparent sample holder through which the gels are imaged using the confocal microscope. The overall experimental schematic is depicted in Fig. 3.3(a).

A $60\times$ water objective (NA = 1.2) is used to visualize the sample over a depth of 100 μm. 3D stacks of images map the entrapped tracer beads (70 μm $\times$ 70 μm $\times$ 50 μm) using the confocal setup with and without shear. 3D stacks with a step-size of 150 nm are taken for 1 μm tracer beads. (Stack step-sizes are changed according to tracer-bead size, *viz.*, 100 nm for 0.6 μm bead, 150 nm for 1 μm bead, and 200 nm for 1.5 μm bead.) A range of shear strain, up to 50% amplitude, is applied. Three dimensional stacks of tiff images (unless otherwise mentioned) are

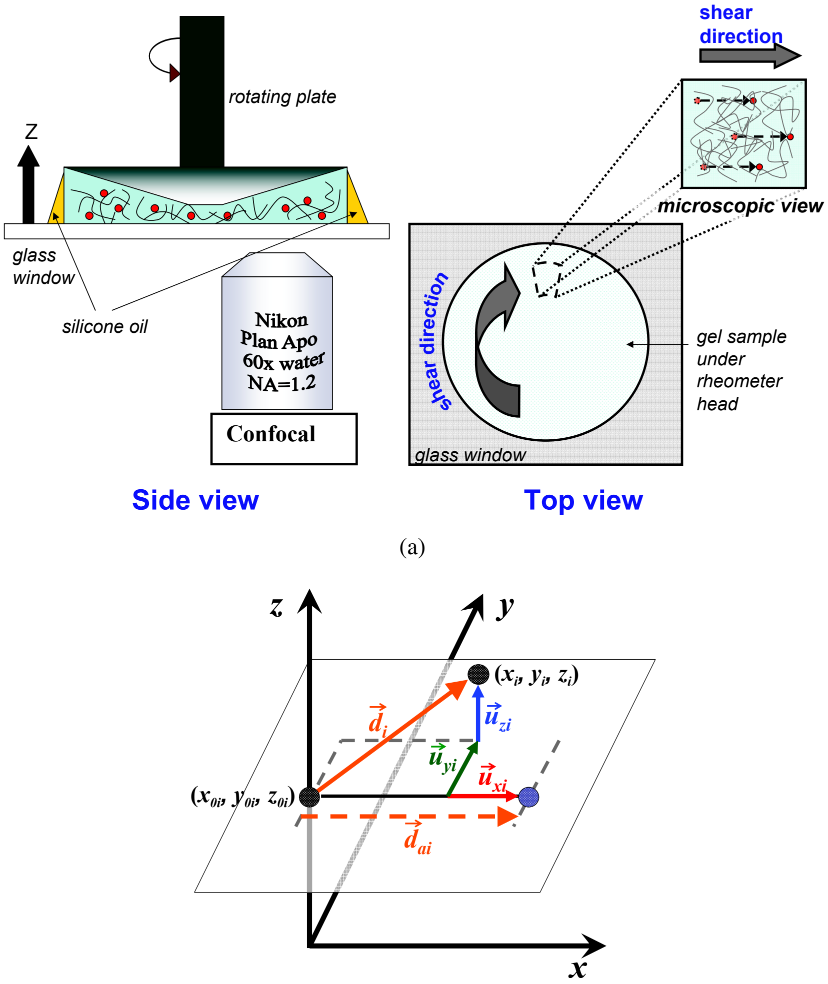

(a)

(b)

Figure 3.3: Experimental Setup. (a) Experimental schematic. (b) Sketch of the non-affine displacements of tracer beads. (x_{0i}, y_{0i}, z_{0i}) and (x_i, y_i, z_i) mark the positions of a tracer bead without and under shear, respectively. Dashed arrow indicates affine displacement, $\vec{d}_{ai}$, of tracer bead in the direction of shear (x-axis). $\vec{d}_i$ is the measured displacement of the tracer bead. $\vec{u}_{xi}$, $\vec{u}_{yi}$, $\vec{u}_{zi}$ indicate the non-affine deviations along the x, y and z axes respectively. $\vec{u}_i = \vec{d}_{ai} - \vec{d}_i$ is the non-affine deviation.

acquired using VoxCell Scan software from VisiTech International, UK.

The image stacks are processed using standard Matlab routines which determine the beads' position with subpixel accuracy [21, 32]. For each stress value, a set of two image stacks are taken, one with shear and one without. The 3D locations of beads in a gel without external shear stress are determined as (x_{0i}, y_{0i}, z_{0i}), for $i = 1, 2, \ldots, N$, where N is the number of tracked beads. On average, 35 beads are tracked in each 3D stack. The stacks are analyzed to find the centroid of the tracer beads using Matlab routines: $bpass3d.m$, $pkfnd3.m$, and $cntrd3.m$ [10]. The centroids of the corresponding N beads in the image stack under shear stress are measured too, as (x_i, y_i, z_i); for convenience the direction of shear is along the $\vec{x}$ axis. The displacements of tracer beads are then calculated from the tracking results as $\vec{d_i} = (x_i - x_{0i}, y_i - y_{0i}, z_i - z_{0i})$. The system permits the displacements of tracer beads to be measured with a spatial resolution of 50 nm.

3.1.2 Non-affine Parameter

A simple measure of the degree of non-affinity is provided by the non-affine parameter $\mathcal{A}$, which is defined in Ref. [23]:

$$\mathcal{A} = \frac{1}{N} \sum_{i=1}^{N} |\vec{u}_i|^2.$$

Here $\vec{u}_i = \vec{d_i} - \vec{d_{ai}}$, is the deviation of the measured tracer-bead displacement, $\vec{d_i}$, from the affine displacement, $\vec{d_{ai}}$ [Fig. 3.3(b)]. This definition is similar to the definitions of non-affine parameters used in a range of different systems, e.g., foams [78], semi-flexible networks [47, 155, 90, 115, 55], etc.

For a perfect shear deformation along the x-axis, the affine displacement $\vec{d_{ai}}$ would be in the direction of shear only– the y and z components must be zero. We measure the resultant strains along all three component axes, γ_x, γ_y and γ_z by fitting the x, y and z components of d_i to linear functions of z_{0i}. The real strain on the sample is determined as $\gamma = \sqrt{\gamma_x^2 + \gamma_y^2 + \gamma_z^2}$. The x, y and z components of the affine displacement vector, $\vec{d_{ai}}$ are then calculated as $z_{0i}\gamma_x$, $z_{0i}\gamma_y$, and $z_{0i}\gamma_z$. Note that the y and z components, both perpendicular to the direction of shear, do not vary as a function of z_i, resulting in γ_y and $\gamma_z \approx 0$. $|\vec{u}_i|^2$ is calculated as $(x_i - x_{0i} - \gamma_x z_{0i})^2 + (y_i - y_{0i} - \gamma_y z_{0i})^2 + (z_i - z_{0i} - \gamma_z z_{0i})^2$.

$\mathcal{A}$ may be defined in terms of these variables as

$$\mathcal{A} = \frac{1}{N}\sum_{i=1}^{N}[(x_i - x_{0i} - \gamma_x z_{0i})^2 + (y_i - y_{0i} - \gamma_y z_{0i})^2 + (z_i - z_{0i} - \gamma_z z_{0i})^2]. \tag{3.1}$$

Additionally, two-point non-affinity correlation function, $\mathcal{G}_{ij}(r - r')$ that measures the non-affinity correlation between two tracer-beads located at $r = (x, y, z)$ and $r' = (x', y', z')$,(also used in [23, 8]) is defined:

$$\mathcal{G}_{ij}(r - r') = \left\langle \vec{u}_i(r) \cdot \vec{u}_j(r') \right\rangle$$

$$= \left\langle [\vec{u}_x \cdot \vec{u}_{x'} + \vec{u}_y \cdot \vec{u}_{y'} + \vec{u}_z \cdot \vec{u}_{z'}] \right\rangle. \tag{3.2}$$

Chapter 4

Shear Deformation in Flexible Polymer Gels

This chapter measures macroscopic shear elasticity and quantifies non-affine shear deformations in a model flexible polymer gel. Polyacrylamide gels with bisacrylamide cross-linkers are used for this purpose. Polyacrylamide is particularly well suited for this investigation because it is a widely studied and well-characterized system that is comparatively well-controlled and its stiffness is tunable by bisacrylamide cross-links. The confocal rheoscope described in Chapter 3 is used for this purpose. Deformation fields in gels under external shear stress are characterized by measuring the displacements of fluorescent beads entrapped in the gels, also described in Chapter 3. $\mathcal{A}$, as defined before, is measured as a function of bead size and cross-link density in the gels, at two different polymer concentrations. Following the lines of a recently developed theory on random elastic media [23], we estimate the fluctuations in elastic modulus of the gels from $\mathcal{A}$.

4.1 Experimental Procedure

4.1.1 Sample Preparation

The polyacrylamide (PA) gel is prepared by polymerizing acrylamide monomers (Fig. 4.1(a)) and methylenebisacrylamide (bisacrylamide or bis) cross-links (Fig. 4.1(b)) in aqueous 50 mM HEPES buffer at pH $= 8.2$, using free-radical polymerization reaction, initiated and catalyzed by 0.3% w/w N, N, N', N'- tetramethylethylenediamine (TEMED) and 0.1% weight/weight (w/w) ammonium persulphate (APS), respectively. Here the percent of X w/w equals the mass in grams of X per 100 grams of solution. Fluorescent tracer beads are mixed into our solution at a concentration of 0.004% weight per volume (w/v), before the addition of bis cross-links. (Here the percent of X w/v equals the mass in grams of X dissolved/suspended in 100 milliliters of solvent.) Thus, a tracer bead concentration of 0.004% w/v is attained by dissolving 0.004 gram of tracer beads in 100 milliliters of water. This procedure helps to distribute the beads uniformly throughout the polymer network. Internally labeled and carboxylate-modified fluorescent polystyrene micro-spheres of various diameters are used for this purpose, viz., 0.6 μm, 1 μm (Molecular Probes, California, USA), and 1.5 μm (Bangs laboratories Inc., Indiana, USA). Acrylamide (7.5%, 15% w/v and bisacrylamide (0.03 - 0.12%w/v) concentrations are systematically changed to study the effects of polymer concentration, cross-link density and mesh size on the polymer network rheology.

4.1.2 Rheology

Rheology measurements are performed using a stress-controlled Bohlin Gemini rheometer, with a cone and plate geometry of 4° cone angle and 20 mm diameter. Samples are prepared *in situ* so

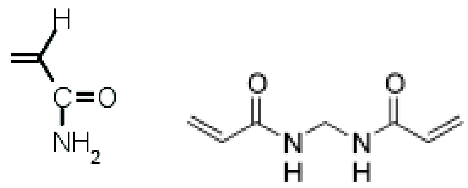

(a) (b)

Figure 4.1: Chemical structures of unreacted (a) acrylamide, and (b) bisacrylamide.

that good contact is routinely established between the sample surfaces and the rheometer plates to prevent slippage at high strains. The shear modulus (G') and loss modulus (G'') for each sample during the process of polymerization are monitored using low strain amplitude (γ_0= 0.01) and low frequency ($f = 0.1$ Hz) oscillatory shear measurements. The polymerization reaction proceeds for ~ 30 minutes, with the elastic and viscous moduli attaining steady-state values in less than 10 minutes. Care is taken to prevent solvent evaporation by sealing off the sample from the sides with a low density, low viscosity (~ 50 mPa·s) silicone oil. The elastic and viscous moduli, G' and G'', respectively, for these gels are measured as functions of frequency, amplitude and temperature. These measurements are intended to confirm that the gels behave in accordance with the existing theories of flexible polymer networks [145]. A set of control experiments are performed on the PA gels, with and without the tracer beads, to further confirm that macroscopic properties of the gels are not altered by the addition of the tracer beads. A wide range of shear strain, up to 50% amplitude, is applied.

4.1.3 Non-affinity Measurements

To quantify the degree of non-affinity in PA gels, we will use the Confocal Rheoscope setup, procedure and the non-affine parameter $\mathcal{A}$ introduced in Chapter 3:

$$\mathcal{A} = \frac{1}{N}\sum_{i=1}^{N}|\vec{u}_i|^2 = \frac{1}{N}\sum_{i=1}^{N}[(x_i - x_{0i} - \gamma_x z_{0i})^2 + (y_i - y_{0i} - \gamma_y z_{0i})^2 + (z_i - z_{0i} - \gamma_z z_{0i})^2].$$

For a perfect shear deformation, the affine displacement $\vec{d_{ai}}$ would be solely in the direction of shear (or the x-axis by construction); the y and z components must be zero. We measure the resultant strains along all three component axes, γ_x, γ_y and γ_z by fitting the x, y and z components of d_i to linear functions of z_{0i}, as seen from a sample PA gel (7.5% acrylamide, and 0.03% bis) under an applied strain of $\gamma\ = 0.3$ in Fig. 4.2(a). The real strain on the sample is then $\gamma = \sqrt{\gamma_x^2 + \gamma_y^2 + \gamma_z^2}$. The x, y and z components of the affine displacement vector, $\vec{d_{ai}}$ are calculated as $z_{0i}\gamma_x$, $z_{0i}\gamma_y$, and $z_{0i}\gamma_z$. Note that the y and z components, both perpendicular to the direction of shear, do not vary as a function of z_i, resulting in γ_y and $\gamma_z \approx 0$. Fig. 4.2(b) plots the distribution of non-affine deviations, $\vec{u}_x$, $\vec{u}_y$, and $\vec{u}_z$ for the same sample gel, along the x, y, z axes respectively, for the same strain of $\gamma\ = 0.3$ as seen in Fig. 4.2(a).

4.2 Results

4.2.1 Bulk Rheology Measurements

The PA gels used in our experiments are solid-like materials with G' ranging from 7.7×10^2 Pa to 1.5×10^4 Pa, 2 to 3 orders of magnitude larger than the G''. In Fig. 4.3(a), G' and G'' of a gel made of 7.5% acrylamide and 0.06% bisacrylamide are plotted as functions of the amplitude of

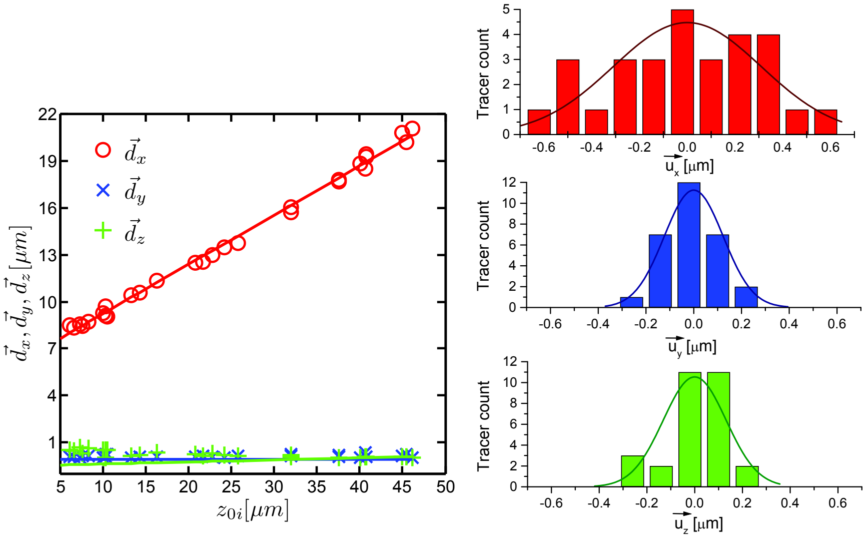

(a) (b)

Figure 4.2: (a) Experimentally measured displacements of tracer beads in the direction of shear, $\vec{d_i}$, that has been decomposed along x-(red circles), y-(blue crosses) and z- (green pluses) axes, as a function of the distance, z_{0i} from the fixed lower plate of the rheometer. This sample is 7.5% acrylamide and 0.03% bis PA gel. The solid lines give the strains, γ_x, γ_y, and γ_z obtained from their linear fits. Note that γ_y, and γ_z are ≈ 0. (b) The distribution of non-affine deviations of tracer beads for the same sample PA gel shown in Fig. 4.2(a), at $\gamma = 0.3$, decomposed along the x-, y- and z- axes. The measurements are normally distributed around the *affine* displacement position, as indicated by the solid curves.

the oscillatory shear strain at oscillation frequency, $f = 0.1$ Hz. G' is approximately 100 times larger than G''. Moreover, both G' and G'' are independent of the applied shear strain for strains up $\gamma = 0.5$, confirming the linear elastic response of PA gels. The frequency response of PA gels is characterized by measuring G' and G'' at oscillatory strains with amplitude $\gamma_0 = 0.01$ and frequency ranging from 0.1 Hz to 100 Hz. Within this frequency range, G' remains constant, and G'' increases with increasing frequency, as shown in Fig. 4.3(d).

The elastic moduli of our PA gels vary linearly with bisacrylamide concentration and sample temperature. Cross-link and monomer concentration trends are shown in Fig. 4.3(b). Notice, when the bisacrylamide concentration increases from 0.03% to 0.12%, G' for gels with 7.5%

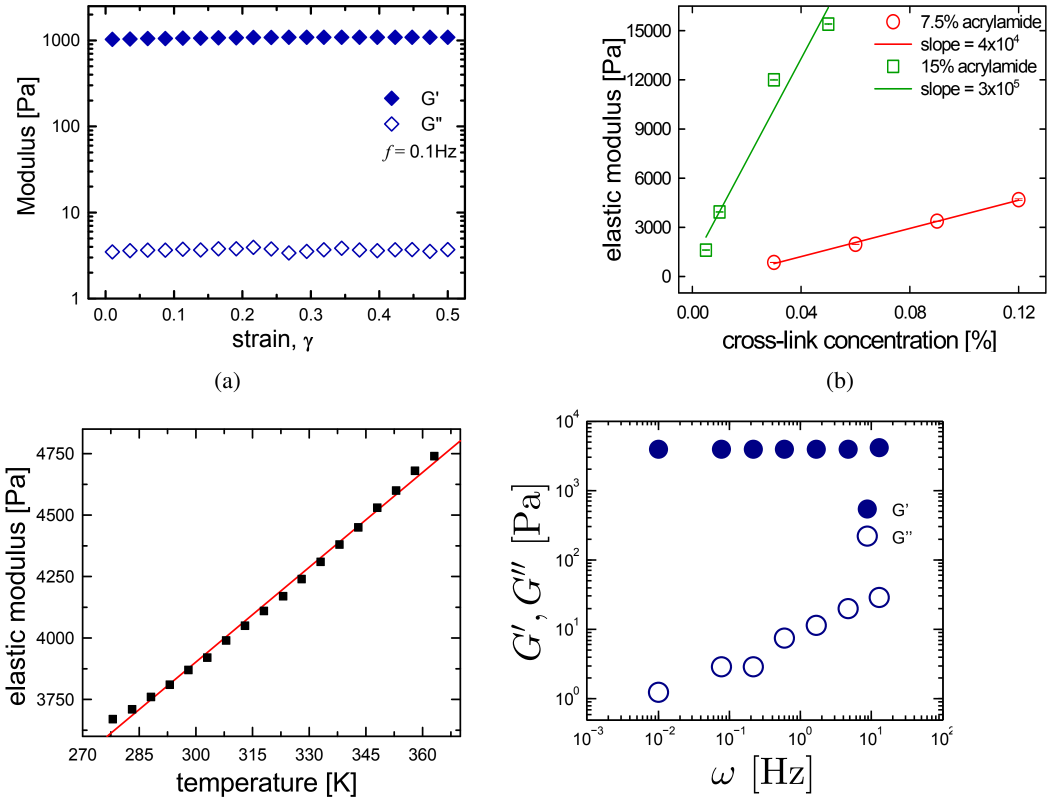

(a) (b) (c) (d)

Figure 4.3: Rheology of polyacrylamide gels. (a) G' of sample PA gel is two orders of magnitude larger than the G'' and theses values remain constant over a wide range of applied strain. Data are shown for a gel with 7.5% acrylamide at 0.03% bisacrylamide cross-link concentration, at an oscillatory frequency of 0.1 Hz. (b) G' of 7.5% and 15% polyacrylamide gels as a function of cross-link concentrations. Error bars denote standard deviations which are less than 2% of the mean elastic moduli. The solid lines indicate linear fits to the data. Note that the overall moduli of the gels with 7.5% acrylamide are significantly lower than that of 15% acrylamide for comparable cross-link density. (c) G' as a function of temperature (red line is the linear fit). (d) G' and G'' as functions of oscillatory frequency, ω. Data are shown in (c) and (d) for a PA gel with 7.5% acrylamide with 0.09% bisacrylamide.

acrylamide increases linearly from 7.7×10^2 Pa to 4.9×10^3 Pa. Similarly, G' for 15% acrylamide PA gels increases from 1.6×10^3 Pa at 0.005% bis concentration to 1.5×10^4 Pa at 0.05% bis concentration. We also investigated the temperature dependence of the network elasticity within the attainable temperature range of the rheometer, i.e., $5°\text{C} < T < 90°\text{C}$. In Fig. 4.3(c), we show that G' from the gel made of 7.5% acrylamide and 0.09% bisacrylamide increases linearly with sample temperature. This linear dependence of G' on cross-link concentration and sample temperature follows the predictions of classical rubber elasticity theory. Note that the slope of the linear fit of G' as a function of cross-link concentrations for the 7.5% acrylamide is lower than that of 15% acrylamide PA gels. We suggest that some bis molecules form efficient cross-links and others do not, and that this difference in the slope of G' versus cross-link concentrations for 7.5% and 15% acrylamide is due to the difference in effectiveness of the bis molecules in forming efficient cross-links, which increases with increasing monomer concentration. We discuss these effects further in Section 4.3.1.

4.2.2 Non-affine Parameter, $\mathcal{A}$ Scales as the Square of the Applied Strain

Confocal microscopy is used to visualize and record the displacements of the fluorescent tracer beads entrapped within a ($70\ \mu\text{m}\times70\ \mu\text{m}\times60\ \mu\text{m}$) volume in the PA gel. Since the tracer beads' size of $\sim 1\ \mu m$ is much larger than the average mesh size of the PA gel, free Brownian motion is suppressed. Within this small volume, located approximately 1 cm from the axis of rotation, the macroscopic shear strain applied to the beads can be approximated to be unidirectional.

In Fig. 4.2(a), bead displacements along the x, y, and z axis, are plotted as a function of z_{0i}, the distance between the beads and the bottom surface. The displacements along the direction of

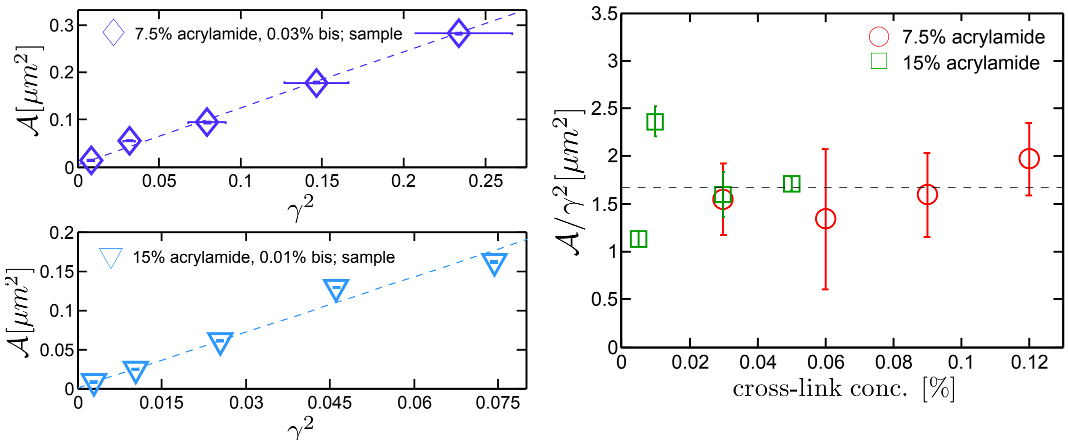

(a) (b)

Figure 4.4: (a) The non-affine parameter scales as the square of the external strain field, as seen for sample polyacrylamide gels at 7.5% acrylamide and 0.03% bis (top), and 15% acrylamide and 0.01% bis (bottom). The dashed lines give best linear fits to the data. Error bars represent standard deviation of measurements of strain and non-affinity, the latter being smaller than symbol size. (b) Strain-normalized non-affine parameter, $\frac{\mathcal{A}}{\gamma^2}$ for sample PA gels at 7.5% and 15% acrylamide are plotted at varying bis concentrations. The data points and error bars represent the average value and standard error of measurements from different samples prepared in the same manner. The dashed line indicates the average $\frac{\mathcal{A}}{\gamma^2}$ calculated from all data points in the figure.

shear, *viz.*, the x-axis, increase linearly with z_{0i}, as expected from macroscopic shear deformation. Fitting d_x to a linear function of z_{0i} yields the strain $\gamma_x \approx \gamma$. d_y and d_z, both perpendicular to the shear direction, are independent of z_{0i} as shown in Fig. 4.2(a). Also notice from Fig. 4.2(b) that the non-affine displacements along each axis, *viz.*, $\vec{u}_x$, $\vec{u}_y$ and $\vec{u}_z$, are much larger than the resolution of our system in the $xy-$ plane ($\sim$ 50 nm) and comparable to that along the z axis ($\sim$ 80 nm) and are normally distributed with mean value zero, i.e., distributed around the affine displacement positions. These uncertainties in tracking lead to a noise floor in $\mathcal{A} \sim 0.007\mu m^2$.

The non-affine parameter $\mathcal{A}$ is readily computed from the measured bead displacements using Eq. (3.1) for PA gels (7.5% and 15% acrylamide and a range of bisacrylamide concentrations). In Fig. 4.4(a), $\mathcal{A}$ increases with applied strain γ, and clearly scales as γ^2.

In Ref. [23], DiDonna and Lubensky developed a perturbation theory for non-affine deformations in solids with random, spatially inhomogeneous elastic moduli. They characterized the non-affine deformations using the non-affinity correlation function

$$\mathcal{G}_{ij}(x, x') = \langle \vec{u}_i(x) \vec{u}_j(x') \rangle, \tag{4.1}$$

where $u(x)$ is the nonaffine displacement field, and $\langle \cdot \rangle$ represents the average over randomness in the elastic moduli (i.e., a disorder average). Because the disorder averaged quantities are translationally and rotationally invariant in the gel we consider, the correlation function only depends on the distance $|x - x'|$, and thus it is characterized by the Fourier transform $\mathcal{G}(q) \equiv \int d(x - x')\mathcal{G}_{ii}(x, x')e^{-iq\cdot(x-x')}$. In Ref. [23] it is proved that this correlation function is related to the correlation function of the inhomogeneous elastic modulus K as

$$\mathcal{G}(q) \sim \frac{\gamma^2 \Delta^K(q)}{q^2 K^2} \tag{4.2}$$

where K is the disorder averaged elastic modulus, and $\Delta^K(q)$ is the Fourier transform of the spatial correlation function of the elastic modulus K.

In this theory, the zeroth order problem concerns elastic deformations in a homogeneous media of elastic modulus K, and the randomness in K is treated as a perturbation from this homogeneous state. To first order, the driving forces of the non-affine deformations are thus proportional to the zeroth order deformations, which are proportional to γ. Therefore, to first order in perturbation theory, $\mathcal{G}(q)$ is proportional to γ^2.

We have shown in the Supplementary Online Material in Ref. [8] that the two-point non-affinity correlation function, $\mathcal{G}_{ij}(x, x')$ decays as $1/|x - x'|$, where $(x - x')$ is separation between tracer-beads in the PA gel samples [23]. For typical tracer-bead concentrations used in our experiments, the smallest separation between tracer-beads is of the order of several microns, for which the $\mathcal{G}_{ij}(x, x')$ falls below our experimental noise floor. Thus, our tracer-bead concentration does not permit us to perform two-point non-affinity correlation analysis at any meaningful length-scales (e.g., length scales of inhomogeneities in PA gels, mesh-size, etc. which are all $\lesssim$ 200 nm).

The non-affine parameter $\mathcal{A}$ defined in the present experiment corresponds to $\mathcal{G}_{ii}(x, x)$,

$$\mathcal{A} = \mathcal{G}_{ii}(x, x) = \int \frac{d^3q}{(2\pi)^3}\mathcal{G}(q) \sim \int \frac{d^3q}{(2\pi)^3}\frac{\gamma^2\Delta^K(q)}{q^2K^2}. \tag{4.3}$$

It is clear from this equation that $\mathcal{A} \propto \gamma^2$. In our experiment the relation $\mathcal{A} \propto \gamma^2$ is verified, as shown in Fig. 4.4(a). This fairly robust relation has also been found in non-affine correlation functions of, for example, flexible polymer networks [97] and semiflexible polymer networks at small strains, using simulations [56] and experiments [90].

The quantity $\frac{\mathcal{A}}{\gamma^2}$, which is independent of strain γ, provides a good measure of the degree of non-affinity of the sample. We shall refer to this quantity, $\frac{\mathcal{A}}{\gamma^2}$, as the strain-normalized non-affine parameter. $\frac{\mathcal{A}}{\gamma^2}$ is calculated for each sample as follows: For a particular strain, $\mathcal{A}$ is calculated by averaging the square of the non-affine displacements, $\vec{u}_i^2$, for all tracer beads in the sample; typically, we carried out multiple shear measurements at the same strain (see Section 4.3.3), and the displacement data from all particles in all repeated shear measurements were averaged together to derive the mean $\mathcal{A}$ and its standard deviation. The resultant $\frac{\mathcal{A}}{\gamma^2}$ data were then fit to a linear function. The slope of the linear fit gives $\frac{\mathcal{A}}{\gamma^2}$ for the sample; the intercept from the fitting is comparable to the noise floor of the measurements in $\mathcal{A}$. Standard deviations for the slopes were also derived. We use this parameter, $\mathcal{A}$ versus γ, which represents an intrinsic material property, for comparisons among samples prepared at different times or under different conditions.

The $\frac{\mathcal{A}}{\gamma^2}$ value calculated for each sample, along with its constituent acrylamide and bis concentration is listed in Table 8.1. Fig. 4.4(b) plots the mean and standard error of the strain-normalized non-affinity parameter, $\frac{\mathcal{A}}{\gamma^2}$ for PA gel samples at various monomer (*viz.,* 7.5% and 15% acrylamide, w/v), and cross-link (between 0.005% and 0.12% bisacrylamide, w/v) concentrations. The large error bars in the $\frac{\mathcal{A}}{\gamma^2}$ values for the 7.5% acrylamide samples at different bis concentration (standard deviation $\sim 38\%$) arises primarily from sample-to-sample variations associated with gels polymerized under (ostensibly) identical experimental conditions. The error bars for the 15% acrylamide samples are much smaller than the 7.5% samples, because data in the former case were extracted from a single sample polymerized at the given acrylamide and bis concentration. Within this relatively large range of values, the strain-normalized non-affinity measure does not appear to vary significantly as a function of either the density of polymer chains or the network mesh-size, and it is evenly distributed around the mean $\frac{\mathcal{A}}{\gamma^2}$ calculated over the entire range of PA gels sampled in our experiments. This mean value is indicated by the dashed line in Fig. 4.4(b). The average values of $\frac{\mathcal{A}}{\gamma^2}$ obtained for different monomer concentrations along with their respective standard deviation and standard error of each group of measurements are summarized in Table 4.1. We also used an alternative approach for calculating the mean $\frac{\mathcal{A}}{\gamma^2}$ in the APPENDIX, Section A.1; this alternative approach treated all beads across all samples equally. The results obtained by this alternative method were essentially same as the results above. Perhaps not surprisingly, we will propose below that this measured non-affinity is largely dominated by inhomogeneities formed during synthesis of the PA gels, rather than being dictated by the thermal fluctuations of the polymer cross-links.

monomer conc.	$\frac{\mathcal{A}}{\gamma^2}$ $[\mu m^2]$	Std. Dev. $[\mu m^2]$	Std. Err. $[\mu m^2]$
7.5%	1.65	± 0.63	± 0.21
15%	1.70	± 0.51	± 0.25
all samples	1.67	± 0.57	± 0.16

Table 4.1: Summary of $\frac{\mathcal{A}}{\gamma^2}$ at different acrylamide concentrations.

4.3 Discussion

4.3.1 Effectiveness of Cross-links

The measured G' of polyacrylamide gels generally follows predictions of standard theories of rubber elasticity, i.e., $G' = 2\nu N k_B T$ where N is the number density of cross-links, k_B represents the Boltzmann constant, T represents temperature, and ν is the efficacy of cross-link [145]. Note the additional multiplicative factor of 2, which arises because bisacrylamide is a tetra-functional cross-link. $\nu = 1$ implies that all cross-links are effective, i.e., the polymer strands attached to each cross-link are a part of the homogeneous network. Any unproductive reaction of bisacrylamide or inhomogeneity in the network, for example if one of the four polymer strands connected to a cross-link is a dangling chain which does not contribute to the elasticity of the polymer network, leads to $\nu < 1$ [127, 145, 22]. Taking the molecular weight of a bisacrylamide as 154, the elasticity of a polyacrylamide gel at room temperature can be rewritten as $G' = 33.2 \times 10^4 \nu c$ measured in Pascals, where c is the percentage concentration of bisacrylamide. In Fig. 4.3(b), we see that G' is equal to $4.0 \times 10^4 c$ Pa for polyacrylamide gels with

7.5% acrylamide, and $3.0 \times 10^5 c$ Pa for 15% acrylamide respectively. Hence $\nu = 0.12$ for the 7.5% and $\nu = 0.9$ for the 15% PA gels. The higher value of ν for 15% acrylamide PA gels is due to the higher polymer chain density in this system, suggesting that there is a higher probability for a bis molecule to find an acrylamide polymer chain in its neighborhood that would result in an effective cross-link.

Note though, that this is a simplified scenario; ν does not keep increasing indefinitely with increasing polymer chain concentration, but levels off as the semi-dilute limit for acrylamide chains is reached. The elastic modulus is also strongly affected by the amount of bis present, an excess of which may change the polymer solubility from good to theta solvent and the effective persistence length of the acrylamide chains [48], and may even lead to macroscopic syneresis (expulsion of the solvent and contraction of the gel) for sufficiently large concentrations of bis [95]. Thus, the relative concentrations of acrylamide and bis may have profound effect on the bulk modulus of PA gels, where instead of a linear scaling of the elastic modulus with the bis concentration, as seen in our samples (Fig. 4.3(b)), the elastic modulus will level off [162] due to micro-phase separation in the gels. The roles of bis and acrylamide are not limited to macroscopic elastic modulus only, but also have significant impact on the microscopic non-affinity of PA gels, as we note in the following section.

4.3.2 Elastic Inhomogeneities in Polyacrylamide Gels

The value of $\frac{A}{\gamma^2}$ characterizes the inhomogeneities in the elasticity of the material. In this section we analyze two possible scenarios that give rise to randomness in elastic modulus K (i.e., randomness in the shear modulus G' of PA gels), and thus generate non-affine responses in polyacrylamide gels. We then compare the predicted non-affinity in these two scenarios with experimental results.

In the first scenario, the gel is assumed to be nearly ideal. The inhomogeneity is assumed to be produced by the intrinsic randomness in the network geometry arising from thermal fluctuations frozen into the PA gel at the moment of gelation; in this case, the smallest lengthscale characterizing the inhomogeneity would be the mesh size of the network, and the inhomogeneities cannot be reduced by improving the synthesis process. In the second scenario, "nonthermal" inhomogeneities are assumed to be introduced during the sample preparation process. For example, this effect could arise if the cross-links are not homogeneously distributed; in this second case, elastic inhomogeneities could be present at lengthscales much larger than the network mesh size.

The elastic modulus correlation function Δ^K in the first scenario can be modeled as

$$\Delta^K(x) = (\delta G')^2 \xi_e^3 \, \delta(x), \tag{4.4}$$

where $(\delta G')^2$ is the variance of the local shear modulus G', and ξ_e is the characteristic mesh size of the network. In this scenario the gelation process is nearly ideal, and the only randomness comes from the frozen thermal fluctuations in the liquid at the moment of gelation. Thus the correlation of the elastic modulus is characterized by the only length scale in the system, the mesh size ξ_e, which we also take to be the short-distance cutoff of the system because the picture of continuous elasticity breaks down below this length scale. Thus the elastic modulus correlations at this scale is characterized by a Dirac delta-function in Eq. (4.3). The Fourier transform of Δ^K

is then

$$\Delta^K(q) = (\delta G')^2 \xi_e^3. \tag{4.5}$$

We plug this correlation function back to Eq. (4.5) to calculate $\mathcal{A}$. To evaluate the integral, one has to set a small length scale cutoff, which is ξ as we discussed. Below this length scale the polymer network structure cannot be coarse grained, and one cannot characterize the properties using continuous elasticity.

We obtain the non-affine parameter $\mathcal{A}$ from the integral (ignoring unimportant $O(1)$ constant prefactor):

$$\mathcal{A} \sim \left(\frac{\delta G'}{G'}\right)^2 \gamma^2 \xi_e^2. \tag{4.6}$$

The experimentally measured $\mathcal{A}$ is plotted as a function of γ^2 at two different monomer and cross-link concentrations in Fig. 4.4(a). Both results are consistent with the theoretical prediction that $\mathcal{A}$ is proportional to γ^2. However, the magnitude of $\frac{\mathcal{A}}{\gamma^2}$ is of the order of $1\mu m^2$. Since the mesh size is expected to be of order 10 nm, we obtain $\delta G'/G' \sim O(10^2)$ from Eq. (4.6) and our measurements of $\frac{\mathcal{A}}{\gamma^2}$. This value is too large for a nearly ideal "thermal" gel. In a nearly ideal gel, the inhomogeneities in network geometry and thus the elasticity come purely from thermal fluctuations at the moment of gelation, thus both $\delta G'$ and G' are of order $k_B T$ times the cross-link number density, so one should expect $\delta G'/G' \sim O(1)$. Furthermore, in this scenario $\mathcal{A}$ should be related to the concentration of cross-links c as $\mathcal{A} \propto \xi_e^2 \propto c^{-2/3}$ (because $\xi_e \propto c^{-1/3}$), but this behavior is not seen in Fig. 4.4(b), in which $\frac{\mathcal{A}}{\gamma^2}$ is essentially a constant (albeit with a wide scatter).

Other length scales in the gel will not significantly affect this analysis. The persistence length of the polymer chain is even smaller than the mesh size, the small length cutoff of the analysis, and thus will not affect the result. The size of the tracer bead, although on the scale of $1\mu m$ and relevant to the problem, only weakly changes the value of $\mathcal{A}$, as we discuss in Section 4.3.4 and Section 2 of the supporting material available online [8].

The discrepancy between the value of $\delta G'/G'$ suggested by the experiment and the theoretical value of nearly ideal "thermal" gel suggest that our second scenario may be more realistic for these systems. In the second scenario, "nonthermal" inhomogeneities in the distribution of the bisacrylamide (cross-link) during the process of polymerization are assumed to exist. These inhomogeneities are frozen in at polymerization and their contribution to the inhomogeneous elasticity in the resulting PA gel dominates over the contributions of thermal fluctuations at gelation described in the first scenario, because these "nonthermal" inhomogeneities exhibit greater variance and longer correlation length, as we discuss below. These types of heterogeneities have been recognized previously in the literature [48, 95, 19, 7, 123, 53, 54, 92, 152, 153, 119, 87, 6, 109, 73]. Briefly, because the hydrophobicity of polymerized bisacrylamide is higher than the polyacrylamide chains, the hydrophobic cross-links have a tendency to aggregate during the sample preparation (Note: Solubility of bis in water = 0.01-0.1 gm per 100 ml at 18^{o}C. Solubility of acrylamide in water = 216 gm per 100 ml. [95]). This effect can generate an inhomogeneous spatial distribution of cross-links at length scales longer than the mesh size.

Thus, in the second scenario, regions with high shear modulus and regions with low shear modulus form in the polyacrylamide network as a result of the inhomogeneous distribution of cross-links frozen in during the process of sample preparation. We define the length scale ξ_G to characterize the size of this inhomogeneity. The resultant inhomogeneity in the shear modulus may then be characterized by a Gaussian correlation function,

$$\Delta^K(r) = (\delta G')^2 e^{-\frac{r^2}{2\xi_G}}. \tag{4.7}$$

We then plug this correlation function it back into Eq. (4.3). The integral is convergent due to the finite range of this correlation function, i.e., so the short length scale cutoff is not needed in this scenario. The resulting non-affine parameter is given by

$$\mathcal{A} \sim \left(\frac{\delta G'}{G'}\right)^2 \gamma^2 \xi_G^2. \tag{4.8}$$

For a careful derivation of this relation with the exact value of the prefactor, see Section 1 of the supporting information for Ref. [8] available online.

In fact, considerable effort has been expended over the years to characterize inhomogeneities inherent to PA gels. Starting with the pioneering work of Richards and Temple (1971) [123], various experimental techniques, *viz.*, gel-swelling and permeability studies [95, 152, 153], small angle x-ray [48, 95, 19] and neutron scattering [48, 7], quasi-elastic light scattering [48, 87, 73], dynamic light scattering [95, 109], UV-visible [119] and IR spectroscopy [92], NMR spectroscopy [54, 92], electron micrographs [53], have been used to quantify the nature and size of inhomogeneities created in PA gels. Some of these ideas have been considered in the context of gel elastic properties [6], as well as under varying acrylamide and bis concentration, and different polymerization reaction conditions. The ratio of monomer to cross-link concentrations, which determines the relative wettability of acrylamide and bis clusters during the polymerization process, as well as the reaction kinetics, all affect the formation of dense, heterogeneous clusters of highly cross-linked polymers interspersed with patches of sparsely cross-linked polymer chains. The size of these spatial inhomogeneities embedded in the more uniform gel matrix has been reported to vary widely from a few nanometers to as much as half a micron, with homogeneous regions of comparable length scale in between.

One may substitute the inhomogeneity correlation length, ξ_G with the size of the spatial inhomogeneities reported in the aforementioned references. From the literature we find that $5\ nm \lesssim \xi_G \lesssim 500\ nm$, which gives corresponding range of inhomogeneity magnitude of $3 \lesssim \frac{\delta G'}{G'} \lesssim 300$ for PA gels over a wide range of monomer and cross-link concentrations. For PA gels synthesized under similar preparation conditions as in our experiment, the length scale of inhomogeneities, $\xi_G \lesssim 200$ nm has been measured using a nano-indentation method. Briefly, an Atomic Force Microscope (DAFM, Veeco, Woodbury, NY) with a sharp conical tip is used to perform nano-indentation on a polyacrylamide gel made of 7.5% acrylamide and 0.1% bis. Working at the "force volume" mode, the AFM scans an area of $1\ \mu m \times 1\ \mu m$ area with a resolution of 16 pixels/μm. At each pixel, a force-indentation curve is obtained and fit to the Hertz model to get the local Young's modulus. Thus, a map of Young's moduli is obtained for a $1\ \mu m^2$ area with a spatial resolution of $62.5\ nm$. The Young's moduli within the map varies from $3800\ Pa$ to $6300\ Pa$ with a mean of $4800\ Pa$. The length scale of inhomogeneity is approximately $200 \pm 100\ nm$. Using $\xi_G \lesssim 200\ nm$ and $\frac{A}{\gamma^2} = 1.67 \pm\ 0.57\ \mu\text{m}^2$ (4.1) in Eq.4.6, we obtain $\frac{\delta G'}{G'} \lesssim 7$.

4.3.3 Repeated Shear Measurements

As part of this study, we explored the effects of cycled measurements on $\mathcal{A}$ in the same sample. By repeatedly shearing and unshearing a PA gel sample at the same strain, we determined the distribution of $\mathcal{A}$ for the same set of particles within a single sample. The resultant variation of $\mathcal{A}$ is not insignificant, though it is considerably less than sample-to-sample error.

To demonstrate this effect, a PA gel sample is synthesized at 7.5% acrylamide and 0.06% bis with $1\ \mu m$ tracer beads embedded in it. The gel is sheared repeatedly to a strain of 0.2, and $\mathcal{A}$ is measured each time as shown in Fig. 4.5(a). Error bars reflect the systematic error in our measurements. The tracer beads relax back roughly to their original (unsheared) positions once the strain is released. The variation in $\mathcal{A}$ suggests that some local rearrangement of the polymer network neighborhood occurs after/during each cycle, perhaps because of the presence of compliant chain entanglements or reorganization of the gel-bead interface. These rearrangements permit the tracer beads to explore and experience slightly different local environments every time the sample undergoes a shear transformation. Non-affinity was slightly different after each shear event. The measured standard deviation of $\frac{\mathcal{A}}{\gamma^2}$ $(\sim 8\%)$ for repetitive shear in the sample is much smaller, however, than that measured for different gels prepared under apparently identical experimental conditions.

With respect to non-affinity variation with repeated cycling, we have explored this phenomenon under different strains as well as for different polymer gel concentrations. It appears that the randomness persists even when a sample gel is sheared repeatedly thirty times. The variation in non-affinity parameter appears to be random, independent of the number of times the gel is sheared. Chain entanglements (see APPENDIX, Section A.2), dangling ends, etc., could

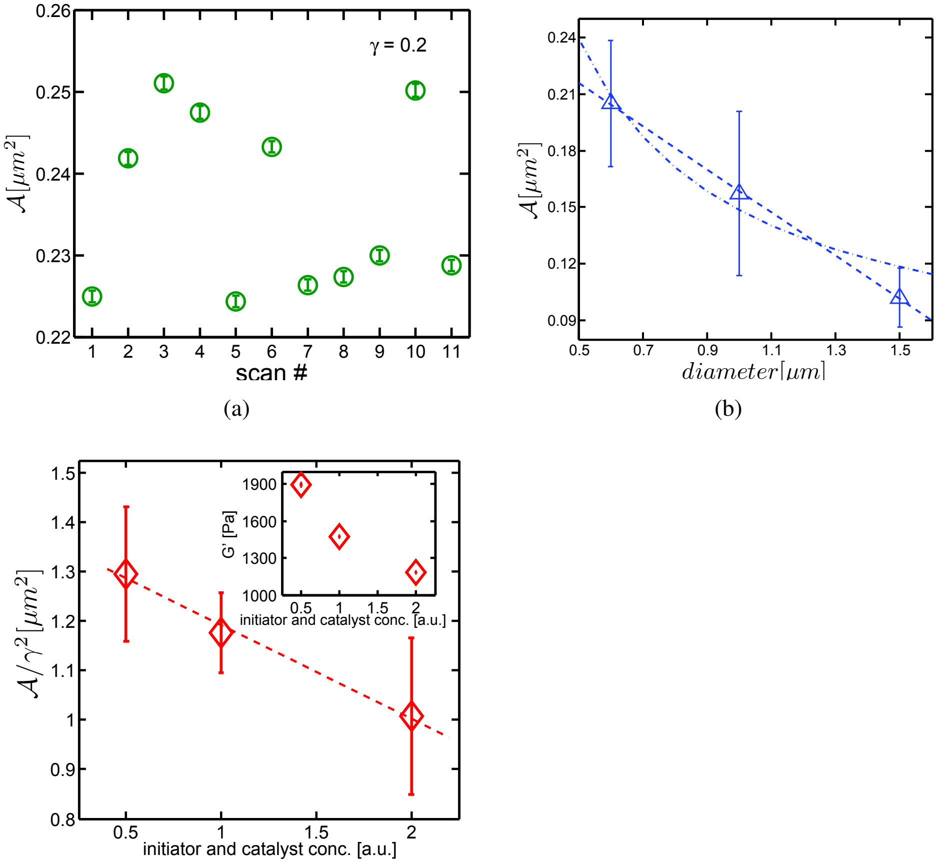

(a) (b)

(c)

Figure 4.5: (a) Non-affine parameter, $\mathcal{A}$ in a sample PA gel (7.5% acrylamide and 0.06% bis), sheared repeatedly under $\gamma = 0.2$ strain. (b) Average non-affine parameter in a sample PA gel measured using fluorescent tracer beads of average diameters of 600 nm, 1 μm and 1.5 μm. $\mathcal{A}$ decreases with increasing tracer-bead diameter. Measurements shown here were performed on a sample PA gel with 7.5% acrylamide and 0.06% bis, sheared ten times at a strain of $\gamma = 0.3$. (c) Elastic shear modulus decreases with increasing initiator and catalyst concentrations, for PA gel where the monomer and cross-link concentrations have been kept constant(inset). $\mathcal{A}$ decreases linearly with increasing initiator and catalyst concentrations. Data are shown here for a 7.5% acrylamide and 0.03% bis PA gel.

contribute to this randomness in the measured non-affinity [22], and one cannot rule out the possibility that the local environment of the tracer micro-beads is subtly distorted due to polymer depletion or adsorption, which might cause more/less slippage or sticking of the tracer beads to the surrounding gel matrix under shear [15]. We use this repeated shear technique to calculate the systematic error in our measurements to be $\sim 8\%$ an use this value as the lower bound for all error estimations shown in Fig. 4.4(b).

4.3.4 Tracer Bead-size Dependence

We also explored the effects of the size of the tracer beads on the magnitude of the non-affine parameter, $\mathcal{A}$, using tracer beads of three different sizes, *viz.*, 0.6, 1 and 1.5 μm. The different-sized beads are fluorescently labeled such that they are uniquely excited by three different wavelengths of the confocal scanning beam, *viz.*, 488, 568, and 640 nm respectively. We disperse these three different-sized beads in a sample PA gel and image them using three different wavelength excitation beams in succession during a particular shear event. We see that, for the range of bead-sizes used in our experiment, the magnitude of $\mathcal{A}$ remains within the range indicated in Table 4.1 for 7.5% acrylamide PA gels. We also note that there is a functional dependence on tracer bead-size of the average value of $\mathcal{A}$ measured from repeated shear events. Fig. 4.5(b) plots the average $\mathcal{A}$ from eleven repeated shear events at $\gamma = 0.3$, for a PA gel at 7.5% acrylamide and 0.06% bis. We see that the average $\mathcal{A}$ decreases with an increase in the diameter of tracer beads. $\mathcal{A}$ can be fit to a linear function of tracer bead size, with a slope of $\sim -0.11 \pm 0.001$ μm^2 and an intercept of $\sim 0.27 \pm 0.002$, as shown. When fit to an inverse function of tracer bead diameter, we obtain a pre-factor of 0.09 ± 0.025 μm^3 and an intercept of 0.06 ± 0.031 μm^2, also shown in the figure.

Essentially all of the theoretical analysis presented in this chapter thus far employed the simplifying assumption that we can treat the tracer beads as point objects that probe local non-affine deformations. However, the size of the tracer bead is comparable to the correlation length ξ_G of the random elastic modulus. In Section 2 of the supporting material available online [8], we have computed the corrections due to the finite size R of the bead in a simplified model of electrostatics in random media, which is a scalar analog to the elastic problem. In the limit of $R \to 0$ the non-affine parameter $\mathcal{A}$ smoothly approaches the limit of point probe, while in the limit of $R/\xi \gg 1$, $\mathcal{A}$ approaches a different value which is simply related to the $R \to 0$ value by a constant factor of $O(1)$. This simple calculation is consistent with the experimental observation (Fig. 4.5(b)) that $\mathcal{A}$ is not very strongly affected by the bead-size, R. However the exact dependence observed experimentally is not captured by the calculation.

4.3.5 Effects of Initiator and Catalyst Concentration

Finally, we explored the effects of reaction kinetics on the strain-normalized non-affinity measure, $\frac{\mathcal{A}}{\gamma^2}$. To do that, we prepare PA gels with same amount of monomer and cross-link concentration, viz., 7.5% acrylamide and 0.03% bis, but with the initiator and catalyst (TEMED and APS, respectively) concentrations twice and half of the normal amount used. The gel reactions proceed faster (slower) as a result, respectively, yielding lower (higher) plateau shear modulus for twice (half) the normal initiator and catalyst concentrations (inset in Fig. 4.5(c)). The $\frac{\mathcal{A}}{\gamma^2}$ values calculated for these samples are still within range of $1.65 \ \pm 0.63 \ \mu m^2$, the measured average for 7.5% acrylamide PA gels, leading us to believe that measured values of $\frac{\mathcal{A}}{\gamma^2}$ are still dominated by the inhomogeneities in these gels. Error bars reflect the standard deviation in the ensemble-averaged non-affinity values measured for four scans over each sample volume. Within this prescribed range, though, there is a slight inverse dependence of $\frac{\mathcal{A}}{\gamma^2}$ on the concentration of TEMED and APS (Fig. 4.5(c)) which we do not understand.

4.4 Conclusions

Non-affine deformations under shear are measured in a simple cross-linked gel and are employed to provide insight about inhomogeneities in the flexible polymer gels. Results indicate that, for a wide range of applied strain, γ, the shear modulus remains independent of strain and the non-affine parameter, $\mathcal{A}$, which is the mean square non-affine deviation in the PA gels, is proportional to the square of the strain applied. These results agree with small-strain predictions in Ref. [23] based on linear elasticity and support the conjecture that $\mathcal{A}$ scales as γ^2 as long as the shear modulus remains independent of γ. Interestingly, the magnitude of $\mathcal{A}$ is greater than what one would expect from theoretical calculations assuming that the PA gels are nearly-ideal and the only source of disorder is from the frozen-in thermal fluctuations at gelation. Also, the degree of non-affinity appears to be independent of polymer chain density and cross-link concentration. Thus, we posit that there are additional built-in inhomogeneities in the PA gels that lead to the large non-affinity we observe. Indeed, there is ample evidence in existing literature of the presence of such inhomogeneities in PA gels due to a difference in the hydrophobicities of the bisacrylamide and acrylamide monomers. Combining the inhomogeneity length-scale estimated from Atomic Force Microscopy measurements, i.e, $\xi_G \sim 200$ nm, with the non-affinity measurements, we calculate the magnitude of local variations in elastic modulus, $\frac{\delta G'}{G'}$ to be ~ 7. Our measurements of non-affinity in PA gels, which are model flexible polymer gels, provide a benchmark for the degree of non-affinity in soft materials, and will serve as an interesting comparison to non-affinity in more complicated materials such as semi-flexible bio-polymer gels.

Chapter 5

Non-Affinity in Gels of Different Polymer Classes

This chapter investigates the mechanical response in different polymer gels, especially those with different persistence length, l_p. Macroscopic shear elasticity and non-affine deformation is studied as a function of shear strain, using a microscope with piezo-driven objective coupled with a conventional rheometer (See Chapter 3). Gels investigated herein range from chemically crosslinked gels of flexible polymers, such as polyacrylamide, to biopolymer gels such as fibrin, collagen and actin, to physically crosslinked gels of stiff mesogens such as carbon nanotubes. Dimensionless nonaffinity parameters, $\mathcal{S}(\gamma)$ and $d\mathcal{S}(\gamma)$ are defined for this purpose, that permit easy comparison of non-affinity across the different classes of polymer gels. Measurements indicate that non-affine displacements in polymer gels increase with increasing l_p or increasing polymer stiffness.

5.1 Experimental Procedure

5.1.1 Sample Preparation

To track non-affine deformation under shear, fluorescent tracer beads are embedded in the gel samples. Polystyrene (PS) micro-spheres with a mean diameter of 1 μm, carboxyl-modified and fluorescently labeled (excitation wavelength of 580 nm, emission wavelength of 605 nm) were purchased from Molecular Probes, Invitrogen Corp., USA, for this purpose. The tracer beads are uniformly dispersed in each gel precursor uniformly *before* the gelation reactions are initiated. The concentration of tracer beads is adjusted empirically to produce a sufficient bead density to enable tracking of multiple beads in the observation volume without the overlapping of fluorescence intensities from adjacent beads. All polymerization reactions are carried out *in situ* at room temperature ($\sim$25 ^{o}C), at an oscillatory frequency of 0.1 Hz, and at a shear strain with peak amplitude $\gamma = 0.01$. Unless otherwise noted, all samples undergoing gelation are sealed off with a low-viscosity ($\sim$40 mPa.s) silicone oil (Fluka, Germany) in order to prevent the solvent from evaporating out of the gels. The gels investigated in this chapter are prepared as follows:

To track non-affine deformation in polymer gels under shear, fluorescent tracer beads are embedded in the gel samples. Polystyrene (PS) micro-spheres with a mean diameter of 1 μm, carboxyl-modified and fluorescently labeled (excitation wavelength of 580 nm, emission wavelength of 605 nm) were purchased from Molecular Probes, Invitrogen Corp., USA, for this purpose. The tracer beads are uniformly dispersed in each gel precursors uniformly *before* the gelation reactions are initiated. The concentration of tracer beads is adjusted empirically to produce a sufficient bead density to allow tracking of multiple beads in the observation volume without

the overlapping of fluorescence intensities from the adjacent beads. All polymerization reaction are carried out at room temperature (∼25 ^{o}C), at an oscillatory frequency of 0.1 Hz, and shear strain with a peak amplitude of $\gamma = 0.01$. Unless otherwise mentioned, all samples undergoing gelation are sealed off with a low-viscosity (∼40 mPa.s) silicone oil (Fluka, Germany) to prevent the solvent from evaporating out of the gels. The different gels investigated in this chapter are prepared as follows:

Salmon Fibrin Gel: Lyophilized fibrinogen [150] and thrombin [101] prepared from salmon blood plasma are provided by Sea-Run Holdings, Inc. (South Freeport, ME). Fibrinogen is rehydrated and dialyzed against 50 mM Tris, 150 mM NaCl, pH 7.4 at a concentration of 20 mg/ml; it is diluted in the same buffer to the target concentration. Thrombin is rehydrated in 50 mM Tris, 1 M NaCl (pH 7.4) at a concentration of 1500 NIH U/ml (NIH unit or 'NIH U' indicates the current US standard used for the measurement of human α-thrombin, originally developed by the National Institutes of Health (NIH) in Bethesda, MD.). Fibrin gel is prepared by addition of 1.8 NIH U/ml thrombin to 2.5 mg/ml fibrinogen and polymerized *in situ* between the rheometer plates. PS micro-spheres were dispersed in the thrombin solution uniformly before the fibrinogen is added to it.

Human Fibrin Gel: Lyophilized fibrinogen and thrombin from human blood plasma were prepared in the same way as salmon fibrin. The stock solutions were diluted in pH 7.4 Tris buffer containing PS tracer beads to yield fibrin gels with final concentrations of 2.5 mg/ml fibrinogen and 1 NIH U/ml thrombin.

Collagen Gel: Type I rat-tail collagen (BD Bioscience, USA) in 1x PBS buffer is polymerized at 1.5 mg/ml polymer concentration. PS beads, same as the as the ones used before, are uniformly mixed into collagen samples and polymerized *in situ* between the rheometer plates.

Actin Gel: Globular monomers of actin, or G-actin, were extracted from rabbit muscles [118]. Filamentous actin or F-actin gels at 4.5 mg/ml are composed of G-actin (85 μl at 9.5 mg/ml initial concentration), and biotinylated actin (15 μl at 9.24 mg/ml initial concentration) are mixed thoroughly in G buffer (80 μl) and actin polymerization buffer (20 μl) in the ratio, 17:3. The sample is incubated for 12 minutes at room temperature. Avidin (2.7 μl at 5 mg/ml) is added to the solution, mixed well, and loaded on the rheometer where the gelation reaction continues. Twenty minutes into the polymerization reaction, the sample is hydrolyzed with F-buffer. After another 15 min, the excess buffer is pipetted off and the sample is sealed using silicone oil to prevent solvent evaporation. Polymerization proceeds for $\approx$ 1.5 hr.

Carbon Nano-Tube Gel: Single walled carbon nanotubes (SWNT) at 0.4 wt% and sodium dodecylbenzenesulfonate (NaDDBS) surfactant (1:6 of SWNT:NaDDBS) is suspended in DI water. Over time, the nanotubes form a three-dimensional, isotropic percolating gel where the nanotube-nanotube overlaps are physically cross-linked through van der Waals attraction [52, 16]. Purified [59] HiPCO SWNT purchased from Carbon Nanotechnologies Inc., USA, were for this purpose. Once the gelation is complete (i.e., G' and G" values remain stable in time) in $\gtrsim 2$ hrs, 1 μm PS beads already dispersed in the SWNT gels are tracked under shear for non-affinity measurements. (Note, because these gels are not chemically crosslinked, we do not see any strain-stiffening in SWNT gels.)

Polyacrylamide Gel: Polyacrylamide (PA) gel is made by adding 0.02% bis-acrylamide (bis) cross-linker to 7.5% acrylamide in aqueous 50 mM HEPES buffer (pH $= 8.2$), in the presence of

0.5 wt % ammonium persulfate (APS) initiator and 0.1 wt % N, N, N', N'- tetramethylethylenediamine (TEMED) catalyst. PS beads are uniformly dispersed in the mixture before the addition of APS. Polyacrylamide gels are composed of flexible network filaments and exhibit linear elastic behavior.

Polyacrylamide and N-isopropylacrylamide Gel Mix: An inherently heterogeneous mixture of PA gel and large microgel spheres of N-isopropylacrylamide (NIPA), is mixed in the ratio 3:5, and tested for non-affinity. To make this sample, NIPA micro-particles, $\sim$15 μm in diameter, are mixed into an aqueous HEPES buffer with 4% acrylamide, 1% bisacrylamide in the above-mentioned ratio, along with PS tracer beads and TEMED, and vortexed. APS is added to this mixture that initiates the polymerization reaction. PA gel polymerizes around the NIPA micro-particles resulting in a translucent gel. As a result of the synthesis method employed here, PS tracer beads are present exclusively in PA gel part of the mixture.

The linear elastic gels are used as controls to compare both macroscopic elasticity and non-affinity measures from the various semi-flexible bio-polymer networks studied. Some gels exhibit non-linear elasticity [138].

5.1.2 Rheology

Rheological measurements of the gels are performed using a Bohlin Gemini rheometer (Malvern Instruments, UK) with cone (4^o, 20 mm) and plate geometry. All samples are polymerized between the rheometer plates; the gelation process is followed throughout with rheology measurements at low frequency ($\omega = 0.1$ Hz) and low oscillatory strain (peak amplitude of $\gamma = 0.01$). During this process, both G' and G'' increase steadily and reach steady-state values once the samples have fully polymerized. Amplitude sweep measurements are made at $\omega = 0.1$ Hz to measure the elastic response of the different polymer gels as function of shear strain, γ. Raw stress response data from an applied sinusoidal strain are analyzed using large amplitude oscillatory shear (LAOS) techniques to calculate G' as a function of γ.

5.1.3 Non-affinity Measurements

Microscopic deformations in polymer gels are measured under shear using the rheometer and optical microscope setup. Briefly, a Nikon TE 200 microscope is mounted below the rheometer, where the lower rheometer plate is replaced by a microscope glass slide mounted on a home-built microscope stage, as described in Chapter 2. An extensional rod, also described in Chapter 2 is employed to bring the upper plate of the rheometer down to the microscope stage and enable the rheometer to apply stress to the gels. A 60x extra long working distance objective was controlled by a E-662 piezoelectric actuator (Physik Instrumente, Germany) to move up and down and scan the focal plane through the sample thickness. This arrangement enables us to image beads at different depths in the sample. Positions of beads in the focal plane with shear on and off are recorded using a Hamamatsu CCD camera (C4742-95). Images are processed using Matlab (MathWorks, Inc., USA), which determines the beads' positions with subpixel resolution [21, 10], to quantify the displacements of beads with a resolution of 50 nm in the image plane.

5.2 Results and Discussion

5.2.1 Macroscopic Elasticity

The elastic modulus of each gel is measured as a function of applied strain, as shown in Fig. 5.1. The strain sweep curves for the gels with and without embedded beads are statistically indistinguishable, suggesting that the presence of tracer beads do not alter gel structure.

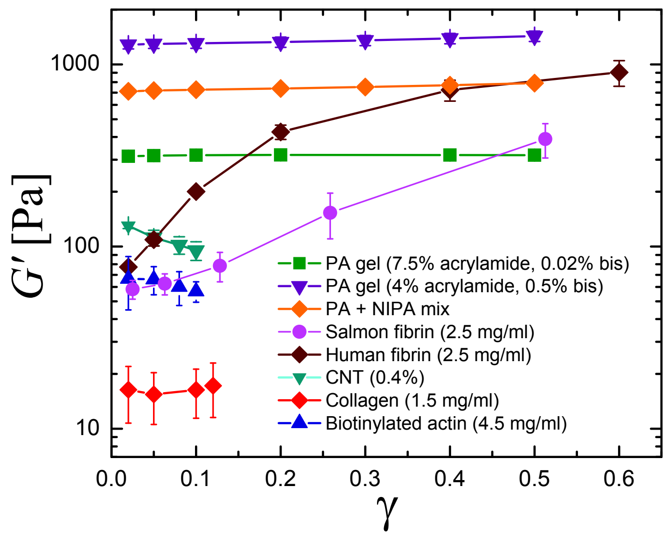

Figure 5.1: Elastic shear modulus, G', vs. strain, γ for different polymer gels.

The modulus of PA gels at different polymer and crosslink concentrations, as well as the one that is a mixture of PA and NIPA, remain constant as strain increases. This linear elastic behavior is as expected for flexible polymer gels of PA and NIPA. The persistence lengths of both PA and NIPA, as listed in Table 5.1, are of the order of Å. In contrast, semiflexible polymer gels composed of salmon and human fibrin, all crosslinked with thrombin, show significant strain-stiffening in Fig. 5.1. This behavior is also expected and was discussed in Chapter 2. The persistence lengths of all fibrin gels shown here are of intermediate length-scales of the order of a fraction of a μm (5.1).

Chemically crosslinked actin gels, as well as physically crosslinked gels composed of collagen and SWNTs do not exhibit strain-stiffening behavior. Though composed of stiff polymers, their elasticity decreases with increasing strain, which we ascribe to filament-bending or the network slipping/rearranging under shear (Chapter 2). We note that a sharp decrease in G' at much larger strains is observed (data not shown), possibly due to sample failure such as network disruption or detachment of the gel from the rheometer plates. Elastic moduli of the aforementioned gels, at several different polymer concentrations, are shown in APPENDIX B; these data also corroborate the observations we present in this chapter.

Table 5.1 lists the persistence lengths of polymer filaments comprising the gels studied in this chapter. These values have been reported previously as follows: PA [8], NIPA, [121], salmon fibrin [155], human fibrin [63, 138], collagen [135], F-actin [61, 117], and CNT [52]. Overall, we note that chemically crosslinked gels composed of flexible polymers like PA and NIPA gels (with l_p of the order of Å) exhibit high shear moduli and linear elasticity for a wide range of strains; in comparison, gels with stiffer polymers (e.g., salmon and human fibrin gels, $l_p \sim 0.5$ μm) have comparable shear moduli as well as significant strain-stiffening. Physically crosslinked gels of stiff polymers (e.g., collagen, actin and CNT gels, $l_p \sim 10$ μm) have much lower shear moduli; they also tend to weaken and yield under growing strains due to the absence of chemical crosslinks.

Filament	l_p
polyacrylamide	∼3 Å
NIPA	∼3.5 Å
salmon fibrin	∼0.5 μm
human fibrin	∼0.2 μm
collagen	∼10 μm
F-actin	∼16 μm
CNT	∼22 μm

Table 5.1: Persistence length, l_p, of different filaments comprising the gels discussed in this chapter.

5.2.2 Displacement of Tracer Beads in Gels

We are able to record the displacement of beads in a 60μm$\times$60μm area using the microscope. Within this small area, approximately 1 cm from the axis of rotation, the strain applied to the sample can be approximated as a unidirectional shear. Fig. 5.2(a) shows the displacement of tracer beads in a sample fibrin gel, where the direction of shear is taken to be along the x-axis. As the distance from the bottom surface up into the gel increases, i.e., the z distance, the displacement along x also increases in a linear manner. The non-affine deformation may, in reality, be characterized by displacements along x-, y- and z-axes. Displacement of the beads in the z-direction may be estimated by monitoring the size of the diffraction ring of the beads that are out of focus. Due to the large focal depth of the microscope objective ($\approx$500 nm), only z displacements larger than 500 nm can be detected. Within this limit, displacements in the z-direction have not been observed for the samples under investigation. Hence, for simplicity, we analyze the bead displacement only along the x-axis in order to quantify non-affine behavior in the gels. In the measurements reported in this chapter, we neglect the displacements in the z- and y-directions, both of which are perpendicular to the direction of shear. This approach might underestimate the non-affine measurements, but should not affect the dependence of non-affinity on strain.

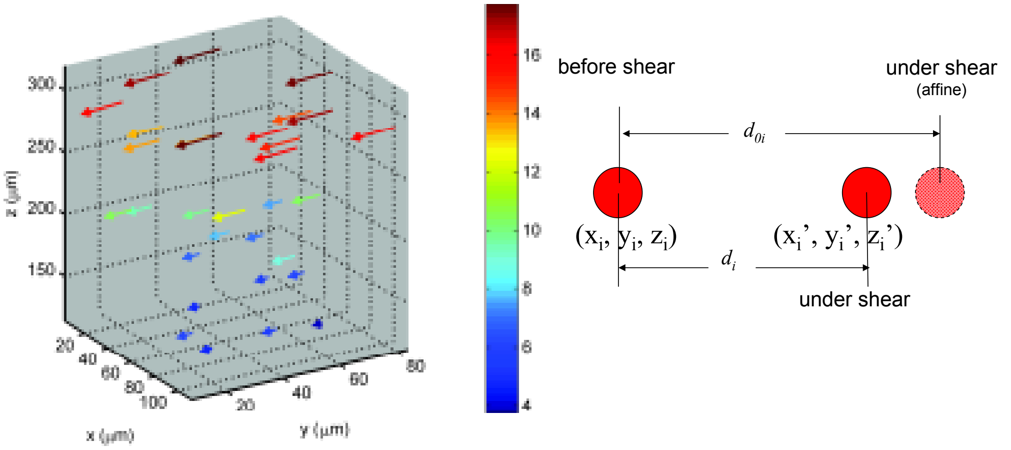

(a) (b)

Figure 5.2: (a) Measured displacement of tracer beads in a sample fibrin gel. Arrows represent the displacement vector for beads, with color indicating the magnitude of the displacement. (b) Schematic of a tracer bead position assuming *affine* response to shear deformation, and a *measured* response to shear deformation. d_{0i} and d_i denote the affine and measured displacements of the tracer bead, respectively.

5.2.3 Non-affine Parameter

Non-affinity in gels, $\mathcal{S}(\gamma)$, is quantified by the ensemble averaged deviation of bead displacements from the displacements for affine deformation:

$$\begin{aligned} \mathcal{S}(\gamma) &= \sqrt{\frac{1}{N}\sum_{i=1}^{N}\left(\frac{d_i - d_{i0}}{d_{i0}}\right)^2} \\ &= \sqrt{\frac{1}{N}\sum_{i=1}^{N}\left(\frac{d_i}{z_i\gamma} - 1\right)^2}, \end{aligned} \tag{5.1}$$

where d_i is the displacement for the i-th bead located at z_i when the sample is subjected to strain, γ. For an affine deformation, γ is uniformly distributed in the gel, i.e., every bead is subjected to the same γ in Eq. 5.1. d_{0i} is the affine displacement of the i-th bead. Under a simple shear strain along the x-direction, a bead located at (x_i, y_i, z_i) in the unstrained gel will displace to a new location (x_i', y_i', z_i') as

$$\begin{pmatrix} x_i' \\ y_i' \\ z_i' \end{pmatrix} = \begin{pmatrix} 1 & 0 & \gamma_i \\ 0 & 1 & 0 \\ 0 & 0 & 1 \end{pmatrix} \begin{pmatrix} x_i \\ y_i \\ z_i \end{pmatrix}, \tag{5.2}$$

where γ_i is the strain for this bead. The displacement of the bead induced by the strain is then $d_i = x_i' - x_i = \gamma_i z_i$. $\mathcal{S}$ is 0 for an affine deformation, since $\gamma_i = \gamma$. For non-affine deformation, the strain is not uniform across the sample, i.e., γ_i is not necessarily equal to γ. $\mathcal{S}(\gamma)$ therefore should be non-zero and should increase with larger non-affinity. Note that $\mathcal{S}(\gamma)$ is a quantity (without units) that is qualitatively similar to $\frac{\mathcal{A}}{\gamma^2}$ employed in Chapter 4.

The non-affinity parameter $\mathcal{S}$ is plotted as a function of γ for different gels in Fig. 5.3(a). Starting from $\gamma = 0.02$, $\mathcal{S}$ decreases continuously for all gels, indicating that the networks becomes more and more affine as strain increases. All PA gel samples, as well as the PA and NIPA gel mixture, have comparatively low values of non-affinity ($\mathcal{S} \approx 0.03$). In addition, these flexible polymer gels ($l_p \sim$Å) exhibit little dependence of $\mathcal{S}$ on applied strain. Fibrin gels with intermediate persistence lengths ($l_p \sim 0.5$ μm) have comparatively higher values of $\mathcal{S}$ (≈ 0.13 on average) and exhibit decreasing $\mathcal{S}$ with increasing γ, suggesting that the network becomes more affine at greater strains. Considering Figs. 5.1 and 5.3(a) together, we note that $\mathcal{S}$ becomes smaller at same strain values where the gels start exhibiting strain-stiffening behavior. This behavior is in accordance to the affine entropic model [138, 47, 45] discussed in Chapter 2. For gels composed of yet stiffer filaments such as collagen, F-actin and CNT (l_p of order tens of μm), the $\mathcal{S}$ are even higher (≈ 0.3), again decreasing with increasing strain (Chapter 2). Overall, we note a strong dependence of $\mathcal{S}$ on l_p; stiffer constituent polymer filaments exhibit greater non-affinity.

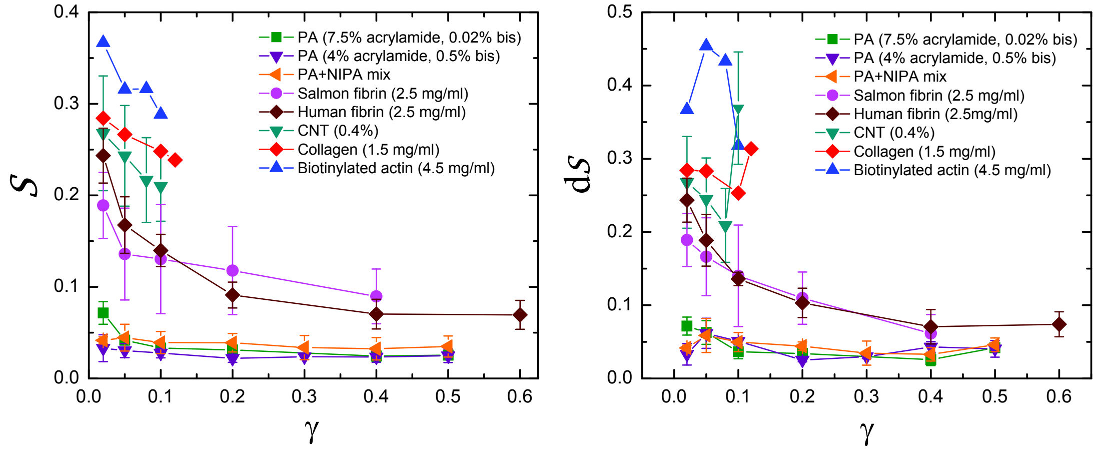

(a)

(b)

Figure 5.3: (a) $\mathcal{S}$ vs. γ calculated from different polymer gels (same samples as shown in Fig. 5.1). (b) $d\mathcal{S}$ vs. γ for the same polymer gels samples as shown in Figs. 5.1, 5.3(a).

A different but related non-affinity parameter, d$\mathcal{S}(\gamma)$ can be calculated for a differential strain, $\Delta\gamma$ applied on a sample under an existing pre-strain, γ (Chapter 2):

$$d\mathcal{S}(\gamma) = \sqrt{\frac{1}{N}\sum_{i=1}^{N}\left(\frac{\left(d_i(\gamma+\Delta\gamma) - d_i(\gamma) - z_i\gamma\right)^2}{(z_i\Delta\gamma)^2}\right)}, \tag{5.3}$$

Fig. 5.3(b) shows d$\mathcal{S}(\gamma)$ values of the same polymer gels as function of γ. The trends seen here are similar to those seen for $\mathcal{S}$ in that d$\mathcal{S}(\gamma)$ increases with increasing persistence length, l_p, and in semiflexible and stiff polymer gels, d$\mathcal{S}(\gamma)$ decreases with increasing pre-strain, γ.

Computer simulations of semi-flexible filaments in two dimensions (2D) [115, 23, 47, 45] provide models in which non-affine deformations are observed at small strains, and the deformation becomes increasingly affine with increasing strain. Simulation results suggest that the low stiffness of cross-linked semiflexible polymer networks under small strain originates from bending of the semiflexible filaments. At high strains, the stretching response of individual filaments contributes more to the network stiffness. Rearrangements of the network that govern the transition from a bending-dominated response at small strains to a stretching-dominated response at high strains cause the non-affine deformation of gels. Once the stretching sets in, the network becomes more and more affine. Note also that the magnitudes of $\mathcal{S}$ for semiflexible polymer gels shown in Figs. 5.3(a) and (b) are small compared to values derived for disperse networks of rigid filaments.

5.3 Conclusions

Overall, we observe that non-affine measures (both $\mathcal{S}$ and d$\mathcal{S}$) in polymer gels increase with increasing stiffness of the constituent polymers. PA and NIPA gels composed of flexible polymers have high shear moduli and low non-affine measures, both of which remain relatively constant with increasing strain. For semi-flexible human and salmon fibrin gels, we note a strong dependence of both shear moduli and non-affinity measures on applied strain: $\mathcal{S}$ and d$\mathcal{S}$ steadily decrease and the gels stiffen under increasing strain. Gels composed of yet stiffer polymers like actin, collagen and CNT have relatively lower shear moduli and high $\mathcal{S}$ and d$\mathcal{S}$ values. In general, the non-affine deformations for both semi-flexible and stiff polymer gels are significantly different from zero, though less than 0.5 at small strains, and decrease even further as strains increase. Relatively high non-affinity values at low strains could indicate that applied external stresses induce structural reorganization of the network, resulting in non-linear elasticity [115]. In contrast, the low $\mathcal{S}$ value at moderate strain suggests that the assumption of affine deformation is approximately applicable for the strains where strain-stiffening is observed, and supports the use of entropic theories to account for this phenomenon.

Fibrin networks formed under physiological conditions show properties of strain-stiffening in accordance with those reported [138, 82] for more uniform gels formed exclusively by fibrin protofilaments under non-physiological conditions. In a biological context, these results imply that fibrin extracellular matrices which form the first scaffold during wound healing, have isotropic response to external deformation on the scale of microns, as measured in this study, even though the network strands have persistence lengths also near a micron. A typical cell, like a fibroblast that would be imbedded in a fibrin gel, should be subjected to forces consistent with the macroscopic stress on the tissue. Highly non-affine stress fields within a matrix are more likely to arise in networks with stiffer filaments such as collagen gels [13], or non-isotropic distributions of actin filaments, in order to generate spatially ordered stresses that can dictate cell responses at the micron scale.

Chapter 6

Shear Deformations in Semi-flexible Polymer Networks

In the previous chapter, we measured non-affine deformations in gels composed of different types of polymers with a wide variety of persistence lengths to study the effect of polymer chain stiffness on non-affinity under shear. In this chapter, we concentrate on two types of semi-flexible polymer gels in particular, *viz.*, fibrin and collagen. We systematically vary polymer concentration and filament diameter in fibrin and collagen gels to investigate the effects of gel morphology on macroscopic shear elasticity and microscopic non-affine measures. Both measurements are accomplished using the confocal rheoscope setup described in Chapter 3. Confocal microscopy allows non-affinity measurements with much higher spatial resolution than was possible in the previous chapter. The macro-rheological behavior of the polymer gels is also tested extensively in the process, with an aim to understanding the underlying mechanism by which the polymer networks deform.

To these ends, collagen gels, with and without glutaraldehyde (GLA) crosslinks, and fibrin gels are studied. Shear moduli of GLA-crosslinked collagen gels are reported for the first time as functions of applied strain and polymer concentration. Elasticity in fibrin and glutaraldehyde-cross-linked collagen gels are seen to behave in accordance with the entropic model of non-linear elasticity [138]. Also, first normal stress difference, $N1$, is measured as a function of polymer concentration in semi-flexible polymer gels for the first time. Non-affinity within the aforementioned gels is quantified as a function of applied strain, polymer density, filament thickness, and tracer-bead size. We note that non-affinity measures *increase* with increasing l_p of the polymers, consistent with the findings in the previous chapter. These measures are also seen to *decrease* with increasing polymer concentration and increasing shear strain. Non-affinity values from semiflexible polymer gels are compared with those from flexible polyacrylamide (PA) gels. These observations are in qualitative agreement with current understanding of non-affinity in semi-flexible polymer networks.

6.1 Experimental Procedure

6.1.1 Sample Preparation

Fibrin gels are prepared in tris buffer at pH 7.4, using reconstituted fibrinogen (thrombin) at concentrations of 2.5 mg/ml (1.8 NIH U/ml), 3.75 mg/ml (2.8 NIH U/ml) and 5 mg/ml (3.75 NIH U/ml). Both fibrinogen and thrombin are extracted from salmon blood plasma. The ratio of fibrinogen to thrombin is kept fixed in order that the fiber diameter remains constant and only the network mesh-size changes. To study the effect of fiber diameter on network properties and non-affinity measures, divalent cations, in the form of 10 mM calcium chloride ($CaCl_2$) are added to

5 mg/ml fibrinogen gels during polymerization. Time taken for the elastic and viscous storage moduli to reach steady-state values is between 45 minutes and 60 minutes.

Collagen gels at various polymer concentrations are prepared, without and with 0.5 %(v/v) glutaraldehyde (GLA) crosslinks, using type I rat-tail collagen (BD Biosciences, USA) in $1\times$ phosphate buffered saline (PBS) solution. GLA-crosslinked collagen gels are prepared at 1 mg/ml, 2 mg/ml and 3 mg/ml. Uncrosslinked collagen gels are prepared at 2 mg/ml, 4 mg/ml, and 6 mg/ml polymer concentrations. Depending on the type of gel formed, polymerization lasts between 1 hour (for collagen gel with glutaraldehyde cross-links) and 2.5 hours (for uncrosslinked collagen gel).

Fluorescent polystyrene (PS) tracer beads at a concentration of 0.004 % weight/volume (w/v) are thoroughly mixed in (by pipetting) with the respective gel ingredients before the gelation reactions are initialized. This procedure helps to distribute the beads uniformly throughout the polymer network. Internally labeled and carboxylate-modified fluorescent polystyrene microspheres, 1 μm in diameter (Molecular Probes, California, USA) are used for the bulk of the non-affine experiments. In addition, other polystyrene particles with diameters 0.6 μm (also from Molecular Probes, California, USA), and 1.5 μm (Bangs laboratories Inc., Indiana, USA) are used to check the effect of tracer bead-size on non-affinity measured.

6.1.2 Rheology

A stress-controlled Bohlin Gemini rheometer with a cone-and-plate geometry (4° conic angle, 20 mm diameter) is used for the rheology measurements. Samples are prepared *in situ* so that good contact is established between the sample surfaces and the rheometer plates. The shear storage modulus (G') and loss modulus (G'') for each sample are monitored during polymerization using low strain amplitude (γ_0= 0.01) and low frequency ($f = 0.1$ Hz) oscillatory shear measurements. The polymerization reaction proceeds for $\sim 1 - 3$ hours, depending of the type of gel, with the elastic and viscous moduli attaining steady-state values in times ranging from $\sim$45 minutes to $\sim$2.5 hours. Care is taken to prevent solvent evaporation by sealing off the sample from the sides with a low density, low viscosity ($\sim$ 50mPa·s) silicone oil.

The shear storage modulus, G' for the semi-flexible gels, as a function of the strain applied is extracted from the raw stress and strain data using Large Amplitude Oscillatory Shear (LAOS) analyses [31]. The measurements confirm that the gels behave in accordance with the existing theories of semi-flexible polymer networks [138]. A set of control experiments are performed on the gels, with and without the tracer beads, to confirm that macroscopic properties of the gels are not altered by the presence of tracer beads.

6.1.3 Measures of non-affinity

The displacement of the fluorescently labeled tracer beads in the polymer gels are tracked using the confocal rheoscope discussed in Chapter 3 by following the procedure described in Sec. 3.1.1. The one-point non-affine parameter, $\mathcal{A}$ (see Eq. 3.1) is used:

$$\mathcal{A} = \frac{1}{N}\sum_{i=1}^{N}[(x_i - x_{0i} - \gamma_x z_{0i})^2 + (y_i - y_{0i} - \gamma_y z_{0i})^2 + (z_i - z_{0i} - \gamma_z z_{0i})^2],$$

for $i = 1, \ldots, N$ tracer beads. For a perfect shear deformation, the affine displacement $\vec{d_{ai}}$ of the i-th tracer bead would be purely in the direction of shear, i.e., along the x-axis (y and z components are zero). The resultant strains along all three component axes are estimated by fitting the x, y and z components of d_i to linear functions of z_{0i}, as seen from a 2mg/ml collagen gel sample (0.5% w/v glutaraldehyde) in Fig. 6.3(a). The real strain on the sample is calculated as $\gamma = \sqrt{\gamma_x^2 + \gamma_y^2 + \gamma_z^2}$. The x, y and z components of the affine displacement vector, $\vec{d}_{ai}$ are then calculated as $z_{0i}\gamma_x$, $z_{0i}\gamma_y$, and $z_{0i}\gamma_z$. Again, the y and z components, both perpendicular to the direction of shear, do not vary as a function of z_i, resulting in γ_y and $\gamma_z \approx 0$. Fig. 6.3(b) plots the distribution of non-affine deviations, $\vec{u}_x$, $\vec{u}_y$, and $\vec{u}_z$ for the same sample gel along the x, y, z axes respectively. The strain-normalized non-affine parameter, $\frac{\mathcal{A}}{\gamma^2}$ is defined as (Chapter 4):

$$\frac{\mathcal{A}}{\gamma^2} = \frac{\langle \vec{u}_i^2 \rangle_{i=1,2,\ldots,N}}{\gamma^2}, \tag{6.1}$$

where $\langle\rangle$ denotes the ensemble average of all N tracer beads in the sample.

The two-point non-affinity correlation function, $\mathcal{G}_{ij}(r-r')$ between two tracer-beads located at $r = (x, y, z)$ and $r' = (x', y', z')$ [23, 8] is also measured, i.e.,

$$\mathcal{G}_{ij}(r-r') = \left\langle \vec{u}_i(r) \cdot \vec{u}_j(r') \right\rangle = \left\langle [\vec{u}_x \cdot \vec{u}_{x'} + \vec{u}_y \cdot \vec{u}_{y'} + \vec{u}_z \cdot \vec{u}_{z'}] \right\rangle. \tag{6.2}$$

6.1.4 Scanning Electron Microscopy

Fibrin and collagen samples are prepared on glass substrates as described in Sec. 6.1.1. After the samples are polymerized, they are fixed with 2% (v/v) EM grade glutaraldehyde (Electron Microscopy Sciences, USA) for 90 minutes. The samples are then washed six times with deionized water to remove excess glutaraldehyde and salts that are present in the buffers. The water trapped in the gels is then replaced by ethanol by washing the samples six times each in 200 proof ethanol. The samples are then critical-point dried with CO_2 using a Samdri-PVT-3D supercritical dryer (Tousimis, USA), and sputter-coated with a gold-palladium layer a few nanometers thick using a Cressington Sputter Coater 108 (Cressington Scientific Instruments Ltd., UK). Images are obtained using a Quanta 600 scanning electron microscope (FEI, USA).

6.2 Results and Discussion

6.2.1 Bulk Rheology Measurements

Semi-flexible polymer gels of collagen and fibrin are visco-elastic in nature with interesting and unusual macroscopic mechanical properties. Two of these unique properties include non-linear elasticity in the form of strain-stiffening, and negative normal stress under shear.

6.2.1.1 Non-linear Elasticity

Bulk rheology measurements on fibrin gels are performed. Salmon fibrin gels with initial fibrinogen concentration, c = 2.5 mg/ml and 5 mg/ml are made using 1.8 and 3.6 NIH units/ml thrombin respectively, in pH 7.4 trizma buffer. To investigate the effect of filament thickness, a 5 mg/ml fibrin gel (and 3.6 NIH units/ml thrombin) is synthesized in the presence of 10 mM divalent calcium cations. Care is taken such that the gels are always well beyond the gelation threshold, i.e., the G' is always greater than G'' for proper optical tracking of entrapped tracer beads. G' and G'' are measured as functions of strain amplitude at an oscillatory frequency of 0.1 Hz, at room temperature. G' is calculated from raw shear stress and strain data using Large Amplitude Oscillatory Shear (LAOS) techniques [31, 66]. Specifically, the elastic and viscous shear moduli are calculated using Fourier Transform, and Lissajous analyses (for a detailed description of these techniques, see Section 2.1.2 in Chapter 2). We note that both these methods yield similar results for the range of γ explored in this chapter.

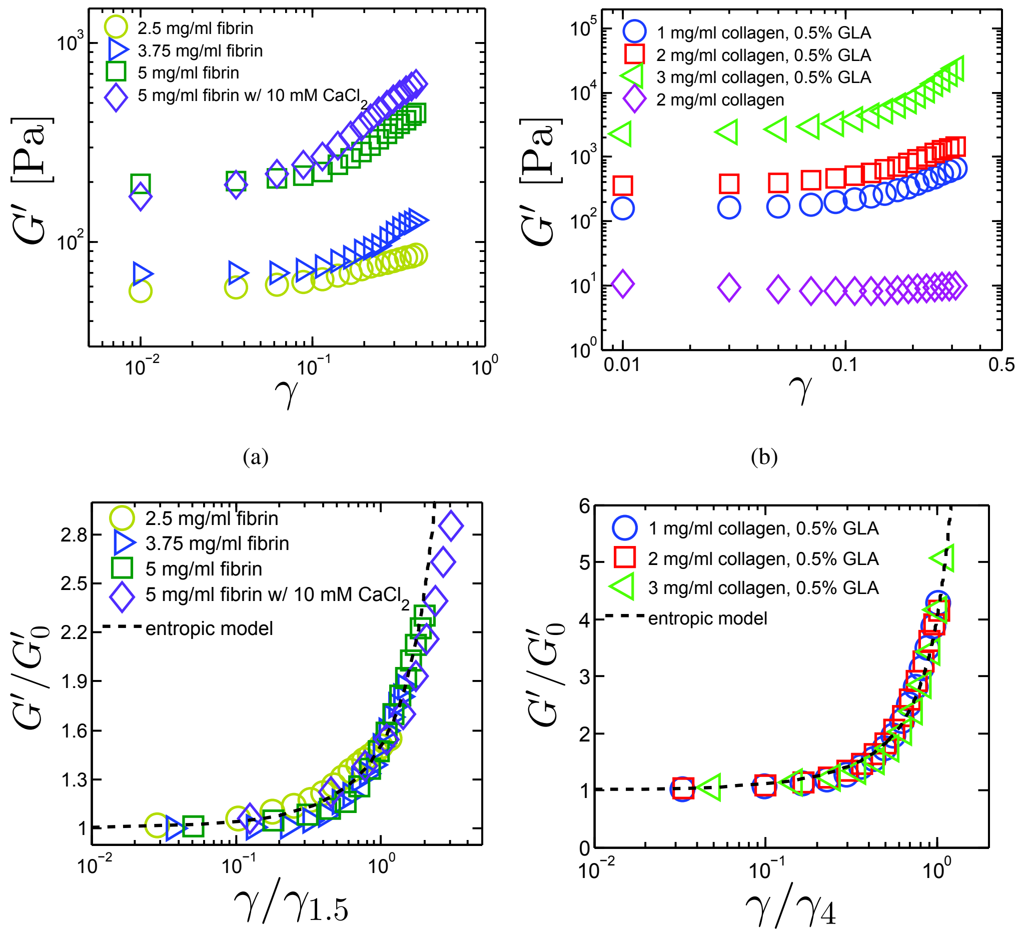

(a) (b)

(c) (d)

Figure 6.1: Rheology of semi-flexible gels. (a) G' of 2.5 mg/ml, 5 mg/ml and 5 mg/ml (10mM Ca^{2+} ions) fibrin gels in tris buffer at pH = 7.4, as function of shear strain. (b) G' vs. γ for type I collagen gels in 1× PBS buffer, at 1 mg/ml, 2 mg/ml, 3 mg/ml polymer concentrations crosslinked with 0.5% GLA, and 2 mg/ml collagen gel without any cross-links. (c) Scaled modulus, $\frac{G'}{G'_0}$ vs. scaled strain, $\frac{\gamma}{\gamma_{1.5}}$ curves for fibrin gels at different conditions. (d) $\frac{G'}{G'_0}$ vs. $\frac{\gamma}{\gamma_4}$ curves for cross-linked collagen gels. In (c) and (d), G'_0 is the zero-strain shear modulus; $\gamma_{1.5}$ is the strain at which $G' = 1.5G'_0$ (c), and γ_4 is the strain at which $G' = 4G'_0$ (d). Dashed lines in (c) and (d) indicate fit to an entropic model for strain-stiffening semi-flexible polymer gels. All data shown here have been measured at an oscillatory frequency of 0.1 Hz. Shear moduli are extracted using LAOS analysis.

Significant strain stiffening behavior is witnessed in all fibrin samples for $\gamma \gtrsim 8\%$; 5mg/ml fibrin samples that have been gelled in the presence of 10 mM Ca^{2+} strain-stiffen to as much as four times ($4\times$) the shear modulus measured at 1% strain amplitude, up to 30% strain amplitude, as seen from Fig. 6.1(a). Strain-stiffening data from fibrin gels can be scaled to collapse on a master curve (Fig. 6.1(c)) when the shear modulus, G' is scaled by the zero-strain shear modulus, G'_0 (or $\gamma = 0.01$ in this case), *viz.*, $\frac{G'}{G'_0}$. The strain is scaled by the strain value, $\gamma_{1.5}$ at which G' is an arbitrarily chosen multiple of G'_0, or, as in case of fibrin gels, $G' = 1.5G'_0$, *viz.*, $\frac{\gamma}{\gamma_{1.5}}$. This scaling collapse can be captured well by the dashed line in Fig. 6.1(c) indicating the fit to the entropic model for non-linear elasticity in semi-flexible polymer gels proposed by Storm, *et al.* [138]. According to this model, non-linear elasticity and negative normal stress in semi-flexible polymer gels arise from the non-linear force-extension curve of a constituent polymer filament. The dashed line fit in Fig. 6.1(c) is described in detail in APPENDIX, Sec. C.1.

We note that low-strain stiffness in fibrin gels increases with increasing concentration, c, i.e., $G'_0 \propto c^a$ where $a \approx 1.8 \pm 0.21$. A similar concentration dependence of G' is exhibited by other semi-flexible polymer gels, e.g., F-actin gels [129, 93]. In contrast to fibrin and F-actin gels, a different power-law dependence between G'_0 and c is observed in collagen gels: $a \approx 4.6 \pm 0.15$ for GLA cross-linked collagen gel, and $a \approx 0.55 \pm 0.01$ for collagen gel without added cross-linking agents.

Elastic shear moduli can be tuned in collagen gels over many orders of magnitude, ranging from ~ 2 Pa for un-crosslinked collagen gels at 2 mg/ml polymer concentration to ~ 2000 Pa for 3 mg/ml collagen gels with 0.5% glutaraldehyde cross-links, as seen in Fig. 6.5(b). Note that the modulus of the 2 mg/ml gel with glutaraldehyde cross-links is almost two orders of magnitude higher than the 2 mg/ml collagen gel without added crosslinks. Significant strain-stiffening behavior in glutaraldehyde-crosslinked collagen gels is reported for the first time, as shown from Fig. 6.1(b). The elastic moduli for crosslinked collagen gels also exhibit scaling collapse similar to that seen in fibrin gels, shown in Fig. 6.1(d), when G' and γ are normalized by the zero-strain shear modulus (G'_0) and the strain at which $G' = 4G'_0$ (γ_4), respectively. The scaled data, $\frac{G'}{G'_0}$ vs. $\frac{\gamma}{\gamma_4}$ can also be sufficiently well-fitted by the entropic theory in [138], indicated by the dashed line in Fig. 6.1(d).

We also note that the rate of strain-stiffening in both fibrin and collagen gels increases with increasing polymer concentration, c. This phenomenon is discussed further in Section C.2 of the APPENDIX.

6.2.1.2 First Normal Stress Difference, $N1$

First normal stress difference, $N1$, in fibrin and collagen gels are also measured as functions of γ and c, using the rheometer. Fibrin and collagen gels, being composed of semiflexible polymer filaments, exhibit significant negative normal stress, $N1$ [62, 155] as shown in Fig. 6.2. Notice that $N1$ decreases as γ increases- starting at $\gamma \approx 8\%$, we find that $N1$ decreases non-linearly. $N1$ can be expressed as a power series of γ that is composed of even power terms only, and is dominated by the quadratic term [66]. The decrease in $N1$ with γ are fitted to quadratic (even) functions of γ (i.e., $N1(\gamma) = A\gamma^2 + B$), as indicated by the dashed lines in Fig. 6.2. The collagen data is well-fitted by the (even) quadratic function for the entire range of applied strain (Fig. 6.2(b)); For fibrin gels, the $N1$ behavior is not captured well by the quadratic fit at low strains; however, the fits get better at higher strains ($\gamma > 0.2$).

We find that for a given γ, the higher the polymer concentration, c, the more marked is the

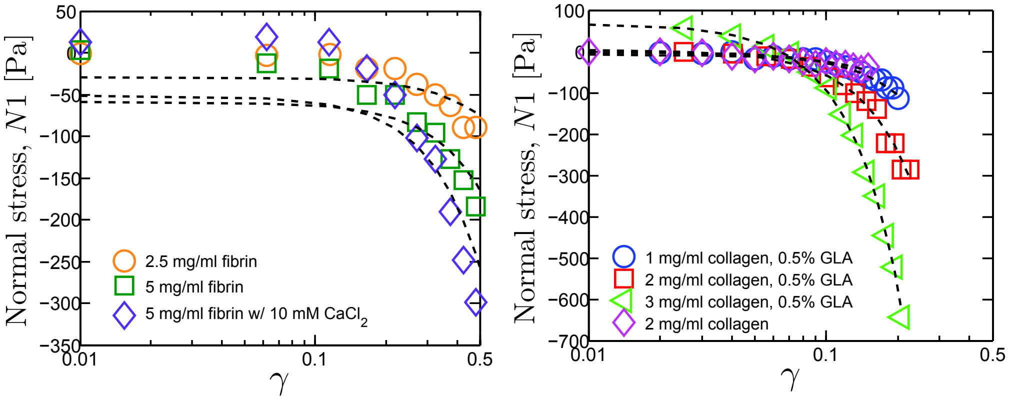

(a)

(b)

Figure 6.2: (a) Normal force, $N1$ vs. shear strain for 2.5 mg/ml, 5 mg/ml and 5 mg/ml (10mM Ca^{2+} ions) fibrin gels. (b) $N1$ vs. γ for 1 mg/ml, 2 mg/ml, 3 mg/ml collagen gels, each crosslinked with 0.5 % glutaraldehyde, and an uncrosslinked 2 mg/ml collagen gel ($\omega =$ 0.1 Hz). Dashed lines indicate quadratic (even) power γ fits to $N1$.

negative normal stress, $N1$ in fibrin and GLA-crosslinked collagen gels (Fig. 6.2). This behavior is consistent with the entropic elasticity model for semiflexible polymer networks [62], where N1 is predicted to *decrease* with increasing polymer concentration, as opposed to the enthalpic model [20], where N1 increases with increasing polymer concentration. Negative values of N1 has been ascribed to the asymmetric force-elongation relation of semi-flexible polymers. It is posited that filament stretching causes positive normal stresses, while filament bending pull the rheometer plates together, giving rise to negative normal stresses [66]. Since bending a filament requires less force than stretching it, this leads to an imbalance between forces resisting elongation compared to the forces needed to compress filaments between network junctions, and a net negative normal stress results [82].

6.2.2 One-point Non-affine Parameter, $\mathcal{A}$

Confocal microscopy is used to visualize and record the displacements of the fluorescent tracer beads entrapped within a $(70\ \mu\text{m} \times 70\ \mu\text{m} \times 60\ \mu\text{m})$ volume in the gel samples. Since the tracer beads' size of $\sim 1\ \mu$m is larger than the average mesh-size of the sample gels, free Brownian motions of the beads are suppressed. Within this small volume located approximately 1 cm from the axis of rotation, the macroscopic shear strain applied to the beads is approximately unidirectional.

In Fig. 6.3(a), bead displacements along the x, y, and z axis, are plotted as a function of the distance z_{0i} between the unsheared beads and the bottom surface. The displacements along the direction of shear, *viz.*, the x-axis, increase linearly with z_{0i} suggesting that the macroscopic shear deformation is affine. Fitting d_x to a linear function of z_{0i} yields the strain $\gamma_x \approx \gamma$. d_y and d_z, both perpendicular to the shear direction, are independent of z_{0i}, as shown in Fig. 6.3(a),(c) for a 2 mg/ml collagen gel (0.5% GLA) and 5 mg/ml fibrin gel respectively. It is interesting that the non-affine displacement along the z-axis, d_z is somewhat larger than that along y-axis. Since semi-flexible polymer gels like fibrin and collagen exhibit significant negative normal stress [62], the displacements along the z-axis may be indicative of the normal stress effects perpendicular to shear plane. [Note though, $d_z > d_y$ holds only for low strains, i.e., $\gamma \leq 0.05$; as strains increase, $d_y \approx d_z \sim 0$.]

The non-affine displacements of the tracer beads along each axis, *viz.*, $\vec{u}_x$, $\vec{u}_y$ and $\vec{u}_z$, are much larger than the resolution of our system in the $xy-$ plane ($\sim 50\ nm$) and the z axis (~ 100 nm). $\vec{u}_x$, $\vec{u}_y$ and $\vec{u}_z$ are normally distributed with mean value zero, i.e., distributed around the affine displacement positions (Fig. 6.3(b),(d)). Tracking resolution for the confocal microscope

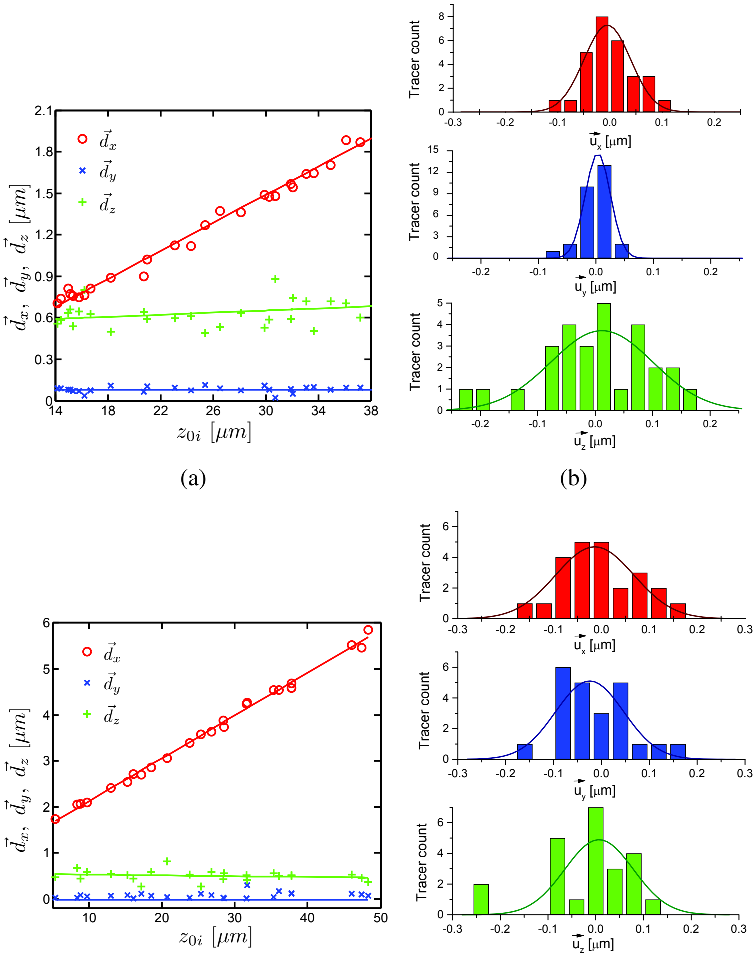

(a) (b)

(c) (d)

Figure 6.3: (a) Sample fibrin gel (5 mg/ml). Experimentally measured displacements of tracer beads in the direction of shear, d_i, that has been decomposed along x-, y- and z- axes, as a function of the distance, z_{0i} from the fixed lower plate of the rheometer. The solid lines indicate strains, γ_x, γ_y, and γ_z obtained from linear fits. Note that γ_y, and γ_z are ≈ 0. (b) The distribution of non-affine deviations of tracer beads for the same fibrin gel sample is shown in Fig. 6.3(a) at $\gamma = 0.12$, decomposed along the x-, y- and z- axes. The measurements are normally distributed around the *affine* displacement position, as indicated by the solid curves. (c) and (d) are the same as (a) and (b), but for a 2 mg/ml collagen gel (0.5% GLA) sample.

is $\sim$ 50 nm in the xy-plane and $\sim$ 80 nm along the z axis. These uncertainties set the tracking noise floor for $\mathcal{A} \sim 0.007\mu m^2$ (See Chapter 4).

The non-affine parameter $\mathcal{A}$ is computed from the measured bead displacements using Eq.(3.1). We plot $\mathcal{A}$ as a function of strain, γ, for a 5 mg/ml fibrin gel sample (Fig. 6.4, (top)) and 1 mg/ml collagen (0.5 % GLA) gel sample (Fig. 6.4, (bottom)). Note that $\mathcal{A}$ increases with γ. The exact nature of this dependence is extracted from the slope of the linear fit to the data which have been plotted in logarithmic scales. For $\mathcal{A} \propto \gamma^B$, we note that B ranges between $1.2 \rightarrow 2.1$. This behavior is typical of semi-flexible gels [5, 55], and distinguishable from the linear elasticity predictions of $B \approx 2$ for flexible polymer gels [23, 8].

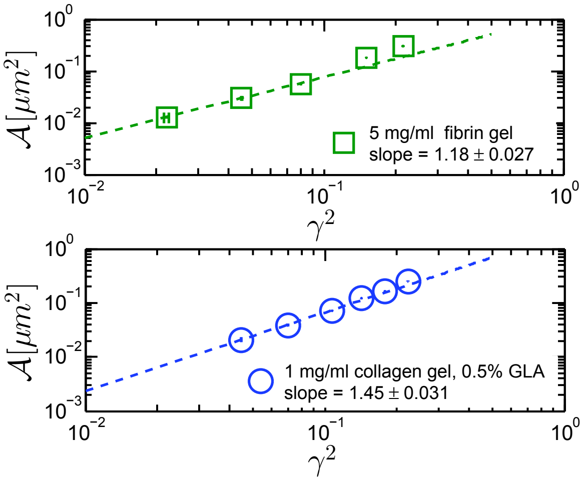

Figure 6.4: $\mathcal{A}$ scales with applied strain, γ for 5 mg/ml salmon fibrin gel (top), and 1 mg/ml type I Collagen gel with 0.5% GLA crosslinks (bottom). Error bars for $\mathcal{A}$ and γ are smaller than the marker size.

From similar log-log plots as Fig. 6.4, we extract the exact dependence of non-affine parameter, $\mathcal{A}$ on strain for individual samples of collagen and fibrin gels at different polymer concentrations and polymerization conditions. These values are listed in the APPENDIX, Section C.3.

The strain-normalized non-affine parameter, $\frac{\mathcal{A}}{\gamma^2}$ provides a good measure of the degree of non-affinity of any polymer sample [90, 8]. We will use this parameter for comparing the degree of non-affinity among different experimental conditions. $\frac{\mathcal{A}}{\gamma^2}$ is calculated for each sample as follows: for a particular strain, $\mathcal{A}$ is calculated by averaging the square of the non-affine displacements, $\vec{u}_i^2$, for all tracer beads in the sample; typically we carry out multiple shear measurements at the same strain, and the displacement data from all particles from the repeated shear measurements are averaged together to derive the mean $\mathcal{A}$ and its standard deviation. The large error bars in the $\frac{\mathcal{A}}{\gamma^2}$ values arises primarily from microscopic variations in gels polymerized under (ostensibly) identical experimental conditions.

$\frac{\mathcal{A}}{\gamma^2}$ is plotted as a function of γ for fibrin gels (Fig. 6.5(a)), GLA-crosslinked collagen gels (Fig. 6.5(b)) and uncrosslinked collagen gels (Fig. 6.5(c)). Several features are immediately evident: the first thing we notice is that notice that, on average, $\frac{\mathcal{A}}{\gamma^2}$ is much greater ($\left[\frac{\mathcal{A}}{\gamma^2}\right]_{fibrin} \approx 10\ \mu m^2$, $\left[\frac{\mathcal{A}}{\gamma^2}\right]_{collagen} \approx 25\ \mu m^2$, and $\left[\frac{\mathcal{A}}{\gamma^2}\right]_{collagen\ w/\ GLA} \approx 30\ \mu m^2$) than that measured for flexible polyacrylamide (PA) gels ($\left[\frac{\mathcal{A}}{\gamma^2}\right]_{PA} < 2\ \mu m^2$) [8]. Secondly, $\frac{\mathcal{A}}{\gamma^2}$ decreases as a function of γ, especially at low γ. Thirdly, for a given type of polymer gels, $\frac{\mathcal{A}}{\gamma^2}$ decreases with increasing polymer concentration, c, and decreasing polymer filament thickness (Fig. 6.7).

6.2.2.1 $\frac{\mathcal{A}}{\gamma^2}$ Decreases with Increasing γ, for Low Strains

To understand the decrease in non-affinity in semi-flexible polymer gels under shear, one needs to investigate the mechanism by which they deform. Unlike flexible polymer gels in which rigidity under shear comes from the resistance offered by the crosslinks to deformation ($G' = dk_BT$, where d = crosslink density, k_B = Boltzmann's constant, and T = temperature) [145], the shear modulus for semi-flexible polymers derives rigidity from both the cross-links as well as the

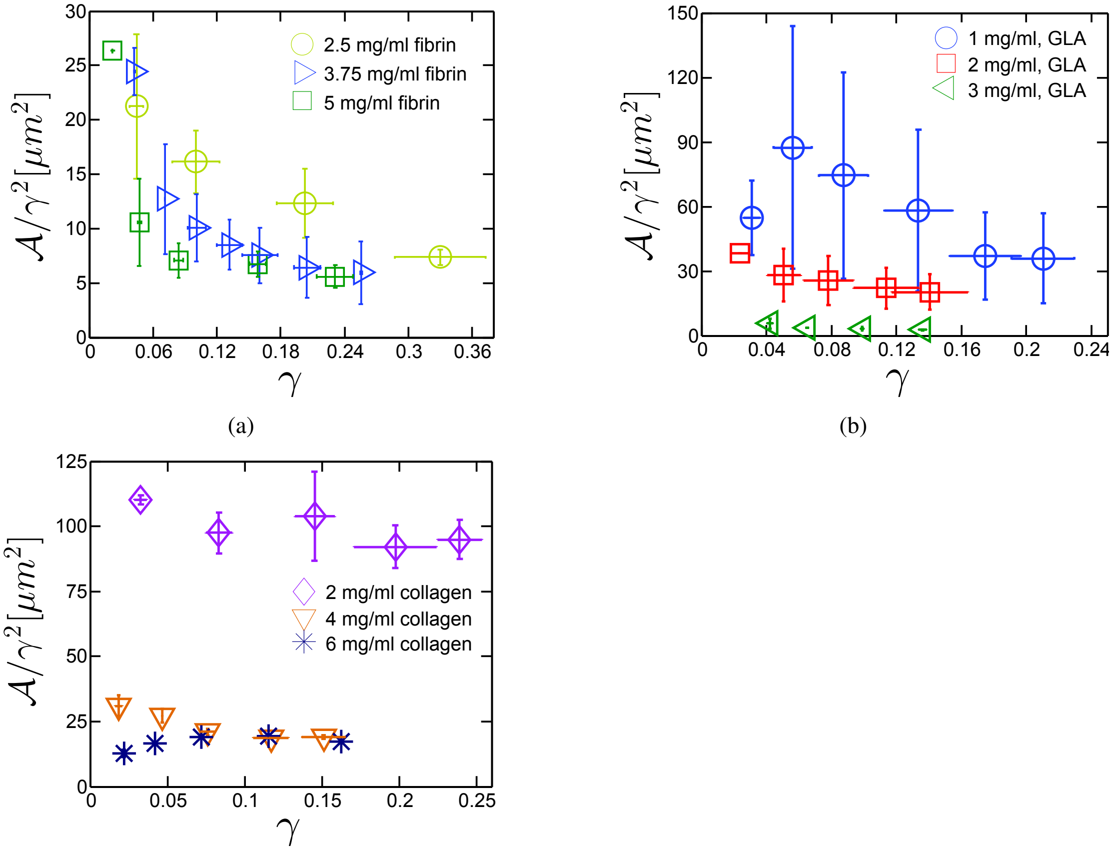

(a) (b)

(c)

Figure 6.5: (a) $\frac{\mathcal{A}}{\gamma^2}$ is plotted as a function of applied strain for (a) 2.5mg/ml and 5mg/ml fibrin gels, (b) collagen gels with 1mg/ml, 2mg/ml, and 3mg/ml polymer concentration, each with 0.5% GLA cross-links, and (c) 2mg/ml, 4mg/ml, and 6mg/ml uncrosslinked collagen gels. With a few exceptions overall, we note that the strain-normalized non-affinity parameter, $\frac{\mathcal{A}}{\gamma^2}$ (A) decreases with increasing polymer concentration, and (B) decreases with increasing γ.

polymer filaments. Deformation under shear in the latter case comes not only with the entropic cost of stretching out filament fluctuations, but also on the enthalpic cost of bending the semi-flexible filaments. Finite element simulations [115, 55] have shown that non-affine deformations result from the collective behavior of the constituent filaments in a network: under low shear strains, network filaments bend; at intermediate strains, the network filaments tend to reorient themselves in the direction of shear to accommodate the growing strains, and under even larger shear, the filaments cooperatively stretch in the shear direction. These models predict decreasing non-affinity with increasing strain, similar to what we observe in Fig. 6.5. This decreasing non-affinity accompanying the bending-to-stretching transition is predicted [115] for both rigid rod-like polymer gels, like collagen gels (Fig. 6.5(c)), as well as semi-flexible gels, like fibrin gels (Fig. 6.5(a)).

To understand the decrease in non-affinity measures in semi-flexible polymer gels under shear, one needs to look into the mechanism by which they deform. Unlike flexible polymer gels in which rigidity under shear comes from the resistance offered by the crosslinks to deformation ($G' = dk_BT$, where $d =$ crosslink dinsity, $k_B =$ Boltzmann's constant, and $T =$ temperature) [145], the shear modulus for semi-flexible polymers is the *sum* of the rigidity from the cross-links as well as the rigidity of the polymer filaments. Deformation under shear comes not only with the entropic cost of stretching out different filament configurations, but also an enthalpic cost of bending the semi-flexible filaments. Finite element simulations [115, 55] have shown that non-affine deformations result from the collective behavior of the constituent filaments in a network: under low shear strains, network filaments bend; at intermediate strains, the network filaments tend to reorient themselves in the direction of shear to accommodate the growing strains, and under even larger shear, the filaments cooperatively stretch in the shear direction. These models predict decreasing non-affinity with increasing strain, similar to what we observe in Fig. 6.5. This decreasing non-affinity accompanying the bending-to-stretching transition is predicted [115] for both rigid rod-like polymer gels, like collagen gels (Fig. 6.5(c)), as well as semi-flexible gels, like fibrin gels (Fig. 6.5(a)).

6.2.2.2 $\frac{\mathcal{A}}{\gamma^2}$ Decreases with Increasing Polymer Density

Strain-normalized non-affine parameter, $\frac{\mathcal{A}}{\gamma^2}$ for an arbitrarily chosen value of strain, viz., $\gamma = 0.1$ is plotted as a function of polymer chain density in Fig. 6.6 for (a) fibrin gels, (b) collagen gels with glutaraldehyde cross-links, and (c) uncross-linked collagen gels. In all three cases presented, we see that there is a decrease in $\frac{\mathcal{A}}{\gamma^2}$ measured with increasing polymer concentration. This can be explained as follows: as the concentration of polymer chain density is increased, the gels formed are better behaved with lesser network imperfections like voids, dangling chain ends, etc. In all three types of polymer gels we investigate, we see that as polymer density is increased, gels become increasingly affine, consistent earlier results [46, 157, 90]. The exact nature of this functional dependence is not obvious or universal though, and seem to be directly related to the exact nature of the gelation mechanism (e.g., whether there is any formation of proto-fibril bundles, etc.). Notice that this behavior is markedly different from that of PA gels [8] where there is no measureable dependence of non-affinity on polymer chain concentration. Rather, non-affinity measures are largely dominated by the presence of inhomogeneities typical in these gels [8].

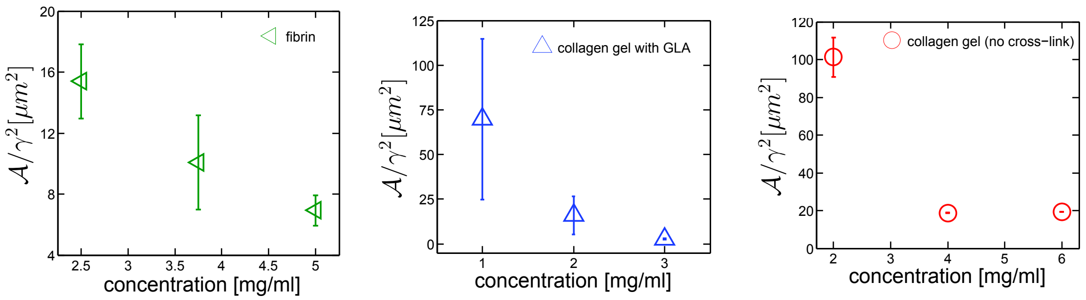

(a) (b) (c)

Figure 6.6: Strain-normalized non-affine parameter, $\frac{\mathcal{A}}{\gamma^2}$ decreases with increase in polymer density for (a) Fibrin gels, (b) Collagen gels with glutaraldehyde (GLA) cross-links, and (c) Uncross-linked collagen gels.

6.2.2.3 $\frac{\mathcal{A}}{\gamma^2}$ Increases with Increasing Fiber Diameter

Fig. 6.7 plots $\frac{\mathcal{A}}{\gamma^2}$ as a function of applied strain for collagen and fibrin gels with identical initial polymer concentration, but with different effective polymer diameters for the resultant gels. This is accomplished in fibrin gels by the addition of divalent cations during polymerization (10 mM Ca^{2+} to a 5 mg/ml fibrin gel), which leads to the formation of thicker bundles of fibrin filaments, thus increasing the fiber diameters [128] (Fig. 6.7(c)). Fibrin bundles are absent in gels without additional Calcium cations (Fig. 6.7(b)). For collagen gel, the addition of glutaraldehyde crosslinks markedly changes the nature of the resultant polymer network. In the absence of glutaraldehyde, thin collagen proto-fibrils bundle together into thick fibers which then branch off to form a volume-spanning network. This is usually a slow process where the typical gelation time for a 2 mg/ml gel is $\sim 2.5 - 3$ hr. In the absence of any real cross-links, the gels formed are much softer, with shear modulus $\sim$ 2 Pa. Typical filament thickness is $\sim 300 - 400$ nm with a high degree of poly-dispersity in diameter (Fig. 6.7(f)). Addition of glutaraldehyde, an effective cross-linking agent [112, 102], leads to the formation of a 3D filamentous network before the collagen proto-fibrils can form substantially thick bundles, leading to a well-crosslinked network (G' $\sim$ 2000 Pa) with relatively thin filaments of $\sim$ 60 nm diameter, as estimated from SEM images, shown in Fig. 6.7(e).

$\frac{\mathcal{A}}{\gamma^2}$ for semi-flexible polymers increases with an increase in fiber diameter, as seen from Fig. 6.7, for 5 mg/ml fibrin gel (a), and 2 mg/ml collagen gels (d). In Fig. 6.7(a), the fibrin sample with Ca^{2+} added has thicker filaments and higher $\frac{\mathcal{A}}{\gamma^2}$ of the two; similarly, Fig. 6.7(b) shows that the collagen gel without GLA cross-links, which has thicker network filaments as a result, has significantly higher $\frac{\mathcal{A}}{\gamma^2}$. Since the effective persistence length of a polymer filament is directly

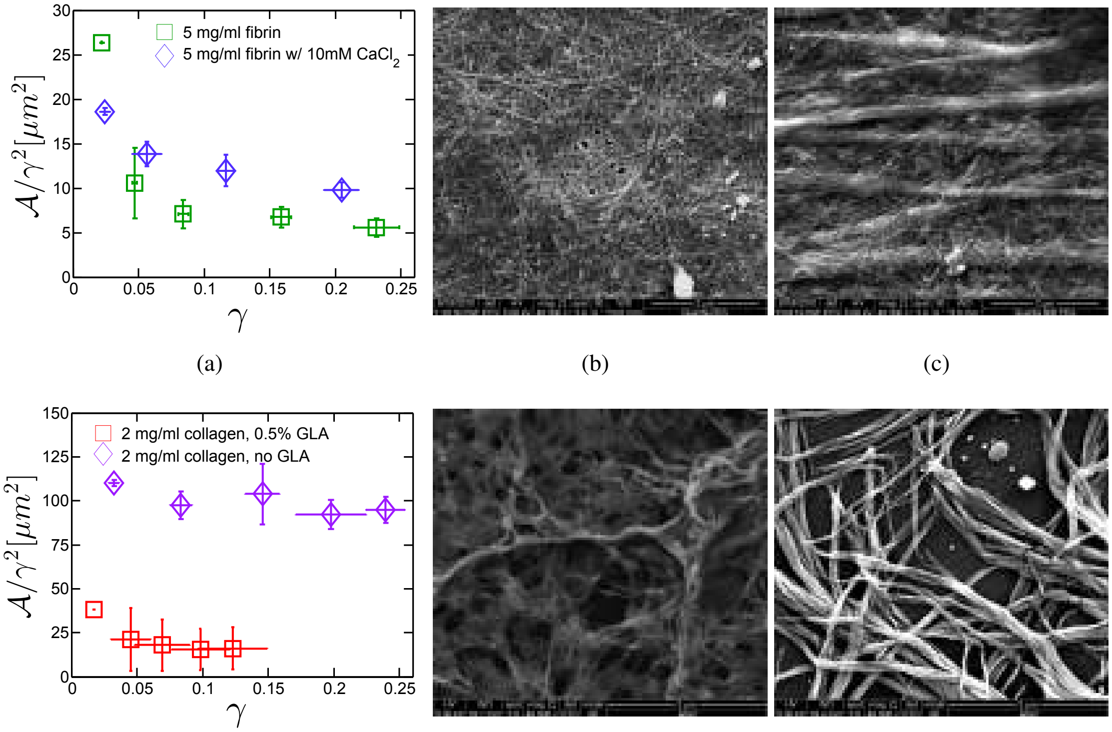

(a) (b) (c)

(d) (e) (f)

Figure 6.7: (a) $\frac{\mathcal{A}}{\gamma^2}$ is plotted as a function of applied strain for 5 mg/ml fibrin gels, with and without 10 mM Ca^{2+} ion buffer. SEM image of a 5 mg/ml fibrin gel without (b), and with (c) Ca^{2+} ions. Fibrin with Ca^{2+} ions have thick fiber bundles interspersed in the gel (b), which are absent in the gel without any divalent ions. (d) Strain-normalized non-affine parameter, $\frac{\mathcal{A}}{\gamma^2}$ is plotted as a function of applied strain for 2 mg/ml collagen gels with and without 0.5% glutaraldehyde cross-links. SEM image of a 2 mg/ml collagen gel with (e), and without (f) 0.5% GLA crosslinks.

proportional to the square of the filament's diameter [138], an increase in the overall diameter of the polymer filaments can be directly correlated to a corresponding increase in persistence length, and hence the stiffness of the constituent filaments. This implies that, for gels with a given polymer concentration, the stiffer the constituent polymer filaments, or higher the l_p, the higher the $\frac{\mathcal{A}}{\gamma^2}$ measured. Of course, this could also be because the gels with thicker filaments has lesser number of network junctions or "cross-links". (Note that since we start with the same gel monomer concentration, say $c = n_1.d_1.l = n_2.d_2.l$, if more proto-fibrils are used up to thicken the network filaments, i.e., if $d_2 > d_1$, there will be less number of network filaments, i.e., $n_2 < n_1$, and hence less number of filament overlaps or network junction points, or ’cross-links’, l being the average length of network filaments, and n_1, n_2 the number and d_1, d_2 the diameter of the thicker and thinner network fibers, respectively.) This results in a more imperfect, loosely-connected, floppy network which would also result in higher non-affinity.

Looking at the data from collagen and fibrin gels altogether, some overall trends emerge. First, there is significant non-affinity measured in semi-flexible polymers and this is much higher on average than that measured in flexible PA gels [8]. Second, $\frac{\mathcal{A}}{\gamma^2}$ is a function of strain: non-affinity decreases with increasing strain and tends to flatten out to a constant at large strains (Fig. 6.5). Third, non-affinity decreases with increasing polymer concentration (Fig. 6.6). Fourth, for a given polymer concentration, the thicker the network fibers (or stiffer the fibers), the higher the non-affinity measured (Fig. 6.7). The last three observations can be combined into a schematic (Fig. 6.8) for non-affinity measures in semi-flexible gels as a function of applied strain, γ, polymer chain concentration, c, and inverse persistence length, $1/l_p$. We posit that the affine-to-non-affine transitions along all three parameter axes are continuous.

6.2.2.4 Tracer Bead-size Dependence of $\frac{\mathcal{A}}{\gamma^2}$

We also explored the effect of the size of the tracer beads on the magnitude of $\mathcal{A}$, using tracer beads of three different sizes, viz., 0.6, 1 and 1.5 μm. The different-sized beads are fluorescently labeled such that they are uniquely excited by three different wavelengths of the confocal scanning beam. We disperse these three types of beads in a 3.75 mg/ml fibrin gel, and two 2 mg/ml collagen gel samples, with and without glutaraldehyde cross-links, and image them using excitation beams at three different wavelengths during a particular shear event.

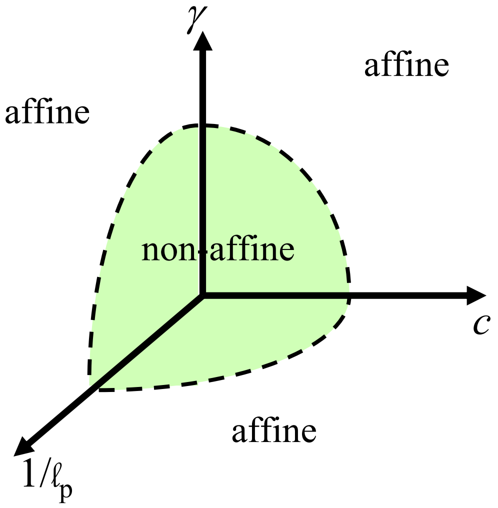

Figure 6.8: Non-affinity schematic for semi-flexible polymer gels as function of applied shear, γ, polymer concentration, c, and inverse persistence length of polymer filaments, $1/l_p$.

We note that non-affinity in the 3.75 mg/ml fibrin gel sample increases with increasing tracer-bead size, as seen from Fig. 6.9(a). Interestingly, there is no significant dependence of non-affinity measure on tracer-bead size for the 2 mg/ml collagen gel without any external cross-links, as seen from Fig. 6.9(b). However, for the 2mg/ml collagen gel with GLA (Fig. 6.9(c)), we notice that while there is no difference in the $\frac{\mathcal{A}}{\gamma^2}$ values for two of the larger bead-sizes, the $\frac{\mathcal{A}}{\gamma^2}$ measured using the 0.6μm tracer bead is consistently smaller.

6.2.3 Two-point Non-affinity Correlation Function, $\mathcal{G}_{ij}(r-r')$

Due to the small number of tracer beads ($\sim 35-40$) used in the non-affinity measurements, the average distance between tracer beads is of the order of tens of microns and this does not allow for very good statistics either. Since $\mathcal{G}_{ij}(r-r')$ dies off as $\frac{1}{|r-r'|}$ [23], at large separations ≥ 5 μm, there not much non-affinity correlation between tracer bead pairs. One trend invariably persists in all three types of polymer gel classes probed: we note that $\mathcal{G}_{ij}(r-r') \equiv$

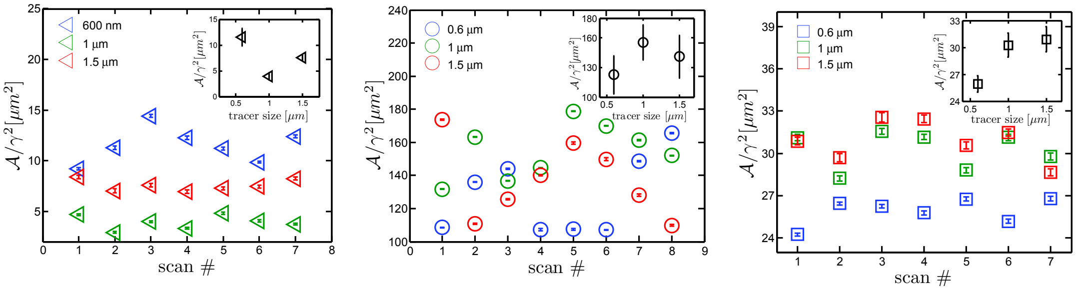

(a) (b) (c)

Figure 6.9: Average $\frac{\mathcal{A}}{\gamma^2}$ as a function of tracer bead size, *viz.* 0.6μm, 1μm and 1.5μm for (a) 3.75 mg/ml fibrin gel (pH=7), (b) 2 mg/ml collagen gel sample, and (c) 2 mg/ml collagen gel sample crosslinked with 0.5% GLA. Both collagen samples are prepared in 1x PBS buffer. Average $\frac{\mathcal{A}}{\gamma^2}$ was calculated from $\gamma = 0.08$ shear events repeated eight times.

$\langle \vec{u}_i(r) \cdot \vec{u}_j(r') \rangle$ increases with increasing strain applied on the samples, as seen in Fig. 6.10. We do not understand this behavior.

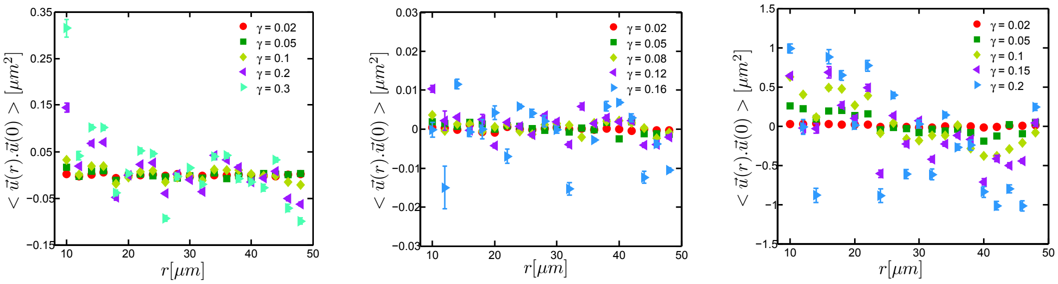

(a) (b) (c)

Figure 6.10: Two-point non-affine correlation for semi-flexible gels as a function of distance between tracer beads. (a) Sample 5 mg/ml fibrin gel in pH = 7.4 tris buffer. (b) Sample 2 mg/ml collagen gel in the presence of 0.5% GLA crosslinks. (c) Sample 2 mg/ml collagen gel.

6.2.4 Non-linear Elasticity and its Link with Non-affinity

Numerous recent theoretical and experimental studies have addressed the origin of elasticity of hydrogels, in particular the strain-stiffening of semiflexible biopolymer gels [93, 138, 45].

Assuming affine network deformation, various entropic models derive non-linear elasticity from the non-linear force-extension response of individual filaments comprising the gel. Another class of non-affine models account for the gel elasticity from an interplay between bending as well as stretching of semi-flexible or stiff filaments, and predict non-affine network deformation, as shown in Fig. 6.11. At low strains, network deformation is dominated by non-affine bending of polymer filaments. But as the applied strain increases, there is transition from filament bending to more affine stretching out of the entropic fluctuations of the polymer filaments, and network deformation becomes increasingly affine [157, 45]. Network rearrangements under external load have also been shown, both theoretically [125, 115, 56] and experimentally [36], to be an additional source of non-affinity.

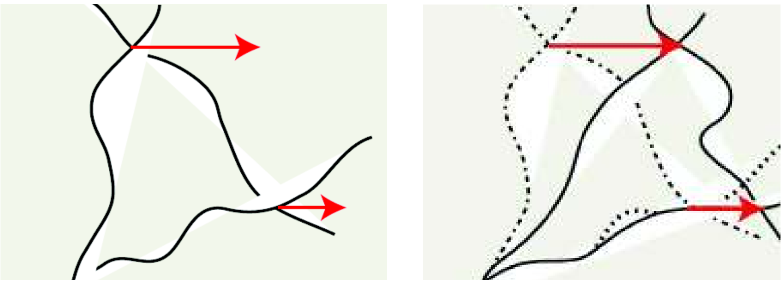

Figure 6.11: Interplay of bending and stretching of polymer segments in networks under shear. Unsheared network segment (left panel). Under shear, as indicated by the red arrows, the two longer segments get stretched, while the shorter one in between is bent (right panel).

6.3 Conclusions

In summary, we measure macroscopic elastic behavior and microscopic non-affine deviation in fibrin and collagen gels under shear. The macroscopic elasticity in bio-polymer network differs markedly from rubber elasticity in that it shows significant non-linear elasticity, in the form of strain-stiffening, and negative normal stress. The rate at which a sample exhibits strain-stiffening and normal stress as a function of strain increases with increasing polymer concentration. We note that all macroscopic elasticity behavior can be explained by the entropic model of elasticity proposed by Storm, *et al.* [138].

Non-affine behavior is quantified by tracking displacements of fluorescent tracer beads in the polymer gels under shear. We see that non-affinity measures, in general, are much larger in semi-flexible polymer networks than in flexible PA gels [8]. Also, unlike in PA gels, non-affinity measures depend on polymer concentrations- the higher the polymer concentration, the lower the non-affinity. There is also a dependence on shear strain- $\frac{\mathcal{A}}{\gamma^2}$ decreases with increasing shear strain. For a given initial monomer concentration, gels with stiffer polymer filaments exhibit higher non-affinity. As we have seen in Chapter 2, non-affine deformation in bio-polymer gels may be the result of such diverse phenomena as filament bending, entropic extension of worm-like chains, or network rearrangements, or a combination of these; a picture that may be further complicated by the presence of network inhomogeneities. Given this complexity, we believe that a more appropriate way to test the validity of the theoretical models is to characterize the deformation of individual constituent polymers as part of a globally deforming gel.

Chapter 7

Macro-rheology of Soft Colloids Near the Jamming Transition

7.1 Experimental Procedure

7.1.1 Sample Preparation

NIPA microgel spheres are synthesized by free radical polymerization of N-isopropyl acrylamide with bisacrylamide crosslinker [130, 1]. Ammonium persulphate initiator used in NIPA particle synthesis leaves the particle surfaces slightly negatively charged, which prevents their aggregation in suspension. These microgel spheres are thermosensitive in water for a fixed range of temperature. In this range of temperature, NIPA particles interact in a pair-wise fashion via short-ranged, repulsive potentials given as $V(r_{ij}) = (\epsilon/a)(1 - r_{ij}/\sigma_{ij})^a$ for $r_{ij} > \sigma_{ij}$ and $V(r_{ij}) = 0$ for $r_{ij} \leq \sigma_{ij}$. Here, r_{ij} is the center-to-center distance between particles i and j, and σ_{ij} is the sum of their radii. Specifically, $a = 2$ for harmonic and $a = 5/2$ for Hertzian interactions. Previous experiments have shown that NIPA inter-particle interactions can, within error, be approximated by both Hertzian [108] and harmonic potentials [17].

Two different aqueous suspensions of NIPA microspheres are investigated. The first sample is an aqueous suspension of $\sim$700 nm diameter NIPA particles. The number density of the monodisperse NIPA microspheres is estimated to be $\sim 2.9 \times 10^{18}$/m^3. The second sample is an aqueous suspension of a bidisperse mixture of $\sim$500 nm and $\sim$700 nm NIPA particles (at $T = 298.5$ K) wherein the two particle species are present in approximately *equal number ratio*. The polydispersity of each particle type is $\sim 10\%$. The size-ratio of the NIPA particles in the bidisperse sample is roughly $1.4 : 1$, i.e., the same size-ratio commonly used to suppress crystallization in glassy/jammed systems. We estimate that the particle number density of each species in the bidisperse sample is $\sim 2.6 \times 10^{18}$/m^3.

7.1.2 Rheology

The samples are placed in an ARES-G2 rheometer shown in Fig. 7.1(a) capable of independent stress and strain measurements (TA Instruments, US), with 4^o/40 mm cone-and-plate geometry. The rheometer applies a torque to the sample, and the resultant rotation rate of the conical top plate is measured. The torques and rotation rates are converted into corresponding stresses and strain-rates, assuming that neither wall-slip nor shear-band formation occurs. Sample temperature is controlled and measured by a Peltier unit and thermocouple built into the rheometer. Care is taken to prevent sample evaporation during the experiment by using a solvent trap (Fig. 7.1(b)). A wide range of torque is applied to the samples over a wide range of temperature. Because of the thermo-responsive nature of the NIPA particles, the sample volume fraction decreases as the sample temperature is increased, and we are able to tune sample volume fractions through the jamming transition. Experiments are performed under continuous as well as oscillatory shear conditions to study both steady-state and time-dependent responses. For the range of stresses measured in these experiments, the particles are deformable but incompressible [108]. Under steady shear, nominal stress (σ) versus strain-rate ($\dot{\gamma}$) data are obtained as a function of volume fraction above and below the jamming transition, as discussed in Sec. 7.2.1. Similarly, shear elastic (G') and viscous (G'') moduli are recorded as a function of oscillatory frequency (ω) across the jamming transition, as shown in Sec. 7.2.2. All measurements are done in the linear elastic strain regime, wherein the peak strain amplitude is 2% or less.

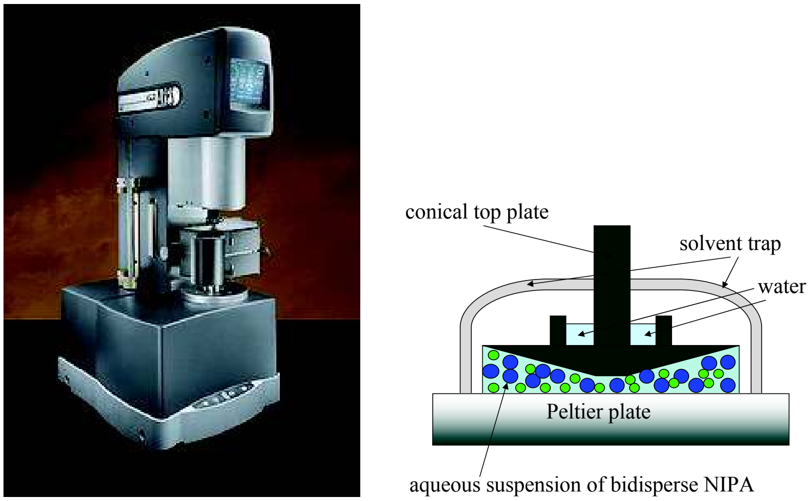

(a) (b)

Figure 7.1: (a) ARES-G2 rheometer (with 4^o/ 40 mm cone-and-plate geometry) used in the experiments. (b) Solvent trap used to prevent evaporation. Note that there is a small solvent reservoir on the conical plate that reduces solvent evaporation from samples.

Reynolds number (Re) is a dimensionless quantity often used to estimate the nature of fluid flow, whether laminar or turbulent. It is a function of the fluid properties, flow-rate, as well as the physical dimensions of the environment in which the flow occurs. For a simple fluid under flow, Re can be calculated under viscometry and oscillatory shear as follows:

$$Re = \frac{2\pi r h \rho \tan(\theta)\dot{\gamma}^2}{\sigma} \qquad \text{(steady-state)}, \tag{7.1}$$

$$Re = \frac{r h \rho \gamma \theta \omega^2}{2\pi\sqrt{G'^2 + G''^2}} \qquad \text{(frequency-dependent)}, \tag{7.2}$$

where, ρ is the density of NIPA microspheres, θ is the angle of the rheometer cone, r is the radii of the rheometer cone-and-plate, h is their maximum separation, γ is the shear strain, and G' and G'' are the shear storage and loss moduli respectively. Fig. 7.2 displays simple schematics for the two cases.

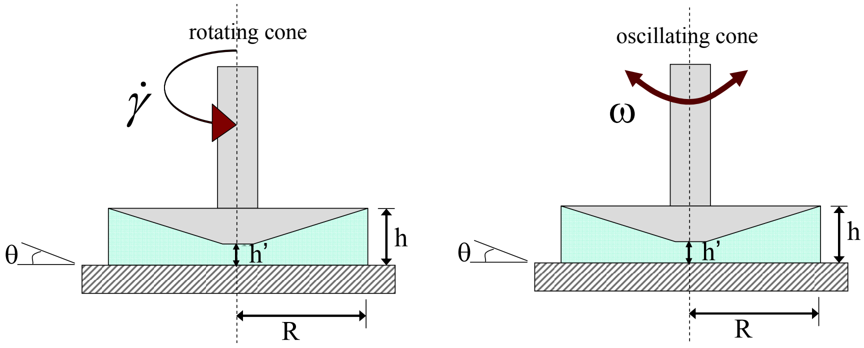

(a) Viscometry (b) Oscillatory

Figure 7.2: Schematics for (a) viscometry and (b) oscillatory modes. Here R is the radius of the sample-filled space, h' and h are the minimum and maximum separation of the rheometer plates, θ is the cone angle of the top plate, and $\dot{\gamma}$ and ω are the shear-rates and oscillatory frequencies in the (a) viscometry and (b) oscillatory modes, respectively.

As Re increases, flow behavior transitions from laminar or viscous force-dominated to turbulent or inertia-dominated. For $Re \approx 0.1$, the flow can be considered laminar and smooth, (also called creeping flow or Stokes' flow) [9]. Because a traditional rheometer has macroscopic dimensions (where r and h can both be of the order of mm), it is easy to have high Reynolds numbers and flow instabilities in rheology measurements. Special care is taken to restrict all data-sets to low Reynolds numbers ($Re < 0.5$) and thus ensure that laminar flow conditions are maintained at all times [9, 25]. This is accomplished by restricting $\dot{\gamma}$ and ω to correspondingly low values. The sensitivity required of the rheometer for such measurements as ours is more demanding than usual; we use an ARES-G2 rheometer with highly sensitive magnetic force transducers for this purpose. Because of the thermo-sensitive nature of NIPA microspheres, we also consider the rise in sample temperature from viscous drag– we estimate this to be less than a billionth of a Kelvin for the flow regimes considered in these experiments.

We do not believe that wall-slip has a significant effect for the systems and flow regimes we consider. To confirm this assumption, a set of control experiments were performed on a similar, albeit less sensitive instrument (Bohlin Gemini rheometer, Malvern Instruments, UK) with identical plate geometry. The effect of roughness of the rheometer surfaces was checked by performing representative experiments with and without roughening the rheometer cone and plate (these control experiments are discussed further in APPENDIX D.1). For the flow regimes considered in these experiments, surface roughness does not seem to have any noticeable effect on the resulting rheology data. Thus, though we were unable to roughen the cone and plate of the ARES-G2 rheometer that was used for the experiments, we do not anticipate wall-slip effects in this closely related instrument. Note also, wall-slip effects are more likely at high strain-rates and high oscillation frequencies [79], both of which are kept quite low ($\dot{\gamma} < 10$ 1/s, $\omega < 10$ rad/s) in the experiments.

Because increasing temperature shrinks the particles isotropically, shear history between different volume fractions is effectively erased [132]. Peclet numbers are high ($Pe > 2 \times 10^6$)

throughout all measurements, indicating that all motion are driven by shear forces as opposed to thermal diffusion.

7.1.3 Dynamic Light Scattering

Below a critical temperature at which NIPA becomes insoluble in water, NIPA particle diameter decreases linearly with increasing temperature. This linear relationship holds for a wide range of temperature, which permits the particle volume, and hence the effective volume fraction of the microgel suspensions, to be easily varied across the jamming transition. The diameter of NIPA particles is determined by dynamic light scattering (DLS). A standard light scattering set-up (Brookhaven Instruments Corporation, NY) is used for this purpose. A collimated laser beam at 632.8 nm wavelength is incident on a temperature-controlled dilute aqueous suspension of NIPA particles; the scattered light is collected by an avalanche photo-diode detector placed at a 60^o angle to the incident beam. For each data point, the scattered light temporal intensity autocorrelation function is measured for $\sim$5 minutes, at $\sim 25 \times 10^3$ photons per second. The thermosensitive *hydrodynamic* diameter of the NIPA microgel spheres is derived from the temporal decay rate of this correlation function at each temperature. The sizes of both species of NIPA particles, *viz.* 500 nm, and 700 nm, are measured using DLS as shown in Fig. 7.3.

The hydrodynamic diameters, *viz.*, D_1 for 500 nm and D_2 for 700 nm NIPA particles, respectively, change linearly with temperature, T, as seen from Fig. 7.3(a). The slopes, dD_1/dT and dD_2/dT, and intercepts, D_{10} and D_{20} of the linear fits for 500 nm and 700 nm NIPA particles respectively are reported in Table 7.1. They are used to convert the relative change, $|T - T_c|/T_c$, in sample temperature T with respect to the jamming transition temperature T_c, to a corresponding change in volume fraction $|\phi - \phi_c|$; here ϕ is the volume fraction at temperature T, and ϕ_c is

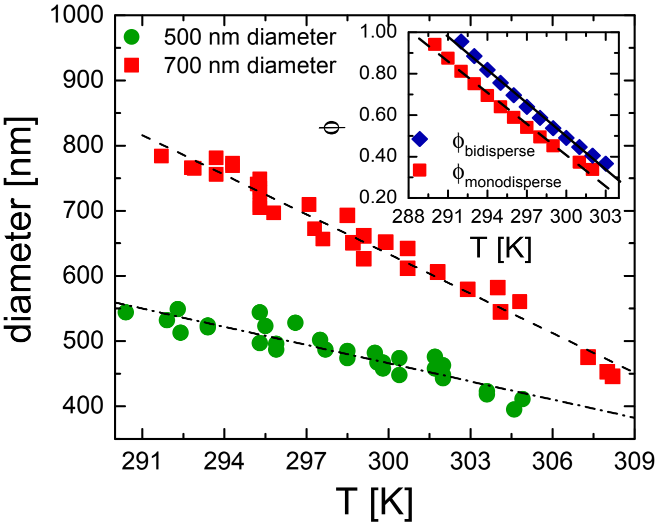

Figure 7.3: Hydrodynamic diameters of two species of NIPA particles are measured using dynamic light scattering. Dashed (700 nm) and dash-dot (500 nm) lines indicate linear best-fits. The slopes are listed in Table 7.1. The inset shows the packing fraction of the monodisperse and bidisperse NIPA systems as function of temperature. The dashed (monodisperse) and solid (bidisperse) lines are linear fits to the data.

the critical volume fraction at the jamming transition. The connection between volume fraction and temperature is computed via the following relation:

$$\phi = \frac{N\pi}{6}\left(D_{10} + \frac{dD_1}{dT}T\right)^3, \tag{7.3}$$

where N is the number density of NIPA particles. Similarly, for the bidisperse system, where the 500 nm and 700 nm NIPA microspheres are present in equal number densities, i.e., $N/2$, we calculate ϕ and ϕ_c using

$$\phi = \frac{N\pi}{12}\left[\left(D_{10} + \frac{dD_1}{dT}T\right)^3 + \left(D_{20} + \frac{dD_2}{dT}T\right)^3\right]. \tag{7.4}$$

The procedure by which T_c is obtained is discussed in Sec. 7.2.1.1. ϕ_c is then derived from these formulas (Eq. 7.3, 7.4) with $T = T_c$; ϕ_c thus obtained is a function of N. We assume that the critical jamming volume fraction, ϕ_c for both monodisperse and bidisperse NIPA systems is the random close packed (RCP) volume fraction, 0.64 [110, 111, 107, 132, 67]. This assumption and Eqns. 7.3, 7.4 permit estimation of N for both monodisperse and bidisperse systems; this value of N and Eqns. 7.3, 7.4 are then used to calculate ϕ for all other T. Note, we have investigated the effect of different critical volume fractions; using $\phi_c = 0.64 \pm 0.05$ does not change the important outcomes of our analyses in any significant way. The inset in Fig.7.3 shows volume fraction versus temperature for the monodisperse and bidisperse NIPA suspensions. The dashed (monodisperse) and solid (bidisperse) lines are linear fits to the data with correlation coefficient, $R \approx 0.99$ in both cases. The high R values indicate that the volume fractions are also approximately linear with temperature for the temperature ranges used in our experiments.

Sample	dD_i/dT [nm/K]	D_{i0} [nm]
500 nm	-10.3 ± 0.8	3548.3 ± 239.3
700 nm	-22.0 ± 1.4	7241.5 ± 434.3

Table 7.1: Fitting parameters obtained from linear fit of hydrodynamic diameters of NIPA particles as a function of temperature.

Note, the radius reported here is the particle hydrodynamic radius, R_h. We expect the hydrodynamic radius to be larger than the radius measured by static light scattering by a factor of approximately 1.1 [131, 122]. We use R_h for all calculations. The exact value of this constant factor is not crucial for any of our scaling results.

7.2 Results and Discussion

7.2.1 Steady Shear Data

The stress (σ), versus strain rate ($\dot{\gamma}$) data curves are plotted across the jamming transition in Fig. 7.4. Data on the jammed side, as indicated by the dashed lines, can be readily fit to the well-known Herschel-Bulkley (HB) phenomenological model [94, 100]: $\sigma = \sigma_y + k\dot{\gamma}^n = \sigma_y \{1 + (\tau\dot{\gamma})^n\}$. Here σ_y is the yield stress, k is the consistency (a material property characteristic of the system), n is the HB scaling exponent, and τ is a relaxation time-constant described by Nordstrom, *et al.* [107]. The HB model is commonly used for capturing the shear-thinning behavior of colloidal suspensions. The exponent, n is approximately $1/2$ for our jammed data; $n \approx 0.50 \ \pm 0.02$ for the monodisperse NIPA system, and $n \approx 0.48 \ \pm 0.01$ for the bidisperse system.

7.2.1.1 Scaling by χ^2-minimization

We next investigate possible critical scaling behavior in the σ versus $\dot{\gamma}$ data across the jamming transition. Such behavior has been found previously in simulation and microfluidic experiments [113, 107]. Specifically, σ vs. $\dot{\gamma}$ data were predicted to collapse onto two distinct curves, one above and one below jamming, when scaled as $\sigma/|\phi - \phi_c|^{\Delta}$ and $\dot{\gamma}/|\phi - \phi_c|^{\Gamma}$. Because ϕ is roughly linear in T (Fig. 7.3, inset), our first investigation uses the directly measured factors $(\frac{|T-T_c|}{T_c})^{\Delta}$ and $(\frac{|T-T_c|}{T_c})^{\Gamma}$ for rescaling σ and $\dot{\gamma}$, respectively, i.e., in lieu of the corresponding $|\phi - \phi_c|^{\Delta}$ and $|\phi - \phi_c|^{\Gamma}$. The best-fit scaling exponents, Δ, Γ, and the critical jamming temperature, T_c, are then deduced by finding the best collapse of the data onto the two separate branches *above* and *below* jamming.

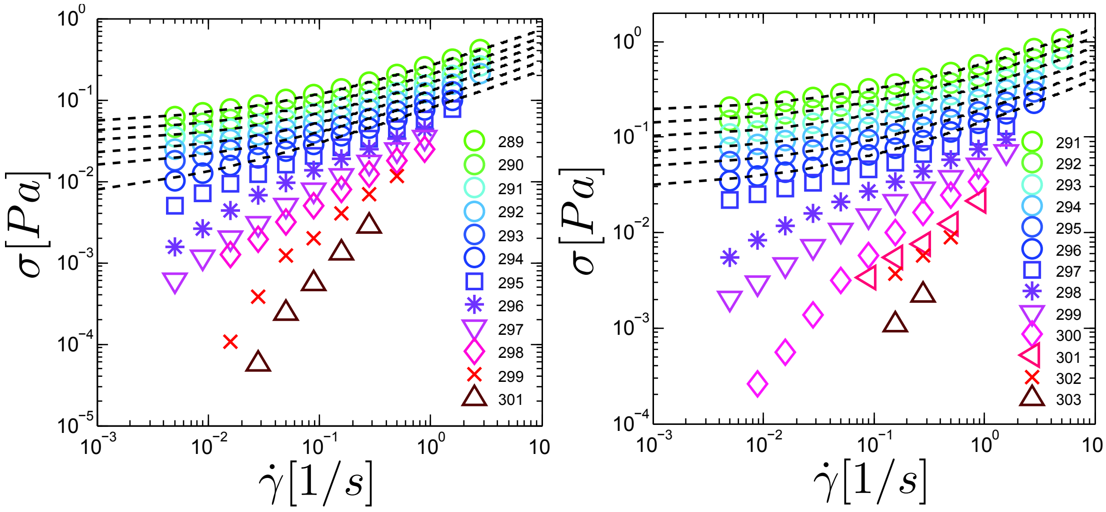

(a) Monodisperse (b) Bidisperse

Figure 7.4: Stress vs. strain-rate data for aqueous suspensions of (a) monodisperse NIPA microgel spheres (diameter, ∼700 nm; T → 289 K to 301 K, in steps of 1 K), and (b) bidisperse NIPA spheres (diameters, ∼500 nm, ∼700 nm; T → 291 K to 303 K, in steps of 1 K), obtained using bulk rheology. Each curve is obtained at a different temperature corresponding to a different particle volume fraction. Dashed lines are Herschel-Bulkley (HB) best-fits to the data in the jammed regime.

To this end we compute all plausible sets of data for Δ, Γ and T_c, generated in steps of 0.1, 0.1, and 0.1 degrees Celsius, respectively. Starting with the raw data, new data-sets of stress divided by $|(T - T_c)/T_c|^{\Delta}$ and strain-rate divided by $|(T - T_c)/T_c|^{\Gamma}$, are thus generated. The quality of collapse is judged by computing χ^2, the mean-square deviation between the scaled data and the best polynomial fit. This method was previously used in the Supplemental Material in [107].

We explored the use of different order polynomials up to fifth order for finding best fits to jammed and unjammed branches of the data. The goodness of the second-order and third-order polynomial fits for the jammed and unjammed branches, respectively, were comparable to the higher-order polynomial fits, and the asymptotic forms of the lower order polynomial fits close to the jamming point behaved reasonably well. We choose to use the second-order fits for estimating exponents of the jammed branch and third-order fits for the unjammed branch. Exponents from the various fits using different order polynomials are in agreement with one another within error bars. A three-dimensional contour plot of $log(\chi^2)$ values obtained for the monodisperse NIPA system, as shown in Fig. 7.5, shows that there is indeed a well-defined minimum from which the best-fit scaling exponents and critical temperature can be extracted. Fig. 7.5 displays $log(\chi^2)$ values obtained from fitting $\sigma/(\frac{|T-T_c|}{T_c})^\Delta$ vs. $\dot{\gamma}/(\frac{|T-T_c|}{T_c})^\Delta$ (to a second-order polynomial on the jammed side, and a third-order polynomial on the unjammed side) in the form of contour plots. Δ, Γ, and T_c are fitting parameters, the values of which are varied between $1 \rightarrow 9$, $1 \rightarrow 9$, and $291 \rightarrow 299$ K, respectively, in steps of 0.1, 0.1 and 0.1 K. Data shown here is from the monodisperse NIPA sample ($\sim$700 nm). Uncertainties in fit parameters are determined conservatively for each of the three scaling parameters by the difference between their values at the minimum and their values when χ^2 is increased by a factor of two.

The best-fit values of Δ, Γ and T_c thus obtained, along with the error estimates for both the monodisperse and bidisperse NIPA systems, are summarized in Table 7.2. Fig. 7.6 shows the best-fit of $\sigma/|(T-T_c)/T_c|^\Delta$ versus $\dot{\gamma}/|(T-T_c)/T_c|^\Gamma$ derived from the monodisperse data in Fig. 7.4(a), and the bidisperse data in Fig. 7.4(b). Dashed lines in the figures are the polynomial functions used for χ^2-minimization. In both samples, the fits capture the scaling collapse of the experimental data over many orders of magnitude around the jamming point; both jammed and unjammed branches are fitted reasonably well.

The linear relationships between sample temperature and NIPA particle diameter obtained

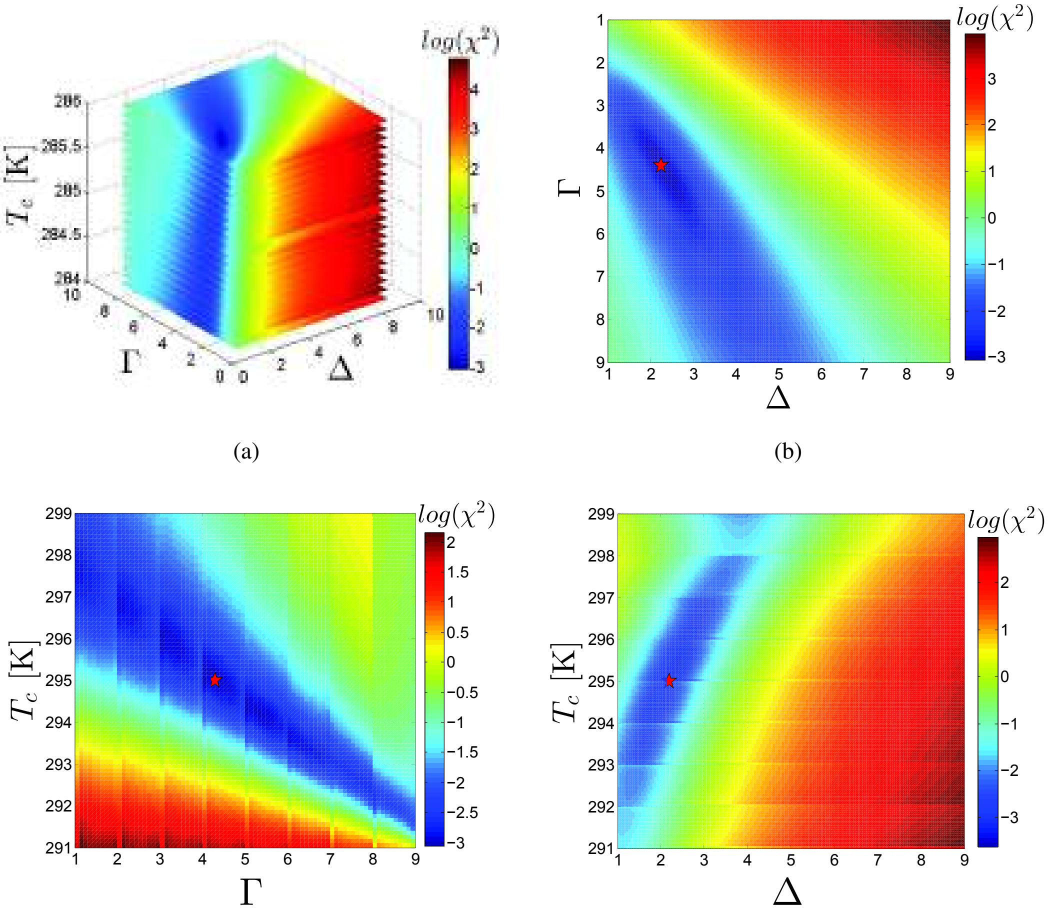

(a) (b)

(c) (d)

Figure 7.5: (a) Three-dimensional contour plot of $log(\chi^2)$ obtained from the polynomial fits to the scaled rheology data for the monodisperse NIPA sample. The blue end of the color-bar indicates low χ^2. The minimum χ^2 is indicated by the red star. Notice the well-defined dark blue ellipsoidal region in the contour plot from which the best-fit Δ, Γ and T_c values are extracted. (b), (c) and (d) show a slice each taken from the 3D contour plot of the monodisperse sample, where (a) T_c is held constant at 295 K while the scaling exponents, Δ and Γ and made to vary, (b) Δ is held constant at 2.2 while T_c and Γ and made to vary, and (c) Γ is held constant at 4.3 while T_c and Δ made to vary.

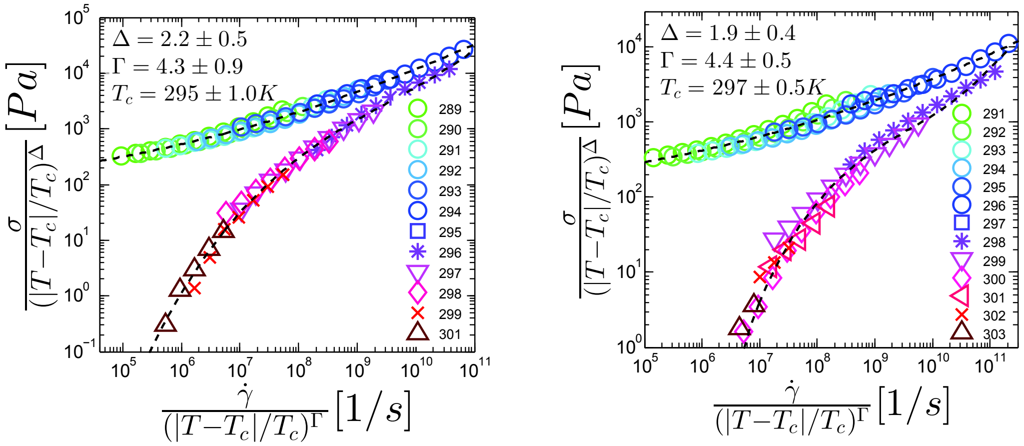

(a) Monodisperse

(b) Bidisperse

Figure 7.6: Optimized scaling collapses of bulk rheology data for aqueous suspensions of (a) monodisperse (diameter, ∼700 nm), and (b) bidisperse (diameters, ∼500 nm, ∼700 nm) NIPA microgel spheres. Temperature-difference scaled σ vs. $\dot{\gamma}$ data is shown. Exponents Δ, Γ and jamming temperature, T_c were derived by χ^2 minimization. The best-fit values of Δ, Γ and T_c are 2.2, 4.3, 295 K for monodisperse NIPA suspensions, and 1.9, 4.4, 297 K for bidisperse NIPA suspensions.

from DLS experiments (given in Eq. 7.3, 7.4) are next used to convert the critical jamming temperature, T_c and temperature difference from the jamming transition, i.e., $|T - T_c|/T_c$, into the corresponding critical jamming volume fraction, ϕ_c, and an analogous $|\phi - \phi_c|$. The corresponding best-fit scaling plots are shown in Fig. 7.7. Note that ϕ_c at the critical temperature, T_c, is assumed to be the critical volume fraction at RCP, *viz.*, $\phi_c = 0.64$, as discussed previously in 7.1.3. The quality of the scaling collapses using $|\phi - \phi_c|$ in both monodisperse and bidisperse systmes are comparable to those obtained using $|T - T_c|/T_c$. The values of Δ, Γ and T_c obtained in this manner for both the monodisperse and bidisperse NIPA systems are summarized in Table 7.2.

Note, we also analyzed our data following a third fitting scheme employed in [107]. This procedure and results are briefly described in APPENDIX D.2.)

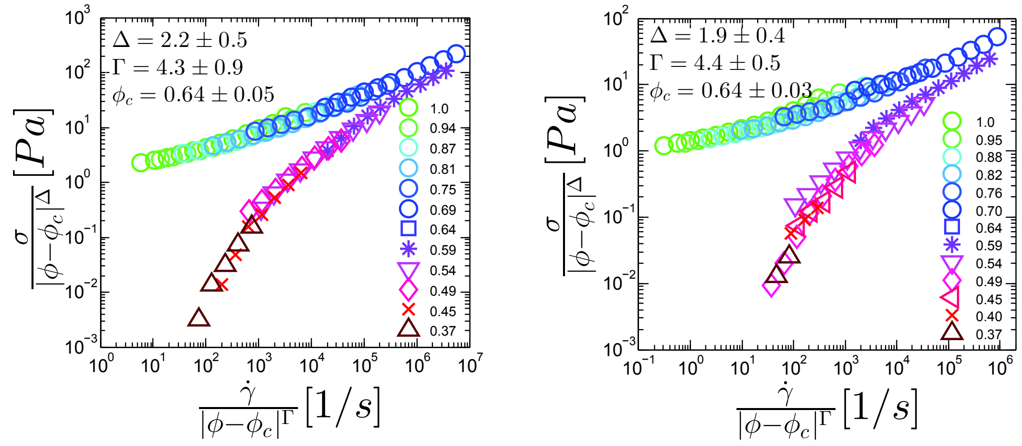

(a) Monodisperse

(b) Bidisperse

Figure 7.7: Volume-fraction-difference scaled σ vs. $\dot{\gamma}$ for aqueous suspensions of (a) monodisperse (diameter, ~700 nm), and (b) bidisperse (diameters, ~500 nm, ~700 nm) NIPA microgel spheres. Volume-fraction difference, $|\phi - \phi_c|$ is calculated from $\frac{|T-T_c|}{T_c}$, using DLS data on the thermal response of NIPA spheres. The best-fit values of Δ, Γ and ϕ_c are 2.2, 4.3, 0.64 for monodisperse NIPA suspensions, and 1.9, 4.4, 0.64 for bidisperse NIPA suspensions.

We find that the values of $\beta \equiv \Delta/\Gamma \sim 0.5$ obtained using the χ^2-minimization method are consistent with the Herschel-Bulkley fitting exponent, $n \approx 0.5$, obtained from fitting the rheology data of all jammed NIPA suspensions (Fig. 7.4). This result is also consistent with previous simulation [113] and micro-fluidic experiment [107]. A new result is that the critical scaling exponents, Δ, obtained from yield-stress scaling in monodisperse and *bidisperse* systems are in agreement (within the error bars) with the Δ values obtained from the χ^2-minimization method and reported previously for monodisperse systems [107]. Scaling arguments predict that $\Delta = a - 1/2$ [141, 107], where $a = 2$ (harmonic) and $a = 5/2$ (Hertzian). Because NIPA interactions have been reasonably well-approximated by both harmonic and Hertzian interactions in previous studies [17], we can expect Δ to range anywhere between $3/2$ and 2. Indeed, $\Delta \approx 2$ for both monodisperse and bidisperse NIPA systems is in agreement with the scaling predictions for Hertzian particles.

The values of the critical exponent ($\Gamma \approx 4$) obtained from the χ^2 minimization method, however, appear to be systematically larger and more consistent with the exponents reported in [107, 70] than those obtained from Herschel-Bulkley fittings. This discrepancy in Γ values could have its origin in the shear history of the fluid micro-structure [105, 99]. The advantages of using the χ^2-minimization method are in that this method helps us avoid fitting the data to any particular model, and data from both jammed and unjammed branches are utilized for the determination of scaling parameters, Δ, Γ and T_c.

The critical exponents for the monodisperse and the bidisperse NIPA systems are approximately the same (within error bars). This result is consistent with a prediction by O'Hern, *et al.* [110, 111] that critical scaling exponents should not depend on whether the jammed system is monodisperse or bidisperse; rather these parameters should depend primarily on the interaction potentials of the particles in suspension, which are similar in the monodisperse and bidisperse systems.

Shear stresses and strain rates measured for the aqueous suspensions of NIPA microspheres can also be redefined in terms of natural parameters in the problem. In APPENDIX D.3, for example, we follow the procedure of Nordstrom, *et al.* [107] to make stress and strain-rate unitless via $\frac{\sigma}{E}$ and $\frac{\dot{\gamma}.\eta_{water}}{E}$, where E is elastic modulus of NIPA microspheres and η_{water} is the viscosity of the background medium. To carry out this procedure, however, we had to make a number of assumptions, e.g., that the different microgel particles used in different experiments have the same functional forms for temperature-dependence of elastic modulus, etc. Nevertheless, critical scaling is still observed (see Appendix D.3) with exponents (reported in Tables 8.3, 8.4) ranging within 10% to 30% of what is obtained from the procedures described above.

7.2.2 Frequency-dependent Rheology

A significant advantage of using a commercial rheometer for the investigation of jammed colloidal systems is the ease with which one can probe their frequency-dependent responses. The frequency response provides information about time-scales associated with dynamic arrest in the vicinity of the jamming transition. We measure the storage (G') and loss (G'') moduli of the monodisperse and bidisperse NIPA systems as a function of oscillation frequency, ω, across the jamming transition. As before, the temperature of these jammed systems are systematically varied to change volume fractions, ϕ; thus we obtain G' and G'' as a function of ϕ and ω. Fig. 7.8 shows the storage (G') and loss (G'') moduli of jammed (a) monodisperse ($\sim$700 nm diameter), and (b) bidisperse ($\sim$500 nm, $\sim$700 nm diameters) NIPA systems as function of ω, and for a range of $\phi > 0.64$. The maximum applied strain amplitude $\gamma \leq 0.02$, wherein the response to oscillatory shear is strictly linear, and all measurements are restricted to the laminar flow regime (i.e., $Re < 0.1$).

We test the scaling predictions for the static shear modulus, $G_0 \equiv \{G^*\}_{\omega\to 0}$ from simulations by O'Hern, *et al.* [110, 111]. G_0 may be extracted from fitting the frequency dependent data to the following functional form [39, 88]:

$$G^* = G_0 \left(1 + \sqrt{i\omega/\omega_n}\right), \tag{7.5}$$

where $G^* = G' + iG''$; static shear modulus, $\{G^*\}_{\omega\to 0} \equiv G_0$ and characteristic frequency, ω_n are the fitting parameters. Using the identity, $\sqrt{i} = (1+i)/\sqrt{2}$, Eq. 7.5 can be rewritten in terms

Scaling exponents for σ vs. $\dot{\gamma}$ using χ^2-minimization

(a) with $|T - T_c|/T_c$ as a scaling parameter:

Sample	Δ	Γ	$\beta = \Delta/\Gamma$	$T_c[K]$	ϕ_c
monodisperse	2.2±0.5	4.3±0.9	0.51±0.26	295±1	0.64±0.05
bidisperse	1.9±0.4	4.4±0.5	0.43±0.10	297±0.5	0.64±0.03

(b) with $|\phi - \phi_c|$ as a scaling parameter:

Sample	Δ	Γ	$\beta = \Delta/\Gamma$	ϕ_c
monodisperse	2.3±0.5	4.7±0.9	0.49±0.14	0.64±0.046
bidisperse	2±0.2	4.9±0.2	0.41±0.04	0.64±0.005

Table 7.2: Summary of critical scaling exponents for viscometry shear data using (a) $|T - T_c|/T_c$ and (b) $|\phi - \phi_c|$ as scaling parameters, respectively. Note that the critical scaling exponents extracted using either $|T - T_c|/T_c$ or $|\phi - \phi_c|$ are roughly same.

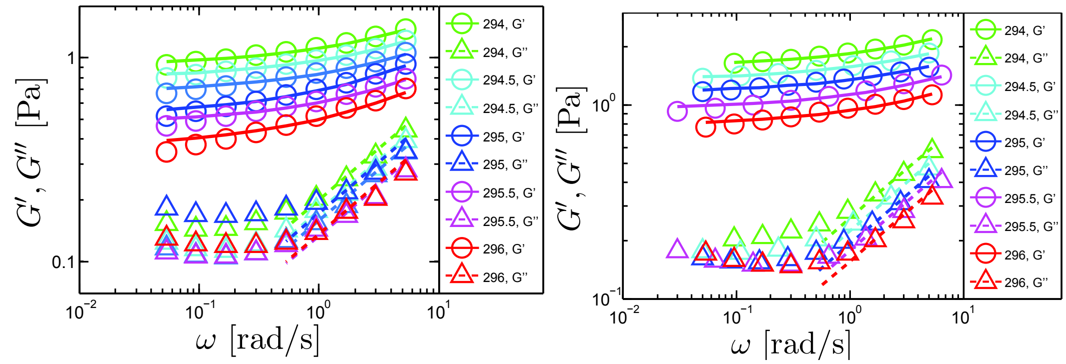

(a) Monodisperse

(b) Bidisperse

Figure 7.8: G' and G'' as a function of oscillatory frequency, for aqueous suspensions of (a) monodisperse NIPA microgel spheres (diameter, ~700 nm), and (b) bidisperse NIPA spheres (diameters, ~500 nm, ~700 nm), obtained using traditional rheology with maximum strain amplitude of $\gamma = 0.01$. Each curve is taken at a different temperature corresponding to a different volume fraction. Temperature is varied from 291.5 K to 294 K in steps of 0.5 K for (a) the monodisperse system, and from 294 K to 296 K for the (b) bidisperse case, again in steps of 0.5 K. The data are fit to $G' = G_0\left(1 + \sqrt{\frac{\omega}{2\omega_n}}\right)$ (solid lines), and $G'' = G_0\left(\sqrt{\frac{\omega}{2\omega_n}}\right)$ (dashed lines), where G_0, and ω_n are fitting parameters.

of G' and G'' as follows:

$$G' + iG'' = G_0 \left(1 + \sqrt{\frac{\omega}{2\omega_n}}\right) + iG_0 \left(\sqrt{\frac{\omega}{2\omega_n}}\right).$$

Equating the real and imaginary parts, we get

$$G' = G_0 \left(1 + \sqrt{\frac{\omega}{2\omega_n}}\right), \text{ and } G'' = G_0 \sqrt{\frac{\omega}{2\omega_n}}. \tag{7.6}$$

These fits are shown in Fig. 7.8, where the solid lines indicate G' fits and the dashed lines indicate the fits to G''. The quality of G' fits is quite good for both monodisperse and bidisperse datasets, whereas G'' can be well-approximated by the equation above only for $\omega > 0.4$ rad/s. The upturn in G'' for $\omega < 0.4$ rad/s, indicative of relaxation mechanisms [96, 79, 100], is not captured well by the fitting form used here. Static shear modulus, G_0 extracted from the G', G'' vs. ω fits at different volume fractions are plotted in Fig. 7.9 as function of the "distance" from the jamming volume fraction, $|\phi - \phi_c|$; error bars in G_0 indicate 95% confidence bounds associated with the fits.

O'Hern, *et al.* [110, 111] predict that G_0 of systems above the jamming transition scale with $|\phi - \phi_c|$, according to following relation: $G_0 \propto |\phi - \phi_c|^{\alpha}$, where $\alpha = 1/2$ for particles with harmonic interaction potentials, and $\alpha = 1$ for particles with Hertzian interactions. (Note: More generally, $\alpha = a - 3/2$, where a is the power-law exponent in the particle interaction potential defined earlier [149, 107].) This result was shown to hold for both monodisperse and bidisperse systems, in 2D as well as 3D. We experimentally confirm this behavior using G_0 extracted from macro-rheology data, as shown in Fig. 7.9. We find that $\alpha = 0.7 \pm 0.05 \pm 0.2$

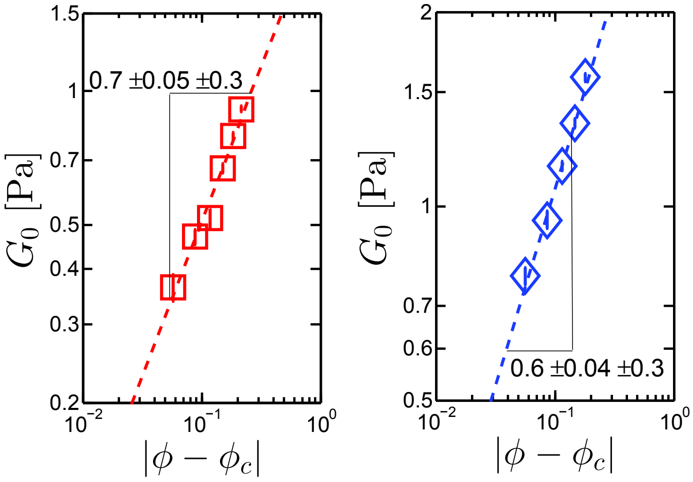

(a) Monodisperse (b) Bidisperse

Figure 7.9: Static shear modulus, G_0, extracted from macro-rheology data vs. $|\phi - \phi_c|$ for aqueous suspensions of (a) monodisperse NIPA microgel spheres (diameter, ~700 nm), and (b) bidisperse NIPA particles (diameters, ~500 nm, ~700 nm). The slopes are 0.7 ± 0.05 (fitting error) $\pm\, 0.2$ (systematic error) for monodisperse (a), and 0.6 ± 0.04 (fitting error) $\pm\, 0.2$ (systematic error) for bidisperse (b) samples, respectively. Overall, the slopes for monodisperse (a), and bidisperse (b) samples can be conservatively estimated as 0.7 ± 0.3.

for monodisperse NIPA microgel systems, where $\pm\, 0.05$ is the fitting error, and $\pm\, 0.2$ is the systematic error [165] for calculating G_0 at different packing fractions. To be conservative, we estimate our systematic error to be 50% greater that what we calculate, i.e., $\pm\, 0.3$. Similarly, we estimate $\alpha = 0.6 \pm 0.04$ (fitting error) $\pm\, 0.3$ (systematic error) for bidisperse NIPA microgel systems. Overall, $\alpha \approx 0.7 \pm 0.3$ for both monodisperse and bidisperse NIPA systems suggest that inter-particle interactions in these systems may be well-approximated by either harmonic or Hertzian potentials [17]. (A quasi-static shear modulus measured at $\omega = 0.1$ rad/s and $\gamma = 0.01$ also exhibit similar scaling relationship as G_0; in this case, we find that $\alpha = 0.7 \pm 0.2$ for monodisperse and $\alpha = 0.6 \pm 0.2$ for bidisperse NIPA microgel systems.) We also note that $\omega_n \approx 10$ rad/s for both systems and decreases as the jamming transition is approached.

Recent calculations by Tighe [142] predict critical scaling behavior of G' and G'' as a function of ω, for the jammed systems. Specifically, for a weakly polydisperse 2D system of disks with harmonic interactions, a scaling collapse of G' and G'' vs. ω is predicted when the moduli are scaled by $|Z - Z_c|^{2\alpha}$, and ω is scaled by $|Z - Z_c|^2$. Here, α as seen before, depends on the inter-particle interactions ($\alpha = 1/2$ for harmonic systems and 1 for Hertzian systems); Z is the coordination number of the interacting disks, and Z_c is the "critical" co-ordination number at the jamming transition.

We experimentally explore scaling collapse of the oscillatory data using the jammed NIPA systems, albeit with $|T - T_c|/T_c$ as the scaling factor, since $|Z - Z_c|$ cannot be measured directly in our experiment. To convert to temperature, we rely upon the relation, $|Z - Z_c| = |\phi - \phi_c|^{1/2}$; this relation was experimentally shown to hold near jamming in 2D foams [26], and was later extended to both harmonic and Hertzian systems, in both 2D and 3D [110], using simulations. Combining this relationship between coordination number and volume fraction near the jamming point with the thermo-sensitive nature of NIPA volume fraction, we expect $|Z - Z_c| = |\phi - \phi_c|^{1/2} \approx (|T - T_c|/T_c)^{1/2}$ (recall that $|\phi - \phi_c|$ is approximately linear in $|T - T_c|/T_c$ for aqueous NIPA suspensions close to the jamming transition, as shown in the inset in Fig. 7.3). As before, the relationships between T and ϕ given in Eq. 7.3, 7.4, and the assumption, $\phi_c = 0.64$, are used to convert between $|T - T_c|/T_c$ and the corresponding $|\phi - \phi_c|$.

Fig. 7.10 shows the scaling collapse of G' and G'', both rescaled by $|\phi - \phi_c|^\alpha$, vs. ω scaled by $|\phi - \phi_c|$, for the (a) monodisperse and (b) bidisperse NIPA systems. As noted above, simulations [110, 111] have predicted scaling of the quasi-static shear modulus, G_0 with $|\phi - \phi_c|^\alpha$ for jammed systems with repulsive interactions, and we have found a similar scaling of G_0 as function of $|\phi - \phi_c|^\alpha$ for $\alpha \approx 0.7$ for both monodisperse and bidisperse NIPA suspensions in Fig. 7.9. Through the scaling collapses in Fig. 7.10, we confirm Tighe's [142] prediction that the scaling of $G = G' + iG''$ with $|\phi - \phi_c|$ holds, not just for the quasi-static limit, but for a broad range of frequencies. Physically, as the jammed system approaches the unjamming transition, relaxation timescales are expected to progressively decrease, and a frequency corresponding to the inverse of such a time-scale should increase on approach to jamming. Consistent with these ideas, our oscillatory shear data exhibit scaling collapse on the jammed side when ω is rescaled by $|\phi - \phi_c|$.

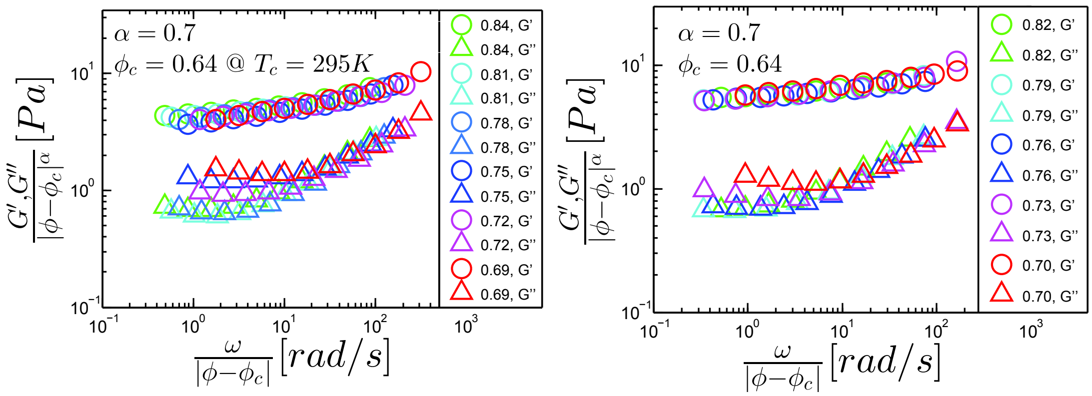

(a) Monodisperse (b) Bidisperse

Figure 7.10: Volume-fraction-difference-scaled G' and G'' as function of oscillatory frequency, for (a) monodisperse NIPA microgel spheres (diameter, ∼700 nm; ϕ= 0.84, 0.81, 0.78, 0.75, 0.72, 0.69), and (b) bidisperse NIPA microgel spheres (diameters, ∼500 nm, ∼700 nm; ϕ= 0.82, 0.79, 0.76, 0.73, 0.70), obtained using traditional shear rheology. The scaling exponent for G' and G'' is 0.7 for monodisperse and bidisperse NIPA suspensions. $\phi_c = 0.64$ in both systems.

The best-fit rescaling factors for G' and G'' were found by systematically varying the exponent α between $1/2$ (Harmonic), and 1 (Hertzian). Note that interactions of NIPA microgel spheres have been fit equally well (within signal-to-noise) by both Harmonic and Hertzian potentials [17]. We find that $\alpha = 0.7$ gives the best scaling collapse for both monodisperse and bidisperse systems, as shown in Fig. 7.10. The critical jamming temperature, T_c used in these rescalings are the same as those extracted from the viscometry scaling data, via χ^2-minimization. The observed data collapse of G' and G'' data onto two master curves are of reasonably good quality for both monodisperse and bidisperse NIPA systems.

In APPENDIX D.3, we also explore the critical scaling behavior of G' and G'' vs. ω, with all parameters rendered dimensionless, *viz.*, $\frac{G'}{E}$, $\frac{G''}{E}$ vs. $\frac{\omega . \eta_{water}}{E}$. The critical scaling exponents for dimensionless data are listed in Tables 8.3, 8.4 and the scaling are shown in Fig. 8.9.

Finally, we measure the cross-over frequency ($\omega^{\times}$) in *unjammed* systems, wherein G' equals G''. The corresponding relaxation time, $\tau^{\times} = 1/\omega^{\times}$ indicates the characteristic relaxation time of the system [79]. Fig. 7.11 plots the $\omega^{\times}$ vs. ϕ for the bidisperse NIPA system (diameters, ~500 nm, ~700 nm); G', G'' vs. ω data for the same system are shown in APPENDIX D.4. $\omega^{\times}$ and $\tau^{\times}$ can be fitted well by exponential functions, as indicated by the black dashed lines in the main figure and the inset. At $\phi = 0.63$, for example, $\omega^{\times} \approx 0.004$ Hz, which translates to $\tau^{\times} \approx 250$ seconds. Interestingly, this time-scale is of the same order of magnitude as the α-relaxation time measured at the jamming transition for a 2D NIPA system [163]. Note that cross-over frequencies measured in the monodisperse NIPA system had similar values (data not shown), albeit for the more limited range of ϕ investigated.fif:contour3D

In total, the frequency-dependent data may be summarized as follows. A series of experiments demonstrate critical scaling behavior in the frequency-dependent shear of monodisperse and bidisperse jammed NIPA systems. We confirm scaling predictions for static shear modulus [110, 111]: $G_0 \approx |\phi - \phi_c|^{\alpha}$. Exponents ($\alpha$) of 0.7 ± 0.3 were derived for both monodisperse and bidisperse NIPA systems 7.9. We also observe a more general scaling collapse in G' and

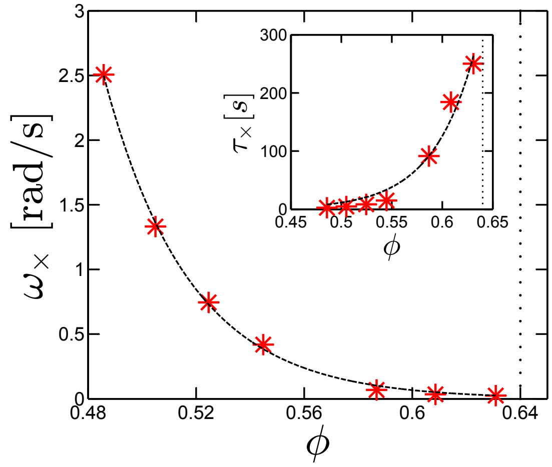

Figure 7.11: $\omega^\times$ (G' and G'' cross-over frequency) vs. packing fraction for aqueous suspensions of bidisperse NIPA microgel spheres (diameters, ~500 nm, ~700 nm). The inset plots the corresponding $\tau^\times$ as a function of ϕ. In both the main figure and inset, dashed black lines indicate exponential fits. Dotted lines mark the jamming transition.

G'' vs. ω when the variables were appropriately scaled by the "distance" from jamming transition. All the results are consistent for both monodisperse and bidisperse NIPA systems, as predicted [111]. Finally, for unjammed NIPA systems close to the jamming transition, we show that the G'-G'' cross-over frequency, $\omega^\times$ decreases as the jamming transition is approached. This observation indicates the presence of a relaxation time-scale, $\tau^\times = 1/\omega^\times$ that increases with proximity to the jamming transition.

7.3 Conclusions

In summary, we investigate both steady-state and frequency-dependent flow behavior of jammed colloidal systems using macro-rheology. We study two systems using shear rheology *viz.*, monodisperse and bidisperse soft colloidal suspensions. We find that shear stress and strain rate data from steady-state rheology experiments can be collapsed onto two distinct branches using scaling exponents, $\Delta \approx 2$ and $\Gamma \approx 4$. These results are consistent with experiments employing a micro-fluidic setup [107] and with simulation [113, 141, 42]. We also report experimental results from frequency-dependent shear in the jammed systems and demonstrate critical scaling of shear storage and loss moduli as functions of oscillating frequency with scaling exponent, $\alpha \approx 0.7$, consistent with theoretical predictions [110, 142]. The stress relaxation time-scale in unjammed systems is shown to grow exponentially as the jamming transition is approached. We note that all scaling behavior and critical exponents are similar within error bars, for monodisperse and bidisperse NIPA systems.

Chapter 8

Conclusions and Future Work

8.1 Summary of Main Results

Microscopy and rheology measurements under shear in model flexible polymer gels, *viz.*, polyacrylamide (PA) gels in Chapter 4 indicate that, for a wide range of applied strain, γ, the shear modulus remains independent of strain and the mean square non-affine deviation, $\mathcal{A}$ in the gels is proportional to the square of the strain applied. These results support the theoretical prediction [23] that in an isotropic, linear elastic medium, $\mathcal{A}$ scales as γ^2 as long as the shear modulus remains independent of γ. Interestingly, the magnitude of $\mathcal{A}$ is greater than what one would expect from theoretical calculations assuming that the PA gels are nearly-ideal in which the only source of non-affinity is thermal fluctuations. We posit that there are additional sources of non-affinity in PA gels that lead to the large non-affinity measures. Indeed, there is ample evidence of built-in inhomogeneities in PA gels due to a difference in the hydrophobicities of the bisacrylamide crosslinks and acrylamide monomers. Combining the inhomogeneity lengthscale estimated from Atomic Force Microscopy measurements ($\xi_G \sim 200$ nm) with non-affinity measurements ($\frac{\mathcal{A}}{\gamma^2} \lesssim 2\ \mu m^2$), the magnitude of local variations in elastic modulus, $\frac{\delta G'}{G'}$ is calculated to be ≈ 7. We note that the degree of non-affinity appears to be independent of polymer chain density and cross-link concentration, but is weakly dependent on reaction kinetics and the size of non-affinity probe particles. Our measurements of non-affinity in PA gels, which are model flexible polymer gels, provide a benchmark for the degree of non-affinity in soft materials, and serve as a comparison for non-affinity in more complicated materials such as semi-flexible bio-polymer gels.

Chapter 5 compares macroscopic elasticity and non-affinity in different types of flexible and semi-flexible polymer gels as a function of shear strain. The nonlinear viscoelastic response of semi-flexible polymer gels at moderate strain coincides with very low magnitudes of non-affinity measures. The deviation from affine deformation for isotropic fibrin gels is significantly different from zero, but less than 0.1 at small strains, and it decreases significantly at higher strains, as the shear modulus increases. Relatively high $\mathcal{S}$ values at low strains could indicate that applied external stress can induce structural reorganization of the network, also providing an explanation to the non-linear elasticity [115]. Low $\mathcal{S}$ value at moderate strain values suggests that the assumption of affine deformation is approximately applicable for the strains where strain-stiffening is observed, and supports the use of entropic theories to account for this phenomenon [138].

Chapter 6 concentrates exclusively on two of the semi-flexible polymer gels studied in the previous chapter, *viz.*, fibrin and collagen gels. We measure macroscopic elastic behavior and microscopic non-affine deviation in these gels under shear. Macroscopic elasticity in semi-flexible gels differs markedly from rubber elasticity in that it shows significant non-linear elasticity in the form of strain-stiffening, and negative normal stress. The rate at which a sample exhibits strain-stiffening and normal stress as a function of strain increases with increasing polymer concentration. We note that all macroscopic elasticity behavior can be explained by the entropic model of elasticity proposed by Storm, *et al.* [138].

Non-affinity measures, in general, are much larger in semi-flexible polymer networks than in flexible PA gels [8]. We note that $\frac{\mathcal{A}}{\gamma^2}$ decreases with increasing shear strain. This behavior is expected when network deformation transitions from filament bending to affine stretching of polymer chains under increasing strains; this decrease in non-affinity is also accompanied by non-linear strain stiffening behavior [115, 84, 85, 12], as seen from rheology measurements. Unlike in flexible PA gels, non-affinity measures depend on polymer concentrations- the higher the polymer concentration, the lower the non-affinity. Also, gels with stiffer polymer filaments exhibit higher non-affinity. Both of these results can be accounted for by simulations done by Head, *et al.* [84, 47].

8.2 Future Directions

Why measure non-affinity? Well, numbers are always handy to characterize material. For example, there is increasing interest and effort in using polymers for soft lithography for cell locomotion, simulating Extra Cellular Matrix (ECM), and even in fabricating phononic materials. The assumption that goes in, is that these soft materials are homogeneous at sub-micron length-scales. Our non-affine measurements, especially on PA gels have shown that such an assumption for PA gels may not be reasonable below certain length-scales.

When we started measuring non-affinity in polymer gels, we were not fully aware of the effect of inhomogeneity on non-affinity in macroscopically homogeneous gels like PA and fibrin. The thought was that non-affinity would provide an extra parameter to study the mechanism by which semi-flexible gels deform under shear. From theoretical and numerical works, it is posited that non-affinity in polymer gels arise from 1) enthalpic bending/buckling of individual semi-flexible polymer segments, or 2) network rearrangements of physically cross-linked gels under shear, both of which can be reversible, up to certain strains. If these are the only two contributing factors to non-affinity, then PA gels, which consist of chemically cross-linked flexible polymer chains, should be completely affine under shear. Indeed, PA gels were studied as a control system, the results of which we could compare against that of semi-flexible gels. Our experiments show that is clearly not the case- there is indeed another source of non-affinity, viz., inhomogeneities. If we are to continue to use non-affinity as a quantitative measure of bending vs. stretching mechanisms, then we will need to decouple the contribution of inhomogeneities in the non-affinity measures from that of entropic/enthalpic deformation mechanisms. We propose that this can be done in two ways: 1) use a model system which is indeed homogeneous in the microscopic length-scales (this is hard- inhomogeneities can be ridiculously hard to get rid off; even if there is a homogeneous concentration of polymer ingredients, i.e., monomer, crosslink, and catalyst to start with, inevitable random thermal fluctuations of the ingredients during the polymerization will get quenched in as the gel polymerizes; soft lithography or microfluidic techniques may be useful to bypass these issues), or 2) define a local order parameter and be able to quantify and then subtract out the non-affinity that may arise from the anisotropy of the gel (this is hard too- one cannot then, simply track displacement of embedded tracer-beads under external loads any longer- this will require a more involved process of visualizing the polymer network itself, to calculate the local order parameter). Non-affinity may also be a function of time, especially for gels with relatively high G''. Currently, experiments can probe the non-affinity in a quasi-static limit. Future experiments may be able to tackle time-dependence non-affinity experiments.

8.2.1 Non-affinity in Active Gels

Active gels comprise a class of semi-flexible bio-polymer gels in which the mechanics are governed by molecular motors that consume energy usually through adenosine triphosphate (ATP) consumption, and generate contractile forces on the polymer filaments comprising the gel. Active gels can mimic the dynamic environment of *in vivo* cytoskeletal structure. Active gels exhibit dramatic strain-stiffening behavior [104]. Recent simulations [12] predict that the contractile forces generated by motors in active gels can pull out and exhaust the bending modes in the semi-flexible filaments, thus causing the network deformation mechanism to transition into a stretching-dominated one. This theory can be easily tested by using non-affinity measurements- if this were indeed the case, one can posit network behavior in *in vitro* reconstituted active gels to be more affine than their passive counterparts.

8.3 Rheology and Jamming

In the last chapter 7, we investigate both steady-state and frequency-dependent flow behavior of jammed colloidal systems using macro-rheology. We study two systems using shear rheology *viz.*, monodisperse and bidisperse soft colloidal micro-spheres. We find that the scaling exponents from steady-state rheology experiments are consistent with experiments employing a micro-fluidic setup and an alternate Herschel-Bulkley fitting scheme [107] and with simulation [113, 141, 42]. We also report experimental results from frequency-dependent shear in the jammed systems and demonstrate critical scaling of oscillatory data, consistent with theoretical predictions [110, 142]. The stress relaxation time-scale in unjammed systems is shown to grow exponentially as the jamming transition is approached. We note that all scaling behavior and critical exponents are similar (within error bars) for monodisperse and bidisperse NIPA systems.

We propose that thermo-sensitive NIPA systems together with commercially available rheometers can provide easily accessible experimental systems to study the jamming phenomenon as a function of shear in 3D soft colloidal glasses. The experiments reported in this thesis concern solely with systems with repsulsive interactions- it will be interesting to compare the current results with thermo-responsive NIPA microspheres with (a) uneven surfaces to investigate the effect of friction on jamming along the shear axis, or (b) attractive interactions. There has been several papers over the years that report rheological response of soft colloidal glasses (SGR), both oscillatory and viscometry using the techniques in this chapter; we simply use these techniques to investigate the broader field of jamming.

Appendix

A Appendix to *Chapter 4: Shear Deformation in Flexible Polymer Gels*

A.1 Ensemble Averaged $\frac{\mathcal{A}}{\gamma^2}$ Values for PA Gel Samples

Fig. 8.1(a) plots the ensemble average of the strain-normalized non-affinity parameter, $\frac{\mathcal{A}}{\gamma^2}$ for different PA gel samples at various monomer (*viz.,* 7.5% and 15% acrylamide, w/v), and cross-link (between 0.005% and 0.12% bisacrylamide, w/v) concentrations. Because different PA gel samples have different number of tracer beads dispersed in them, this alternative approach is pursued where every tracer bead across different samples is weighed equally. In this method, the mean-square non-affine displacement collected from various samples at a given acrylamide and bis concentration is plotted against the mean square fitted strain, where all the fitted strain values are very close to the externally applied strains. The linear fit of the mean square non-affine displacements versus the mean square fitted strains, for different externally applied strains, gives the ensemble averaged $\frac{\mathcal{A}}{\gamma^2}$, as shown in Eq. (8.1). Error bars in the figure reflect the error in the linear fits. Note that the strain-normalized non-affinity parameters obtained from this method are very similar to that shown in Fig. 4.4(b), and confirm the robustness of our results.

$$\mathcal{A} = \frac{1}{\sum_i N_i} \sum_{i=1}^{m} \sum_{j=1}^{N_j} |\vec{u}_{ij}|^2,$$

$$\gamma^2 = \frac{1}{m} \sum_{i=1}^{m} \gamma_i^2. \tag{8.1}$$

Here $i = 1, 2, \ldots, m$ labels the PA gel samples at a given acrylamide and bis concentration, with the i-th sample contains N_i beads labeled by $j = 1, 2, \ldots, N_i$.

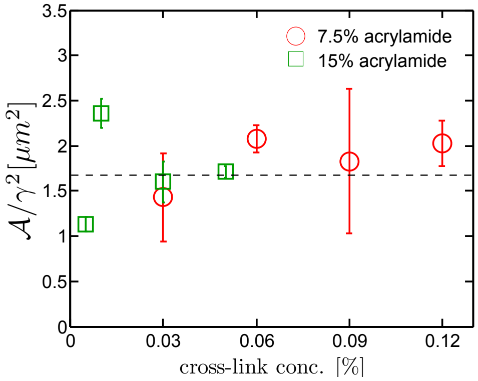

(a)

Figure 8.1: (a) $\frac{\mathcal{A}}{\gamma^2}$ for sample PA gels at 7.5% and 15% acrylamide are plotted at varying bis concentrations. The data points represent the ensemble-averaged values of measurements from several different samples prepared, ostensibly, in the same manner. Error bars reflect the fitting error in calculating ensemble-averaged $\frac{\mathcal{A}}{\gamma^2}$. The dashed line in the main figure indicates the mean of all $\frac{\mathcal{A}}{\gamma^2}$ values listed in Table 8.1.

$\frac{\mathcal{A}}{\gamma^2}$ calculated from individual samples at various acrylamide and bis concentrations are listed in Table 8.1, along with their respective error estimates.

Sample#	acrylamide conc.[%]	bis conc.[%]	$\frac{A}{\gamma^2}$ $[\mu m^2]$	Error $[\mu m^2]$
1	7.5	0.03	1.18	± 0.08
2	7.5	0.03	1.92	± 0.96
3	7.5	0.06	2.08	± 0.15
4	7.5	0.06	0.61	± 0.28
5	7.5	0.09	1.15	± 0.58
6	7.5	0.09	2.03	± 0.94
7	7.5	0.12	1.69	± 0.50
8	7.5	0.12	2.72	± 0.25
9	7.5	0.12	1.50	± 0.41
10	15	0.005	1.13	± 0.08
11	15	0.01	2.36	± 0.16
12	15	0.03	1.60	± 0.23
13	15	0.05	1.71	± 0.07

Table 8.1: List of $\frac{A}{\gamma^2}$ values for different PA gel samples. Error estimates reflect the uncertainty in the linear fits from which $\frac{A}{\gamma^2}$ are obtained.

A.2 Effect of Polymer Chain Concentration

Though we have only investigated the effect of crosslinks on the elasticity of flexible polymer gels, there may be added contributions to elasticity from other factors like solvent quality, and polymer chain entanglements. This section briefly looks at the effect of polymer concentration on gel elasticity using PA gels with different acrylamide (polymer) concentration.

Fig. 8.2(a) displays G' as function of bis (crosslink) for PA gels with 7.5%, 12%, 16% and 20% acrylamide, respectively. We note that the greater the acrylamide concentration, the greater is the efficacy of crosslinks, i.e., greater is the slope of G' vs. bis concentration. This may be explained as follows: the higher the acrylamide concentration, greater is the probability of a bis unit to successfully crosslink to polymer chain, forming an effective crosslink junction that can contribute to the gel elasticity.

Fig. 8.2(b) looks at shear elasticity in PA gels with different acrylamide concentrations, in

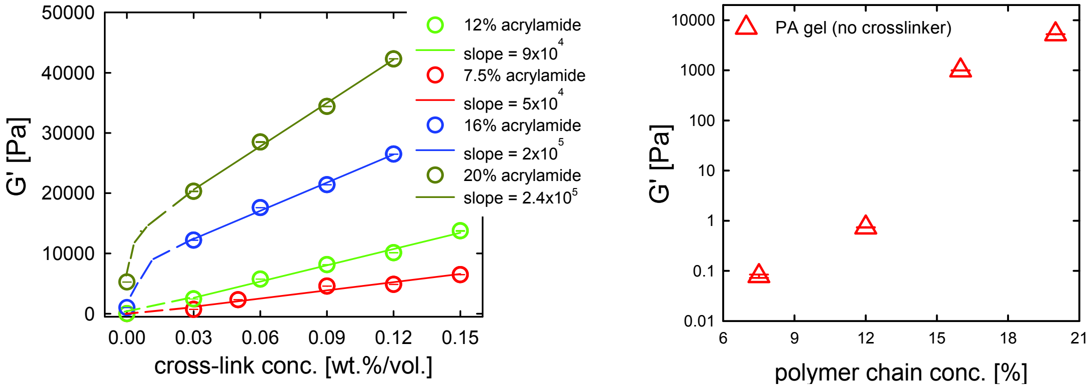

(a) (b)

Figure 8.2: (a) G' vs. crosslink concentration for PA gels with 7.5%, 12%, 16% and 20% acrylamide, respectively. (b) G' vs. polymer chain concentration in the absence of bis crosslinks.

the *absence* of any additional crosslinks (i.e., bis). We note that at sufficiently high polymer concentrations (beyond the critical overlap concentration) of acrylamide, there is a non-zero G' from polymer chain entanglements alone; this G' increases with increasing polymer concentration.

B Appendix to *Chapter 5: Non-Affinity in Gels of Different Polymer Classes*

Fig. 8.3 plots the elastic moduli, G' of the different types of polymer gels discussed in Chapter 5 as function of applied strain, γ. Gels consisting of different polymer concentrations are displayed.

Similarly, Figs. 8.3(a),(b) shows the dimensionless non-affinity parameters, $\mathcal{S}$ and $d\mathcal{S}$ vs. γ for the same set of polymer gels shown in Fig. 8.3.

The conclusions that were made in Chapter 5 are borne out in these plots: (a) chemically crosslinked bio-polymer gels show significant increases in G' with increasing γ, (b) non-affinity

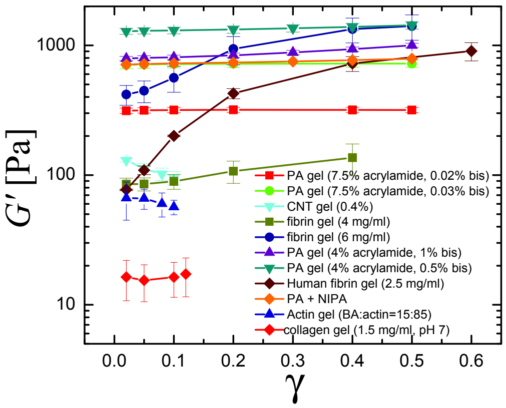

Figure 8.3: G' vs. γ for different polymer gels.

decreases with decreasing persistence length, l_p of the constituent polymer chains, and (c) non-affinity, decreases with increasing γ. Additionally, we see that as the polymer concentration for a particular gel is increased, G' *increases* while both $\mathcal{S}$ and $d\mathcal{S}$ *decreases*, meaning that gels tend to become stronger and more affine with increasing polymer concentration. We concentrate on two particular types of gels in Chapter 6 to investigate such roles as polymer concentration, etc. on macroscopic gel elasticity and non-affinity measures.

C Appendix to *Chapter 6: Shear Deformations in Semi-flexible Polymer Networks*

C.1 Fitting Scaled Shear Modulus vs. Scaled Strain data for fibrin and collagen gels to Entropic Theory

Strain-stiffening data from fibrin gels can be scaled to collapse on a master curve (Fig. 6.1(c)) when the shear modulus, G' is scaled by the zero-strain shear modulus, G'_0 (or $\gamma = 0.01$ in this

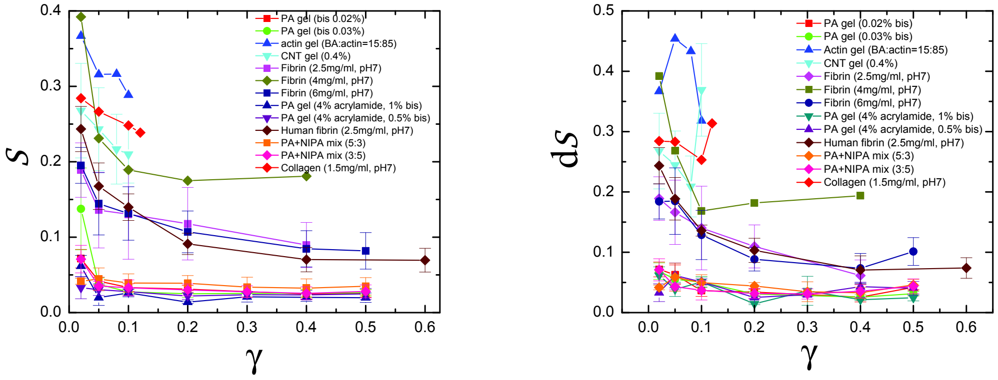

(a) (b)

Figure 8.4: (a) $\mathcal{S}$ vs. γ calculated from different polymer gels (same samples as shown in Fig. 8.3). (b) $d\mathcal{S}$ vs. γ for the same polymer gels samples as shown in Figs. 8.3, 8.4.

case), *viz.*, $\frac{G'}{G'_0}$. The strain is scaled by the strain value, $\gamma_{1.5}$ at which G' is an arbitrarily chosen multiple of G'_0, or, as in case of fibrin gels, $G' = 1.5G'_0$, *viz.*, $\frac{\gamma}{\gamma_{1.5}}$. This scaling collapse can be captured well by the dashed line in Fig. 6.1(c) indicating the fit to the entropic model for non-linear elasticity in semi-flexible polymer gels proposed by Storm, *et al.* [138]. According to this model, non-linear elasticity in semi-flexible polymer gels arise from the non-linear force-extension curve of a constituent polymer filament.

$$\delta\tilde{L} = \frac{L(f;L_c) - L(0;L_c)}{L_c^2/l_p} = \frac{1}{\pi^2}\sum_{n=1}^{\infty}\frac{\varphi}{n^2(n^2+\varphi)}$$

$$= \frac{3+\pi^2\phi - 3\pi\sqrt{\phi}\coth(\pi\sqrt{\phi})}{6\pi^2\phi} \tag{8.2}$$

where $L(0;L_c)$ is the unstretched length of a semi-flexible polymer, $L(f;L_c)$ is the stretched length of the same polymer under an applied force, f; L_c is the contour length, l_p is the persistence length, $\kappa = k_BTl_p$ is the bending stiffness, $\varphi = fL_c^2/(\kappa\pi^2)$ is the force term that can be rendered dimensionless by the scaling force, $\kappa\pi^2/L_c^2$, which is also the threshold force for the Euler buckling instability in thin cylinders.

We use this formula to derive the scaling for shear modulus using the entropic theory and affine deformation assumption,

$$\frac{G'}{G'_0} = g\left(\frac{\gamma}{\gamma_4}\right). \tag{8.3}$$

Because $\gamma \propto \delta\tilde{L}$, we can write

$$\frac{\gamma}{\gamma_4} = \frac{\delta\tilde{L}}{\delta\tilde{L}_4}. \tag{8.4}$$

Using $\sigma \propto \phi$, we can write shear modulus as

$$G' \equiv \frac{d\sigma}{d\gamma} \propto \frac{d\phi}{d\delta\tilde{L}} \tag{8.5}$$

Thus,

$$\frac{G'}{G'_0} = \frac{d\phi/d\delta\tilde{L}}{d\phi/d\delta\tilde{L}|_{\phi=0}}. \tag{8.6}$$

The above equation can be rewritten as

$$\frac{G'}{G'_0} = \frac{d\delta\tilde{L}/d\phi|_{\phi=0}}{d\delta\tilde{L}/d\phi}. \tag{8.7}$$

Using Eqn. 8.2, we get

$$d\delta\tilde{L}/d\phi = \frac{\pi\sqrt{\phi}\mathrm{coth}(\pi\sqrt{\phi}) + \pi^2\phi\mathrm{csch}^2(\pi\sqrt{\phi}) - 2}{4\pi^2\phi^2} \tag{8.8}$$

The value at $\phi = 0$ is

$$d\delta\tilde{L}/d\phi|_{\phi=0} = \frac{\pi^2}{90}. \tag{8.9}$$

$\delta\tilde{L}_4$ can be obtained from solving the following equation

$$\frac{G'}{G'_0} = \frac{d\delta\tilde{L}/d\phi|_{\phi=0}}{d\delta\tilde{L}/d\phi} = 4. \tag{8.10}$$

To plot the dashed line in Fig. 6.1(c), we use parametric plot with ϕ as the free parameter. For any given ϕ, the horizontal axis is

$$\frac{\gamma}{\gamma_4} = \frac{\delta\tilde{L}}{\delta\tilde{L}_4} \tag{8.11}$$

where $\delta\tilde{L}$ depends on ϕ through Eq. 8.2 and $\delta\tilde{L}_4$ is calculated from the value of ϕ_4 solved from Eq. 8.10. The vertical axis is obtained from

$$\frac{G'}{G'_0} = \frac{\pi^2/90}{d\delta\tilde{L}/d\phi}. \tag{8.12}$$

and using Eq. 8.8.

Solving numerically, The values at $G'/G'_0 = 4$ and $G'/G'_0 = 1.5$ are obtained as follows

$$\phi_4 = 3.50584, \tag{8.13}$$

$$\phi_{1.5} = 0.54417 \tag{8.14}$$

Accordingly we calculate $\delta\tilde{L}_4$ and $\delta\tilde{L}_{1.5}$ using above values and Eq. 8.2,

$$\delta\tilde{L}_4 = 0.0619434 \tag{8.15}$$

$$\delta\tilde{L}_{1.5} = 0.0217531. \tag{8.16}$$

C.2 Rate of Strain-stiffening in Semiflexible Polymer Gels Increases with Increasing Polymer Concentrations

We also note that the rate of strain-stiffening in both fibrin and collagen gels increases with increasing c. This phenomenon becomes more evident in Fig.8.5, where G' normalized by $\{G'\}_{\gamma\to 0} \equiv G'_0$ is plotted as function of γ for fibrin (a), and collagen (b), at different polymer concentrations.

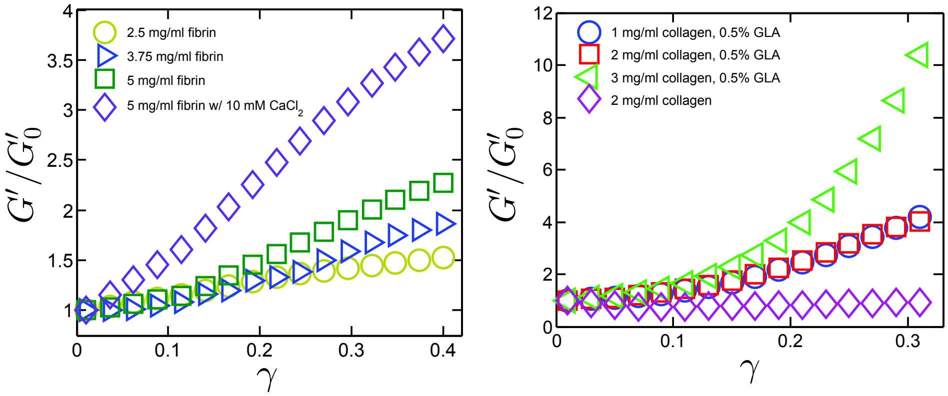

(a) (b)

Figure 8.5: Normalized storage moduli, $\frac{G'}{G'_0}$ vs. γ in (a) 2.5 mg/ml, 3.75 mg/ml, 5 mg/ml and 5 mg/ml (10mM Ca^{2+} ions) fibrin gels in tris buffer at pH = 7.4, and (b) 1 mg/ml, 2 mg/ml, 3 mg/ml collagen gels, each crosslinked with 0.5% GLA, and uncrosslinked 2 mg/ml collagen gel, all in 1× PBS buffer.

The stiffening in fibrin gels with increasing c can be written as $G'_0 \propto c^a$ where $a \approx 1.8 \pm$

0.21. A similar concentration dependence of G' has been witnessed in other types of semi-flexible polymer gels, e.g., F-actin gels [129, 93]. Unlike fibrin and F-actin gels, however, we obtain a different scaling relation between G'_0 and c in collagen gels: $a \approx 4.6 \pm 0.15$ for GLA cross-linked collagen gel, and $a \approx 0.55 \pm 0.01$ for collagen gel without any additional cross-linking agents.

C.3 List of Slopes for $log_{10}(\mathcal{A})$ vs. $log_{10}(\gamma)$ for different samples of fibrin and collagen gels.

Table 8.2 lists the dependence of $\mathcal{A}$ on γ, *viz.*, $A \propto \gamma^B$, where B is reported along with their respective error estimates. B is calculated from the linear fit to data on a log-log plot for individual samples polymerized under different experimental conditions.

D Appendix to *Chapter 7: Macro-rheology of Soft Colloids Near the Jamming Transition*

D.1 Checking for wall-slip effects using rheometer tools *with* and *without* surface roughening

A Bohlin Gemini rheometer (Malvern Instruments, UK), albeit with lower sensitivity (~5 mPa, compared to 0.1 μPa for the ARES-G2), was employed to check the effect of surface roughness and wall-slip, using steady-state viscometry measurements. The rheometer tools were roughened by sintering polystyrene micro-spheres, ~800 nm diameter (Seradyn Microparticle Technology, US), on the surfaces of the rheometer cone and plate. Steady-state measurements on

Salmon fibrin gel

Sample#	fibrinogen [mg/ml]	thrombin [NIH U/ml]	Ca^{2+}[mM]	B	Error
1	2.5	1.8	0	1.80	± 0.07
2	2.5	1.8	0	1.54	± 0.06
3	5	3.75	0	1.71	± 0.04
4	5	3.75	0	1.18	± 0.03
5	5	3.75	10	1.48	± 0.03
6	5	3.75	10	1.79	± 0.01

Collagen gel with GLA cross-links

Sample#	collagen [mg/ml]	GLA [mg/ml]	B	Error
7	1	0.5	1.45	± 0.03
8	1	0.5	1.51	± 0.10
9	1	0.5	1.55	± 0.01
10	2	0.5	1.93	± 0.07
11	2	0.5	1.99	± 0.08
12	3	0.5	2.20	± 0.11
13	3	0.5	0.84	± 0.18

Collagen gel

Sample#	collagen [mg/ml]	B	Error
14	2	1.91	± 0.03
15	2	1.84	± 0.06
16	4	1.66	± 0.01
17	4	1.98	± 0.08
18	6	2.62	± 0.14
19	6	2.39	± 0.03

Table 8.2: List of B values for different semi-flexible gel samples, where $\mathcal{A} \propto \gamma^B$. Error estimates reflect the uncertainty in the linear fits to $log_{10}(\mathcal{A})$ vs. $log_{10}(\gamma)$, from which B is obtained.

monodisperse NIPA suspensions were made for $\dot{\gamma} = 0.05 \rightarrow 5$ 1/s, at different volume fractions, $\phi \approx 0.9 \rightarrow 0.6$, roughly in steps of 0.05.

D.2 Scaling analysis using Herschel-Bulkley fitting

Following the fitting scheme [107], we fit the jammed data at each temperature using the Herschel-Bulkley (HB) model, $\sigma = \sigma_y + k\dot{\gamma}^n = \sigma_y \{1 + (\tau\dot{\gamma})^n\}$, where τ is a relaxation time-constant described by Nordstrom, *et al.* [107]. As shown in Fig. 7.4, n is in agreement with the HB

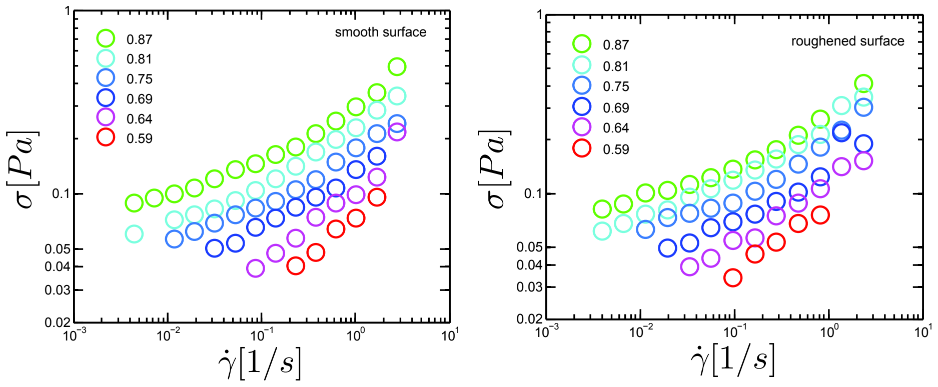

(a) (b)

Figure 8.6: σ vs. $\dot{\gamma}$ of monodisperse NIPA suspension (diameter, $\approx$700 nm) using Bohlin Gemini rheometer and 4^o, 40 mm cone-and-plate geometry (a) without, and (b) with the surfaces roughened.

exponent reported by Nordstrom, *et al.* [107].

Per scaling, we note that even though the viscometry data of the jammed samples can be fit reasonably well to the HB model, the HB fitting schemes used to derive scaling exponents in [107] proved more difficult to apply to our macro-rheology data. For example, the macro-rheology experiments were unable to approach the jamming transition as closely as the microfluidic experiments due to the limitations in temperature control when using the rheometer; thus we have fewer points very close to the jamming point, and by comparison to our χ^2 minimization method, we only use half of the available data. Nevertheless, we perform the HB analysis for completeness sake in this section, as follows.

We fix n at its mean value, and repeat the HB fits to obtain a new set of σ_y and k versus temperature. The timescale, τ, is derived from k such that $\tau = (\sigma_y/k)^n$. σ_y and τ are then fitted to power laws in $|T - T_c|$, where both exponent and critical temperature are adjusted. This gives two values of T_c, *viz.*, $(T_c)_{\sigma_y}$ and $(T_c)_k$, which are at most within a couple of degrees Kelvin of one another; our estimated critical temperature, T_c is obtained by averaging these two values, as $T_c = ((T_c)_{\sigma_y} + (T_c)_k)/2$. ϕ_c and ϕ are then calculated using Eqns. 7.3 and 7.4, as before. σ_y and τ values are then plotted as functions of $|\phi - \phi_c|$ on log-log plots, the slopes of which give us the exponents Δ and Γ, respectively. (Δ obtained from power-law fit for σ_y vs. $(\phi_c)_{\sigma_y}$ and Γ similarly from power law fit for τ vs. $(\phi_c)_k$ are in agreement with Δ and Γ obtained from using average ϕ_c, within error bars.) Fig. 8.7 plots n, σ_y and τ for the monodisperse (a, b, c) and bidisperse (d, e, f) NIPA suspensions respectively.

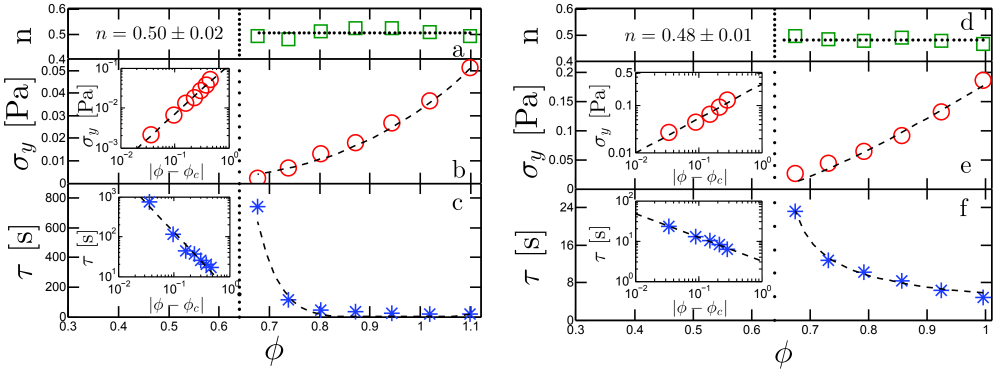

(a) Monodisperse

(b) Bidisperse

Figure 8.7: Scaling exponents Δ, Γ obtained from the HB fits to macro-rheology data for (a, b, c) monodisperse NIPA microgel suspensions (diameter, ~700 nm), and (d, e, f) bidisperse NIPA suspensions (diameters, ~500 nm, 700 nm). For the monodisperse and bidisperse systems, respectively, (a) and (d) plots the HB exponent, n as a function of ϕ, (b) and (e) plots σ_y Pa vs. ϕ (inset - σ_y Pa vs. $|\phi - \phi_c|$), and (c) and (f) plots τ s vs. ϕ (inset - τ s vs. $|\phi - \phi_c|$). Critical exponents calculated from HB scaling are (a) monodisperse: $\Delta = 1.3 \pm 0.23$, and $\Gamma = 1.6 \pm 0.43$; (b) bidisperse: $\Delta = 1.4 \pm 0.4$, and $\Gamma = 1.0 \pm 0.4$. Error bars include statistical and systematic errors from fits.

Δ and Γ thus calculated are as follows: 1.3 ± 0.03 (fitting error) $\pm\ 0.2$ (systematic error), and $1.6 \pm 0.13 \pm 0.3$ (monodisperse NIPA system); (b) $1.4 \pm 0.1 \pm 0.3$, and $1.0 \pm 0.1 \pm 0.3$ (bidisperse NIPA system). The systematic errors in Δ and Γ are calculated as before [165]. Δ obtained from yield-stress scaling in monodisperse and *bidisperse* systems are roughly in agreement with the Δ values obtained from the χ^2-minimization method (within the error bars) and reported previously for monodisperse systems [107].

Values of Γ obtained from scaling the τ derived from the HB fits, however, appear to be systematically lower than the exponents reported in both [107, 70] and from the χ^2 minimization method. This discrepancy in Γ values may have its origin in the shear history of the fluid microstructure [105, 99], which would affect the scaling behavior of τ vs. $|\phi - \phi_c|$. Also, if indeed there are subtle wall-slip effects, then this artifact would preferentially affect the data at higher shear-rates [79], i.e., the data which directly influence τ and Γ. In general, we suspect that the Herschel-Bulkley scaling analysis is optimally employed for packing fractions above jamming but very close to the jamming point, which is not optimized in our macro-rheological samples.

D.3 Scaling of Dimensionless Viscometry and Oscillatory Data

D.3.1 Viscometry Data

We also explore the critical scaling behavior of our steady-state and time-dependent data, all rendered dimensionless, following the procedure delineated in Nordstrom, et al. [107]. This can be accomplished by rescaling stress, shear moduli, strain-rate and oscillatory frequency as follows: $\frac{\sigma}{E}$, $\frac{G'}{E}$, $\frac{G''}{E}$, $\frac{\dot{\gamma}.\eta_{water}}{E}$ and $\frac{\omega.\eta_{water}}{E}$. We use the elastic modulus, E of NIPA microspheres as a function of temperature, reported by Nordstrom, *et al.* [108]. Since the NIPA microspheres used in this experiment and by Nordstrom, *et al.* [107] were synthesized using similar techniques [130, 1], we expect the swelling/deswelling behavior of both species to be similar. To do so, the elastic modulus vs. temperature reported in [108] is fit to a simple polynomial of the form $E(T) = A \cdot T^B + C$, where A, B, and C are fitting parameters. The elastic moduli for the temperatures used in our experiment are extracted from the best-fit polynomial function. This exercise is performed for both monodisperse and bidisperse NIPA systems. There is a caveat though: we assume that the functional form of the temperature dependence for elastic modulus is essentially similar for all NIPA microgel particles with similar synthesis protocols; this assumption may not hold true for a bidisperse NIPA system where each species has different swelling/deswelling rates with temperature. η_{water} is viscosity of the background medium for the micro-spheres, *viz.*, water.

With these new variables, we again explore critical scaling behavior using the χ^2-minimization method described above. The critical scaling factors for σ/E and $\dot{\gamma}.\eta_{water}/E$ are of the same form as before, i.e., $(|T-T_c|/T_c)^{\Delta}$ and $(|T-T_c|/T_c)^{\Gamma}$ respectively. Δ, Γ and T_c values obtained in this manner for both the monodisperse and bidisperse systems are reported in Table 8.3. The T_c calculated from the dimensionless quantities are same as before, *viz.*, 295 K for the monodisperse and 297 K for the bidisperse systems. Δ increases by 27% (monodisperse) and 36% (bidisperse) and Γ by 16% (monodisperse) and 11% (bidisperse) resulting in an overall increase in β by 10% (monodisperse) and 24% (bidisperse). Though the scaling exponents obtained in this method are similar to the ones obtained in [107], the magnitude of the dimensionless stress values are lower by an order of magnitude in comparison, and the scaled stresses are off by as much as four orders of magnitude, for comparable shear rates. We posit that this difference has its origin in the difference in pre-shear protocols followed in the macro and micro-rheology experiments [105].

The temperature-dependent rescaling factor, $\frac{|T-T_c|}{T_c}$ can be converted to its volume-fraction equivalent, $|\phi-\phi_c|$ as before. The best-fit scaling collapses for the monodisperse and bidisperse systems are shown in Fig. 8.8.

Dimensionless Viscometry Data: Scaling Exponents from χ^2-minimization Method

Sample	Δ	Γ	β	$T_c\ [K]$	ϕ_c
monodisperse	2.8±0.7	5.0±1.0	0.56±0.18	295±0.9	0.64±0.05
bidisperse	2.6±0.8	4.9±1.0	0.53±0.20	297±0.6	0.64±0.03

Dimensionless Viscometry Data: Exponents from Herschel-Bulkley Fitting Scheme

Sample	n	Δ	Γ	β	$T_c\ [K]$	ϕ_c
monodisperse	0.51±0.02	2.3±0.05	2.7±0.16	0.85±0.05	296.0±2.1	0.64±0.11
bidisperse	0.48±0.01	3.2±0.12	2.7±0.16	1.19±0.08	297.9±2.0	0.64±0.11

Table 8.3: Critical scaling exponents using $\frac{|T-T_c|}{T_c}$ as an optimization parameter.

If we use $|\phi - \phi_c|$ directly as the scaling parameter instead of $\frac{|T-T_c|}{T_c}$, Γ values are slightly larger for both the monodisperse and bidisperse systems, while Δ stays roughly the same. This gives a slightly larger value for $\beta = \Delta/\Gamma$ for both NIPA systems. These exponents are reported in Table 8.4.

Dimensionless Viscometry Data: Scaling Exponents from χ^2-minimization Method

Sample	Δ	Γ	β	ϕ_c
monodisperse	2.8±0.6	5.2±1.0	0.54±0.16	0.64±0.051
bidisperse	2.6±0.7	5.2±0.9	0.50±0.16	0.64±0.049

Table 8.4: Critical scaling exponents using $|\phi - \phi_c|$ as an optimization parameter.

D.3.2 Oscillatory Data

Critical scaling behavior of G' and G'' vs. ω rendered dimensionless is demonstrated in Fig. 8.9 for (a) monodisperse and (b) bidisperse NIPA systems. The best scaling collapse is obtained when $\frac{G'}{E}$ and $\frac{G''}{E}$ are rescaled by $|\phi - \phi_c|^\alpha$ for $\alpha = 1.1$. Note that the scaling exponent for the dimensionless data is more that 50% greater than that obtained previously. $\frac{\omega.\eta_{water}}{E}$ exhibits optimal critical scaling behavior when scaled with $|\phi - \phi_c|$, same as unscaled ω. As before, ϕ_c corresponds to $T_c = 295$ K for monodisperse and $T_c = 297$ K for bidisperse systems.

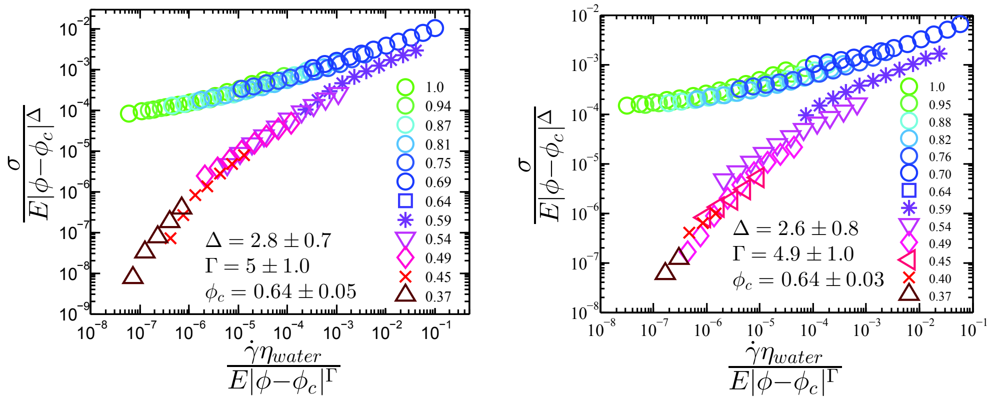

(a) Monodisperse

(b) Bidisperse

Figure 8.8: Volume-fraction-difference scaled $\frac{\sigma}{E}$ vs. $\frac{\dot{\gamma}\cdot\eta_{water}}{E}$ for aqueous suspensions of (a) monodisperse (diameter, $\sim$700 nm), and (b) bidisperse (diameters, $\sim$500 nm, 700 nm) NIPA microgel spheres. Volume-fraction difference, $|\phi-\phi_c|$ is calculated from the equivalent temperature difference, $\frac{|T-T_c|}{T_c}$, using DLS data on the thermal response of NIPA spheres. The values of Δ, Γ and ϕ_c are as follows: 2.8, 5, 0.64 for monodisperse NIPA suspensions, and 2.6, 4.9, 0.64 for bidisperse NIPA suspensions.

D.4 G', G'' vs. ω data *below* ϕ_c for bidisperse NIPA system

Fig. 8.10 shows elastic and viscous shear moduli for the bidisperse NIPA suspension (diameters, $\sim$500 nm, $\sim$700 nm) and function of frequency.

Cross-over frequency, $\omega_\times$ is defined as the frequency at which G' equals G''. To extract $\omega_\times$, G' and G'' vs. ω are fitted to arbitrary, high-order polynomial functions. The frequency at which the polynomial functions intersect is $\omega_\times$. The cross-over moduli corresponding to $\omega_\times$ are indicated by black asterisks at each packing fraction in Fig. 8.10.

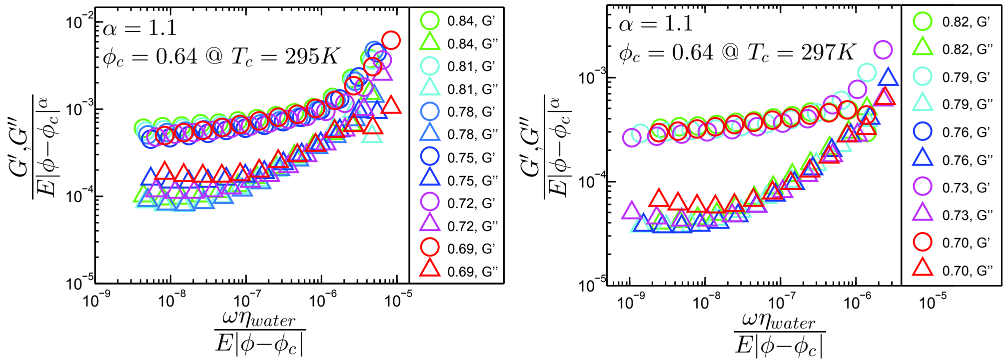

(a) Monodisperse (b) Bidisperse

Figure 8.9: $\frac{G'}{E}$ and $\frac{G''}{E}$ as function of $\frac{\omega.\eta_{water}}{E}$, all scaled by $|\phi - \phi_c|$, for (a) monodisperse NIPA microgel spheres (diameter, ∼700 nm; $\phi = 0.84, 0.81, 0.78, 0.75, 0.72, 0.69$), and (b) bidisperse NIPA microgel spheres (diameters, ∼500 nm, ∼700 nm; $\phi = 0.82, 0.79, 0.76, 0.73, 0.70$). The scaling exponent for G' and G'' is 1.1 and for ω 1.0, for monodisperse and bidisperse NIPA suspensions. $\phi_c = 0.64$ in both systems.

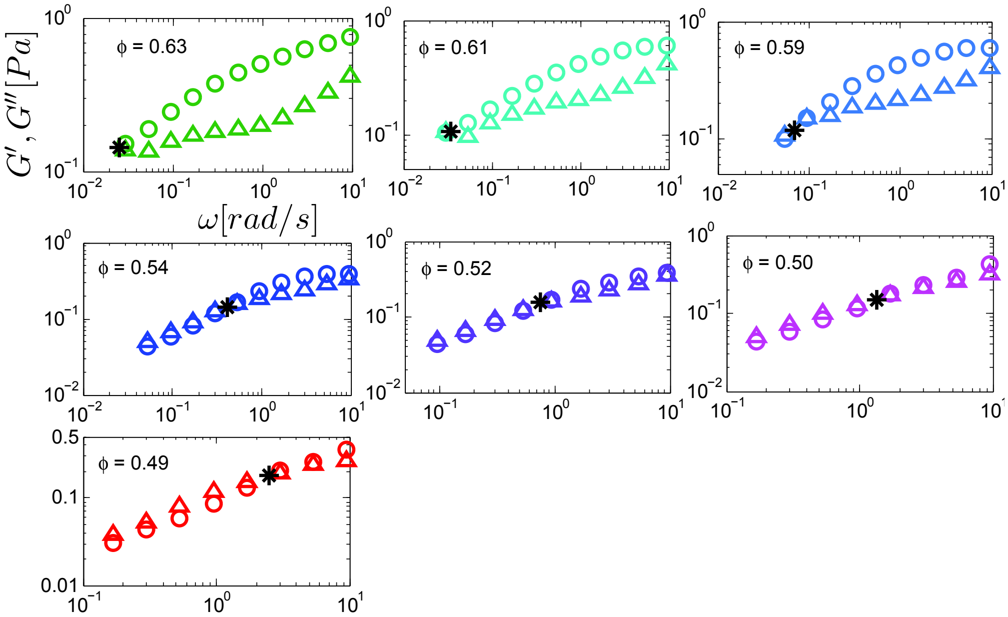

Figure 8.10: G', G'' vs. ω for the bidisperse NIPA suspension, measured at different packing fractions all below ϕ_c. In all subfigures, x-axes are ω rad/s, and y-axes are G' Pa (circles) and G'' Pa (triangles).

Bibliography

[1] A. M. Alsayed, M. F. Islam, J. Zhang, P. J. Collings and A. G. Yodh, *Science*, **309**, 1207 (2005).

[2] K. S. Anseth, C. N. Bowman and L. Brannon-Peppas, *Biomaterials*, **17** 1647–1657 (1996).

[3] R. C. Arevalo, J. S. Urbach, and D. L. Blair, *Biophys. J.*, **99** L65–L67 (2010).

[4] S. Badylak, K. Kokini, B. Tullius, A. Simmons-Byrd, and R. Morff, *J. Surg. Res.*, **103**, 190–202 (2002).

[5] M. Bai, A. R. Missel, W. S. Klug, and A. J. Levine, *Soft Matter*, **7**, 907–914 (2011).

[6] J. Baselga, I. HernPndez-Fuentes, I. F. PiBrola, and M. A. Llorente, *Macromolecules*, **20**, 3060–3065 (1987).

[7] J. Bastide, E. Mendes Jr., F. Boue, M. Buzier, and P. Linder, *Makromol. Chem., Macromol. Symp.*, **40**, 81–99 (1990).

[8] A. Basu, Q. Wen, X. Mao, T. C. Lubensky, P. A. Janmey, and A. G. Yodh, *Macromolecules*, **44**, 1671–1679 (2011).

[9] R. B. Bird, W. E. Stewart, and E. N.Lightfoot, *Transport Phenomena*, John Wiley & Sons, Inc. (1960).

[10] We gratefully acknowledge Dr. D Blair for matlab tracking routines *http://physics.georgetown.edu/matlab/*.

[11] C. P. Broedersz, X. Mao, T. C. Lubensky, and F. C. MacKintosh, *Nature Phys.*, **7**, 983 (2011).

[12] C. P. Broedersz and F. C. MacKintosh, *Soft Matter*, **7**, 3186–3191 (2011).

[13] P. L. Chandran and V. H. Barocas, *J. Biomech. Engg.*, **128**, 259–270 (2006).

[14] O. Chaudhuri, S. H. Parekh and D. A. Fletcher, *Nature*, **445**, 295–298 (2007).

[15] D. T. Chen, E. R. Weeks, J. C. Crocker, M. F. Islam, R. Verma, J. Gruber, A. J. Levine, T. C. Lubensky, A. G. Yodh, *Phys. Rev. Lett.*, **90**, 108301 (2003).

[16] D. T. N. Chen, K. Chen, L. A. Hough, M. F. Islam, and A. G. Yodh, *Macromolecules*, **43**, 2048–2053 (2010).

[17] K. Chen, W. G. Ellenbroek, Z. X. Zhang, D. T. N. Chen, P. J. Yunker, S. Henkes, C. Brito, O. Dauchot, W. van Saarloos, A. J. Liu and A. G. Yodh, *Phys. Rev. Lett.*, **105**, 025501 (2010).

[18] K. S. Cho, K. Hyun, K.H. Ahn, S. J. Lee, *J. Rheol.*, **49**, 747–758 (2005).

[19] Y. Cohen, O. Ramon, I. J. Kopelman, and S. Mizrahi, *J. Polym. Sci., Polym. Phys. Ed.*, **30**, 1055–1067 (1992).

[20] E. Conti and F. C. MacKintosh, *Phys. Rev. Lett.*, **102**, 088102 (2009).

[21] J. Crocker and D. Grier, *J. Colloid Interface Sci.*, **179** 298 (1996).

[22] P. de Gennes, *Scaling Concepts in Polymer Physics*, Cornell University Press (1979).

[23] B. A. DiDonna, and T. C. Lubensky, *Phys. Rev. E*, **72**, 066619 (2005).

[24] L. Dong and A. Hoffman, *J. of Controlled Release*, **15**, 141–152 (1991).

[25] J. F. Douglas, J. M. Gasiorek, and J. A. Swaffield, *Fluid Mechanics*, 2nd Ed. Longman Group Ltd. (1985).

[26] D. J. Durian, Phys. Rev. Lett. **75**, 4780 (1995); D. J. Durian, *Phys. Rev. E*, **55**, 1739 (1997).

[27] S. F. Edwards and T. A. Vilgis, *Polymer*, **27**, 483–492 (1986).

[28] S. F. Edwards and T. A. Vilgis, *Reports on Progress in Physics*, **51**, 243–297 (1988).

[29] R. Everaers, *Eur. Phys. J. B*, **4**, 341-350 (1998).

[30] R. H. Ewoldt, A. E. Hosoi, and G. H. McKinley, *J. Rheol.*, **52**, 1427–1458 (2008).

[31] R. H. Ewoldt, P. Winter, J. Maxey, G. H. McKinley, *Rheol. Acta*, **49**, 191–212 (2010).

[32] Y. Gao and M. L. Kilfoil, *Optics Express*, **17**, 4685 (2009).

[33] M. L. Gardel, J. H. Shin, F. C. MacKintosh, L. Mahadevan, P. Matsudaira, and D. A. Weitz, *Science*, **304** 1301 (2004).

[34] M. L. Gardel, F. Nakamura, J. Hartwig, J. C. Crocker, T. P. Stossel, and D. A. Weitz, *Phys. Rev. Lett.*, **96**, 088102 (2006).

[35] C. Gerth, W. W. Roberts, and J. D. Ferry, *Biophys. Chem.*, **2**, 208–217 (1974).

[36] T. W. Gilbert, M. S. Sacks, J. S. Grashow, S. L.-Y. Woo, S. F. Badylak, and M. B. Chancellor, *J. Biomech. Engg.*, **128**, 891–898 (2006).

[37] F. Gittes, B. Mickey, J. Nettleton, and J. Howard, *J. Cell. Biol.*, **120**, 923–934 (1993).

[38] G. Glatting, and R. G. Winkler, P. Reineker, *Polymer*, **38**, 4049–4052 (1997).

[39] A. D. Gopal and D. J. Durian, Phys. Rev. Lett. **91**, 188303 (2003).

[40] Y. Han, N. Y. Ha, A. M. Alsayed and A. G. Yodh, *Phys. Rev. E*, **77**, 041406 (2008).

[41] H. Hatami-Marbini and R. C. Picu, *Acta Mech.*, **205**, 77–84 (2009).

[42] T. Hatano, M. Otsuki, and S. Sasa, *J. Phys. Soc. Jpn.*, **76**, 023001 (2007).

[43] T. Hatano, *J. Phys. Soc. Jpn.*, **77**, 123002 (2008).

[44] T. Hatano, *Prog. Theo. Phys. Supp.*, **184**, (2010).

[45] D. A. Head, A. J. Levine, and E. C. MacKintosh, *Phys. Rev. Lett.*, **91**, 108102 (2003).

[46] D. A. Head, A. J. Levine, and F. C. MacKintosh, *Phys. Rev. E*, **68**, 061907 (2003).

[47] D. A. Head, F. C. MacKintosh, and A. J. Levine, *Phys. Rev. E*, **68**, 025101(R) (2003).

[48] A. Hecht, R. Duplessix, and E. Geissler, *Macromolecules*, **18**, 2167–2173 (1985).

[49] D. G. Hepworth, A. Steven-fountain, D. M. Bruce, and J. F. V. Vincent, *Journal of Biomechanics*, **34** 341–346 (2001).

[50] C. Heussinger, and E. Frey, *Phys. Rev. Lett.*, **97**, 105501 (2006).

[51] B. Hinner, M. Tempel, E. Sackmann, K. Kroy, and E. Frey, *Phys. Rev. Lett.*, **81**, 2614 (1998).

[52] L. A. Hough, M. F. Islam, P. A. Janmey, and A. G. Yodh, *Phys. Rev. Lett.*, **93**, 168102 (2004).

[53] T. Hsu, and C. Cohen, *Polymer*, **25**, 1419–1423 (1984).

[54] T. Hsu, D. S. Ma, and C. Cohen, *Polymer*, **24**, 1273–1278 (1983).

[55] E. M. Huisman, T. van Dillen, P. R. Onck, and E. Van der Giessen, *Phys. Rev. Lett.*, **99**, 208103 (2007).

[56] E. M. Huisman, C. Storm, and G. T. Barkema, *Phys. Rev. E* **82**, 061902 (2010).

[57] E. M. Huisman, and T. C. Lubensky, *Phys. Rev. Lett.*, **106**, 088301 (2011).

[58] J. M. Huyghe, and C. J. M. Jongeneelen, *Biomech. Model. Mechanobiol.*, **11**, 161–170 (2012).

[59] M. F. Islam, D. E. Milkie, C. L. Kane, A. G. Yodh, and J. M. Kikkawa, *Phys. Rev. Lett.*, **93**, 037404 (2004).

[60] P. A. Janmey, E. J. Amis, and J. D. Ferry, *J. Rheol.*, **26**, 599–600 (1982).

[61] P. A. Janmey, S. Hvidt, J. Kas, D. Lerche, A. Maggs, E. Sackmann, M. Schliwa, and T. P. Stossel, *J. Biol. Chem.*, **269**, 32503–32513 (1994).

[62] P. A. Janmey, M. E. McCormick, S. Rammensee, J. L. Leight, P. C. Georges and F. C. MacKintosh, *Nature Mat.*, **6**, 48–51 (2007).

[63] P. A. Janmey, J. P. Winer, and J. W. Weisel, *J. R. Soc. Interface.*, **6**(30), 1–10 (2009).

[64] I. Jorjadze, L. Pontani, K. A. Newhall and J. Brujic, *PNAS, Advanced Article* (2011).

[65] Y. E. Ju, P. A. Janmey, M. E. McCormick, E. S. Sawyer, and L. A. Flanagan, *Biomaterials*, **28**, 2097–2108 (2007).

[66] H. Kang, Q. Wen, P. A. Janmey, J.X. Tang, E. Conti, and F. C. MacKintosh, *J. Phys. Chem. B*, **113**, 3799–3805 (2009).

[67] A. R. Kansal, S. Torquato and F. H. Stillinger, *J. Chem. Phys.*, **117**, 8212 (2002).

[68] M. Kasai, H. Kawashima, and F. Oosawa, *J. Polym. Sci.*, **44**, 51–69 (1960).

[69] G. Katgert, M. E. Mobius and M. van Hecke, *Phys. Rev. Lett.*, **101**, 058301 (2008).

[70] G. Katgert, B. P. Tighe, M. E. Mobius and M. van Hecke, *Europhys. Lett.*, **90**, 54002 (2010).

[71] G. Katgert and M. van Hecke, *Europhys. Lett.*, **92**, 34002 (2010).

[72] A. S. Keys, A. R. Abate, S. C. Glotzer and D. J. Durian, *Nature Phys.*, **3**, 260 (2007).

[73] M. Y. Kizilay, and O. Okay, *Macromolecules*, **36**, 6856–6862 (2003).

[74] M. A. Kotlarchyk, E. L. Botvinick, and A. J. Putnam, *J. Phys.: Condens. Matter*, **22** 194121 (2010).

[75] L. Kreplak, H. Bar, J. F. Leterrier, H. Herrmann, and U. Aebi, *J. Mol. Biol.*, **354**, 569–577 (2005).

[76] K. Kroy, and E. Frey, *Phys. Rev. E*, **55**, 3092 Q1 (1997).

[77] B. G. Langer, J. W. Weisel, P. A. Dinauer, C. Nagaswami and W. R. Bell, *J. Biol. Chem.*, **263**, 15056–15063 (1988).

[78] S. A. Langer and A. J. Liu, *J. Phys. Chem. B*, **101**, 8667 (1997).

[79] R. G. Larson, *The Structure and Rheology of Complex Fluids*, Oxford University Press (1999).

[80] H. Lee, K. Paeng, S. F. Swallen and M. D. Ediger, *Science*, **323**, 231 (2009).

[81] J. F. Leterrier, J. Kas, J. Hartwig, R. Vegners, and P. A. Janmey, *J. Biol. Chem.*, **271**, 15687–15694 (1996).

[82] I. Levental, P. C. Georges, and P. A. Janmey, *Soft Matter*, **1**, 299–306 (2007).

[83] A. J. Levine and T. C. Lubensky, *Phys. Rev. E* **63**, 041510 (2001).

[84] A. J. Levine, D. A. Head and F. C. MacKintosh, *J. Phys.: Condens. Matter*, **16**, S2079–S2088 (2004).

[85] O. Lieleg, M. M. A. E. Claessens, C. Heussinger, E. Frey, and A. R. Bausch, *Phys. Rev. Lett.*, **99**, 088102 (2007).

[86] O. Lieleg, K. M. Schmoller, C. J. Cyron, Y. Luan, W. A. Wall, and A. R. Bausch, *Soft Matter*, **5**, 1796–1803 (2009).

[87] B. Lindemann, U. P. Schroder, and W. Oppermann, *Macromolecules*, **30**, 4073–4077 (1997).

[88] A. J. Liu, S. Ramaswamy, T. G. Mason, H. Gang, and D. A. Weitz, Phys. Rev. Lett., **76**, 3017–3020 (1996).

[89] A. J. Liu and S. R. Nagel, *Nature*, **396**, 21 (1998).

[90] J. Liu, G. Koenderink, K. Kasza, F. MacKintosh, and D. Weitz, *Phys. Rev. Lett.*, **98**, 198304 (2007).

[91] H. Lodish, A. Berk, S L. Zipursky, P. Matsudaira, D. Baltimore, and J. Darnell, *Molecular Cell Biology*, 4th edition, W. H. Freeman, 2000; R. P. Mecham, *The Extracellular Matrix: An Overview*, Springer, 2011.

[92] V. V. Lopatin, A. A. Askadskii, A. S. Peregudov, and V. G. Vasil'ev, *J. App. Polym. Sci.*, **96**, 1043–1058 (2005).

[93] F. C. MacKintosh, J. Kas and P. A. Janmey, *Phys. Rev. Lett.*, **75**, 4425–4428 (1995).

[94] C. W. Macosko, *Rheology Principles, Measurements, and Applications*, Wiley-VCH, Inc. (1994).

[95] S. Mallam, F. Horkay, A. Hecht, and E. Geissler, *Macromolecules*, **22**, 3356–3361 (1989).

[96] T. G. Mason and D. A. Weitz, Phys. Rev. Lett., **74**, 1250–1253 (1995).

[97] X. Mao, P. M. Goldbart, X. Xing, and A. Zippelius, *Euro. Phys. Lett.* **80**, 26004 (2007).

[98] J. Marko and E. Siggia, *Macromolecules*, **28**, 8759–8770 (1995).

[99] K. Martens, L. Bocquet, and J. Barrat, Phys. Rev. Lett. **106**, 156001 (2011).

[100] J. Mewis, and N Wagner, *Colloidal Suspension Rheology*, Cambridge University Press (2012).

[101] S. E. Michaud, *Thromb. Res.*, **107**, 245–254 (2002).

[102] I. Migneault, C. Dartiguenave, M. J. Bertrand, and K. C. Waldron, *BioTechniques*, **37** 790–802 (2004).

[103] M. Minsky, *Microscopy apparatus*, Patent US3013467 (1961).

[104] D. Mizuno, C. Tardin, C. F. Schmidt, and F. C. MacKintosh, *Science*, **315**, 370–373 (2007).

[105] P. C. F. Moller, J. Mewis and D. Bonn, *Soft Matter*, **2**, 274 (2006).

[106] P. B. Morgana, N. Efron, M. Helland, M. Itoi, D. Jones, J. J. Nichols, E. van der Worp, and C. A. Woods, *Contact Lens and Anterior Eye*, **33**, 196–198 (2010).

[107] K. N. Nordstrom, E. Verneuil, P. E. Arratia, A. Basu, Z. Zhang, A. G. Yodh, J. P. Gollub and D. J. Durian, *Phys. Rev. Lett.*, **105**, 175701 (2010).

[108] K. N. Nordstrom, E. Verneuil, W. G. Ellenbroek, T. C. Lubensky, J. P. Gollub and D. J. Durian, *Phys. Rev. E*, **82**, 041403 (2010).

[109] R. Nossal, *Macromolecules*, **18** 49–54 (1985).

[110] C. S. O'Hern, S. A. Langer, A. J. Liu and S. R. Nagel, *Phys. Rev. Lett.*, **88**, 075507 (2002).

[111] C. S. O'Hern, L. E. Silbert, A. J. Liu and S. R. Nagel, *Phys. Rev. E*, **68**, 011306 (2003).

[112] L. H. H. Olde Damink, P. J. Dijkstra, M. J. A. Van Luyn, P. B. Van Wachem, P. Nieuwenhuis, and J. Feijen, *J. Materials Science: Materials in Medicine*, **6** 460–472 (1995).

[113] P. Olsson and S. Teitel, *Phys. Rev. Lett.*, **99**, 178001 (2007).

[114] P. Olsson and S. Teitel, *arXiv:*1109.2545v1 [cond-mat.dis-nn] (2011).

[115] P. R. Onck, T. Koeman, T. van Dillen, and E. van der Giessen, *Phys. Rev. Lett.*, **95**, 178102 (2005).

[116] J. Orberg, E. Baer, and A. Hiltner, *Connect. Tissue Res.*, **11**, 285–297 (1983).

[117] A. Ott, M. Magnasco, A. Simon, and A. Libchaber, *Phys. Rev. E*, **48**, R1642-R1645 (1993).

[118] J. D. Pardee, and J. A. Spudich, *Methods Cell Biol.*, **24**, 271–289 (1982).

[119] O. Pekcan, and S. Kara, *Polym. Int.*, **52**, 676–684 (2003).

[120] R. Pelton, *Adv. Colloid Interface Sci.*, **85**, 1 (2000).

[121] S. Radji, H. Alem, S. Demoustier-Champagne, A. M. Jonas, and S. Cuenot, *Macromol. Chem. Phys.*, **213**, 580–586 (2012).

[122] J. C. Rahola, *Elasticity and dynamics of weakly aggregated colloidal systems*, PhD thesis, Universite de Fribourg, Switzerland (2007).

[123] E. G. Richards, and C. J. Temple, *Nature (Physical Science)*, **230**, 92–96 (1971).

[124] S. W. Rothwell, T. J. Reid, J. Dorsey, W. S. Flournoy, M. Bodo, P. A. Janmey, and E. Sawyer, *J. Trauma*, **59**, 143–149 (2005).

[125] M. Rubinstein and S. Panyukov, *Macromolecules*, **30**, 8036–8044 (1997).

[126] M. Rubinstein, and S. Panyukov, *Macromolecules*, **35**, 6670–6686 (2002).

[127] M. Rubinstein and R. Colby, *Polymer Physics* (Oxford University Press, New York, 2003).

[128] E. A. Ryan, L. F. Mockros, J. W. Weisel, and L. Lorand, *Biophys. J.*, **77**, 2813–2826 (1999).

[129] R. L. Satcher Jr., and C. F. Dewey Jr., *Biophys. J.*, **71**, 109–118 (1996).

[130] H. Senff and W. Richtering, *J. Chem. Phys.*, **111**, 4 (1999).

[131] H. Senff and W. Richtering, *Colloid Polym Sci.*, **278**, 830 (2000).

[132] D. A. Sessoms, I. Bischofberger, L. Cipelletti and V. Trappe, *Phil. Trans. R. Soc. A*, **367**, 5013 (2009).

[133] R. E. Shadwick, *J. Exp. Biol.*, **202**, 3305–3313 (1999).

[134] J. V. Shah, and P. A. Janmey, *Rheol. Acta*, **36**, 262–268 (1997).

[135] L. Sivakumar, G. Agarwal, *Biomaterials*, **31**, 4802–4808 (2010).

[136] J. U. Sommer, and S. Lay, *Macromolecules*, **35**, 9832-9843 (2002).

[137] L. Starrs, and P. Bartlett, *Faraday Discuss.*, **123**, 323–334 (2003).

[138] C. Storm, J. J. Pastore, F. C. MacKintosh, T. C. Lubensky, and P. A. Janmey, *Nature*, **435**, 191 (2005).

[139] C. Svaneborg, G. S. Grest, and R. Everaers, *Phys. Rev. Lett.*, **93**, 257801 (2004).

[140] A. Tanguy, J. P. Wittmer, F. Leonforte, and J. L. Barrat, *Phys. Rev. B*, **66**, 174205 (2002).

[141] B. P. Tighe, E. Woldhuis, J. J. C. Remmers, W. van Saarloos and M. van Hecke, *Phys. Rev. Lett.*, **105**, 088303 (2010).

[142] B. P. Tighe, *Phys. Rev. Lett.*, **107**, 158303 (2011); private communication.

[143] S. Thomopoulos, G. M. Fomovsky, P. L. Chandran and J. W. Holmes, *J. Biomech. Engg.*, **129**, 642–650 (2007).

[144] P. Tomasik, *Chemical and functional properties of food saccharides*, CRC Press LLC, 2003.

[145] L. R. G. Treloar, *The Physics of Rubber Elasticity* (Clarendon, Oxford, 1975).

[146] T. A. Ulrich, A. Jain, K. Tanner, J. L. MacKay and S. Kumar, *Biomaterials*, **31**, 1875–1884 (2010).

[147] D. Vader, A. Kabla, D. Weitz and L. Mahadevan, *PLoS ONE*, **4**, e5902 (2009).

[148] M. T. Valentine, Z. E. Perlman, M. L. Gardel, J. H. Shin, P. Matsudaira, T. J. Mitchison, and D. A. Weitz, *Biophys. J.*, **86** 4004 (2004).

[149] M. van Hecke, *J. Phys.: Condens. Mat.*, **22**, 033101 (2010).

[150] L. Z. Wang, J. Gorlin, S. E. Michaud, P. A. Janmey, R. P. Goddeau, R. Kuuse, R. Uibo, D. Adams, and E. S. Sawyer, *Thromb. Res.*, **100**, 537–548 (2000).

[151] J. W. Weisel, *Biophys. Chem.*, **112**, 267–276 (2004).

[152] N. Weiss, and A. Silberberg, *British Polym. J.*, **9**, 2, 144–150 (1977).

[153] N. Weiss, T. V. Vliet, and A. Silberberg, *J. Polym. Sci.: Polymer Physics Edition*, **17**, 2229–2240 (1979).

[154] E. W. Weisstein, *"Lissajous Curve."* From MathWorld–A Wolfram Web Resource. http://mathworld.wolfram.com/LissajousCurve.html

[155] Q. Wen, A. Basu, J. Winer, A. Yodh, and P. Janmey, *New J. Phys.*, **9** 428 (2007).

[156] M. Wilhelm, *Macromol. Mater. Eng.* **287**, 83–105 (2002).

[157] J. Wilhelm, and E. Frey, *Phys. Rev. Lett.*, **91**, 108103 (2003).

[158] X. S. Wu, A. S. Hoffman and P. Yager, *J. Polymer Science Part A: Polymer Chemistry*, **30**, 2121–2129 (1992).

[159] N. Xu, *Front. Phys.*, **6**(1): 109-123 (2011).

[160] Y. Yang, L. M. Leone and L. J. Kaufman, *Biophys. J.*, **97**, 2051–2060 (2009).

[161] N. Y. Yao, R. J. Larsen, and D. A. Weitz, *J. Rheol.*, **52**, 1013–1025 (2008).

[162] T. Yeung, P. C. Georges, L. A. Flanagan, B. Marg, M. Ortiz, M. Funaki, N. Zahir, W. Ming, V. Weaver, and P. A. Janmey, *Cell Motil. Cytoskeleton*, **60**, 24–34 (2005).

[163] Z. Zhang, N. Xu, D. T. N. Chen, P. Yunker, A. M. Alsayed, K. B. Aptowicz, P. Habdas, A. J. Liu, S. R. Nagel and A. G. Yodh, *Nature*, **459**, 230 (2009).

[164] Y. Zhao, Y. Cao, Y. Yang, C. Wu, *Macromolecules*, **36**, 855–859 (2003).

[165] The systematic error in α (where $G_0 \propto |\phi - \phi_c|^{\alpha}$) is calculated as follows: The G_0 vs. $|\phi - \phi_c|$ fit is performed with the first 30% of data excluded, which yields an α, say α_1. The fit is performed again with the last 30% of the data-set excluded this time, yielding a different α, say α_2. The largest standard deviation between the α calculated for the entire data-set, and α_1 or α_2 gives the systematic error.

[166] NIH U or NIH unit indicates the current US standard used for the measurement of human α-thrombin, originally developed by the National Institutes of Health (NIH) in Bethesda, MD.